Few-body collisions in a quantum gas mixture of ^{40}K and ^{87}Rb atoms

by

Ruth Shewmon Bloom

B.S., Massachusetts Institute of Technology, 2008

A thesis submitted to the

Faculty of the Graduate School of the

University of Colorado in partial fulfillment

of the requirements for the degree of

Doctor of Philosophy

Department of Physics

2014

This thesis entitled:
Few-body collisions in a quantum gas mixture of ^{40}K and ^{87}Rb atoms
written by Ruth Shewmon Bloom
has been approved for the Department of Physics

Deborah Jin

Eric Cornell

Date

The final copy of this thesis has been examined by the signatories, and we find that both the content and the form meet acceptable presentation standards of scholarly work in the above mentioned discipline.

Bloom, Ruth Shewmon (Ph.D., Physics)

Few-body collisions in a quantum gas mixture of ^{40}K and ^{87}Rb atoms

Thesis directed by Deborah Jin

This thesis describes experiments on few-body interactions in a mixture of ultracold bosonic ^{87}Rb and fermionic ^{40}K atoms. Ultracold atoms are celebrated as a platform to explore fundamental quantum physics because their internal states, external potentials, and interactions with each other can be controlled by straightforward electrical and optical tools. In the case of Bose-Fermi mixtures, control comes at the cost of stability when strong interactions give rise to inelastic collisions that destroy the atomic samples. I present detailed measurements of the cross sections for these inelastic processes and discuss how they fit into an emerging pattern of resonances that is leading to better models of few-atom interactions. These phenomena have their roots in universal Efimov physics, which is a paradigm of quantum three-body interactions that was originally inspired by exotic nuclear states. I also discuss several methods to control the formation of KRb Feshbach molecules within the finite lifetime of the interacting K and Rb atomic mixture.

Dedication

To Paul Shewmon, who inspires me to be a better scientist.

Acknowledgements

This thesis only lists one author on the title page, but it really includes the work of many people. I've had the pleasure of working closely with some fantastic teammates in the lab while we ran the experiments that are presented here. John Perreault was our post-doc when I first arrived at JILA. His deep knowledge of optics and atomic physics was an invaluable resource. Ty Cumby, who was the senior graduate student during most of my PhD, had a remarkable patience and attention to detail. He taught me how to run quantum gas experiments, and we had a lot of fun working together. We were later joined by Ming-Guang Hu, whose powerful enthusiasm is driving our group forward to a new generation of experiments. I'm sure the lab will accomplish great things under his leadership.

Of course, none of this work would have been possible without our fearless leader, Debbie Jin. She is equally at home in the lab's tangled jungle of wires or in contemplating deep questions on the quantum nature of matter. It's amazing how much time Debbie makes for her students, and I really appreciated the insightful advice she has given on every aspect of my work – from diagnosing technical problems to designing experiments, editing the written results, presenting them at conferences, and more. She has a way of making complex problems seem simple. I couldn't have asked for a better research adviser.

Our lab is part of a larger group that is jointly run by Debbie Jin and Eric Cornell. Eric is a great leader and role model, and his love of physics is contagious. It's also been wonderful to have so many people in the group to bounce idea off of and borrow equipment from, and I'm glad that I had the chance to learn about the inner workings of so many great experiments at our big

meetings.

JILA is a fun place to work because the community is so inter-connected. A huge number of people from JILA contributed to the work in this thesis, more than I can list here, so I'd like to take a moment to thank everybody. In particular, Tracy Keep in the instrument shop did a masterful job of building the magnetic coils that are central to our experiment. Jose D'Incao patiently answered so many of my questions about scattering theory, for which I am also grateful. The JILA electronics shop, especially Terry Brown and Carl Sauer, designed some incredible circuits for our lab.

Finally, I want to thank my family. This PhD has been hard work, but your support makes every burden lighter. I love you.

Contents

Chapter

Tables

Table

Figures

Figure

Chapter 1

Introduction

A prism disperses white light into a rainbow, but the light emitted by atoms splits into discrete lines of color. These spectra inspired Niels Bohr to deduce the quantized structure of the atom [1]. One hundred years later, atoms are still helping us discover the quantum world. Techniques like laser cooling and forced evaporation can bring a gas of atoms to ultra cold temperatures near absolute zero [2, 3]. Here, atomic wave functions spread out to overlap each other and quantum mechanics plays out on a macroscopic scale. This thesis is about measurements of the collisions between a few atoms in such an ultra cold gas.

1.1 Bosons and Fermions near absolute zero

Most of the particles and excitations in the known universe are categorized as either Bosons or Fermions. Fermions have half-integer spins and the Pauli exclusion principle forbids them from occupying the same quantum state. Protons, neutrons, and electrons are all Fermions and Pauli exclusion dictates the way these particles arrange themselves to create atoms and materials. On the other hand, Bosons have integer spins and multiple Bosons can occupy the same quantum state. The photon is a familiar example of a bosonic particle, and ^{4}He is a composite Boson famous for its superfluidity at low temperatures.

Bose and Fermi gases have distinctly different behaviors in the limit of zero temperature. The relatively friendly Bosons pile together into the quantum state with lowest energy, forming a Bose-Einstein Condensate (BEC) [4]. Atomic BECs have shown interesting quantum properties

like matter wave interference [5] and superfluidity [6]. Identical Fermions spread across the lowest available energy levels with one particle per quantum state, forming a Degenerate Fermi Gas (DFG) [7]. The DFG is essential to the behavior of matter all around us – electrons in a metal form a DFG, as do neutron stars.

Mixtures of Bosons and Fermions, which are the subject of this work, can add up to more than the sum of their parts. The superfluid transition temperature in (bosonic) liquid ^{4}He is raised by the presence of (fermonic) ^{3}He [8]. Conversely, bosonic lattice excitations mediate Cooper pairing of electrons in solids, which leads to superconductivity [9]. As for cold atoms, Bose gases are often used to sympathetically cool Fermi gases to lower temperatures. At these temperatures, strongly interacting ultra cold Bose-Fermi mixtures are expected to host quantum phase transitions and novel pairing phenomena [10].

1.2 Universality and ultra cold atoms

Gases of ultracold atoms have promising applications in communications, information processing, and sensors, but I would argue that their most fascinating application is in the emulation of other quantum systems. The collective dynamics of strongly interacting quantum particles is a frontier for modern science that could unlock the secrets of superconductors, dense nuclear matter, astrophysics, and more. Unfortunately, the behaviors of quantum systems are notoriously difficult to model[1] . Feynman famously proposed that we circumvent this problem by using one well controlled quantum system to simulate another quantum system's behavior [11].

A remarkable level of control has already been demonstrated in ultra cold atom experiments, thanks to a growing set of experimental tools [12]. For example, a magnetic Fano-Feshbach resonance was used to control interactions between fermionic atoms to realize Cooper pairing and the BCS-BEC crossover transition in a Fermi gas [13]. The optical lattice, formed by an interference

[1] To simply write down the full quantum state of N interacting particles requires 2^N numbers. The cost of computing quickly gets out of control as particle number increases. If every one of the protons in the known universe were used as memory in a giant classical computer, then it could only store the complete description of a few hundred quantum particles.

pattern in light, made it possible to explore the quantum phase transition from a Mott insulator to a superfluid state in a Bose gas [14]. High-resolution optics were later used to manipulate and detect these states one atom at a time [15]. In other experiments, inventive configurations of optical and magnetic fields are being used to try to realize topologically non-trivial states of matter [16].

These tools are put to good use in ultra cold atoms because of a property called universality, where very different quantum systems often exhibit very similar behavior. In spite of the length and energy scales that appear to separate them, an ultra cold atomic Fermi gas near a Fano-Feshbach resonance has much in common with a solid-state superconductor. Dilute gases of ultra cold atoms can serve as a test bed for quantum models and concepts that apply to other universal systems that are less easy to access experimentally [17].

1.3 Universal few-body interactions

The work in this thesis focuses on universal few-body interactions between ultra cold atoms. The most straightforward system in this category consists of two atoms with contact interactions. A Fano-Feshbach resonance occurs at specific magnetic fields where the energy of these two atoms is the same as a molecular bound state that has a different magnetic moment [18]. The scattering length, which parameterizes two-body interactions, diverges near Fano-Feshbach resonances. Experimenters can dial in magnetic field values near the resonance to achieve repulsive or attractive interactions that vary by orders of magnitude. This magnetic tuning means that a single ultra cold atom experiment has the flexibility to operate over a huge parameter range rather than relying on scattering properties that were fine-tuned by Nature (which must be done in nuclear physics, for example).

For each Fano-Feshbach resonance there is an associated bound state called a Feshbach molecule, whose binding energy is also controlled by the magnetic field [19]. These molecules are an important first step in the formation process of ultra cold dipolar molecules, which promise to dramatically extend the range of quantum models that can be simulated in ultra cold atomic gases [20]. Feshbach molecules also have interesting properties in their own right, for example their

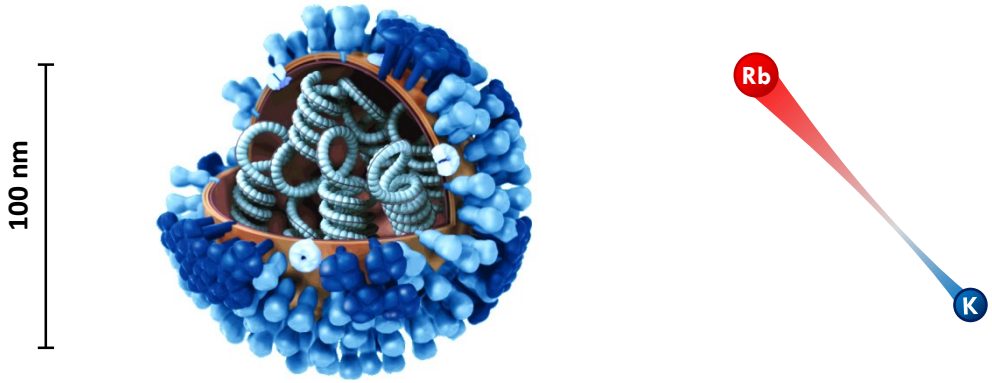

Figure 1.1: Feshbach molecules are quantum-mechanical bound states that can attain gigantic spatial extent. The influenza virus (left) contains hundreds of millions of atoms yet it has a comparable size to some of the diatomic $^{40}K^{87}Rb$ Feshbach molecules that are studied in this thesis (right). The virus cartoon is reproduced from www.cdc.gov.

huge size as illustrated in Fig. 1.1.

After two-body interactions, the logical next step is to consider three-body interactions. The quantum three-body problem has a universal solution in the limit of strong interactions, which is called the Efimov effect [21]. This effect consists of an infinite series of three-body bound states called Efimov trimers. Amazingly, the trimers follow a discrete scale invariance such that for each bound state there exists one larger by a scaling factor that depends on the relative masses of the constituent particles. Much like Feshbach molecules, their spatial extent can be gigantic. Although Efimov's theory was intended for the internal structure of exotic nuclei, the first clear observation of these effects occurred in the collisions between ultra cold Cesium atoms [22]. Efimov states in cold atoms occur near Fano-Feshbach resonances, where interactions are strong [23]. They give rise to inelastic three-body collisions that eject atoms from the ultra cold gas. Measurements of these atom loss rates have revealed an intricate series of resonances in several different atomic species, confirming key predictions of Efimov's work and related theories [24].

These phenomena are fascinating, but they also have an important practical side-effect: atom loss rates limit the available time to perform other quantum physics experiments. A quantitative understanding of few-body collisions is therefore essential to the design of experiments that rely on

strong interactions in ultra cold atomic gases. For this reason, it was exciting to discover that the locations of Efimov loss resonances in different single-species quantum gases followed a simple and completely unexpected pattern [25, 26, 27]. This was an opportunity to refine and simplify existing models of few-body interactions, and a promise that measurements in one atomic species could be used to predict very specific details about the behavior of another. It remains to be seen how far this success can be extended to systems containing multiple species of atoms or systems with strong background interactions that effectively weaken the influence of Fano-Feshbach resonances.

1.4 Overview

This thesis explores few-body physics in a Bose-Fermi mixture of ^{87}Rb and ^{40}K atoms with resonant interspecies interactions. To that end, Fig. 1.2 outlines the scattering processes that are measured. The rates of these few-body scattering processes can reveal a lot about the way atoms see each other. Whereas related phenomena are well-studied in single-species quantum gases, the same level of detail has not yet been realized in quantum gas mixtures like ^{87}Rb–^{40}K.

The extra complexity of atomic mixture experiments has so far made them less popular than their single-species counterparts. In the study of few-body collisions, however, the Bose-Fermi mixture offers some advantages: the fermionic two-body Feshbach molecule has a longer lifetime than similar molecules in Bose gases; the two types of atoms can also be measured independently to gain more information about who participates in collisions; and Pauli exclusion prevents collisions between identical ^{40}K atoms so that there are fewer types of collisions to analyze. More broadly, the mass-imbalanced Bose-Fermi mixture provides an opportunity to test the generality of theories that were honed on experiments with only one type of atom.

The remainder of the work is organized as follows.

Chapter 2 is about tuning the interspecies scattering properties with DC magnetic fields. This includes a brief overview of the physics of Fano-Feshbach resonances and the inelastic loss processes that accompany them. Chapter 3 introduces a high-current electromagnet system that is used to create these magnetic fields. Chapter 4 goes on to describe how samples of ^{40}K and ^{87}Rb atoms are

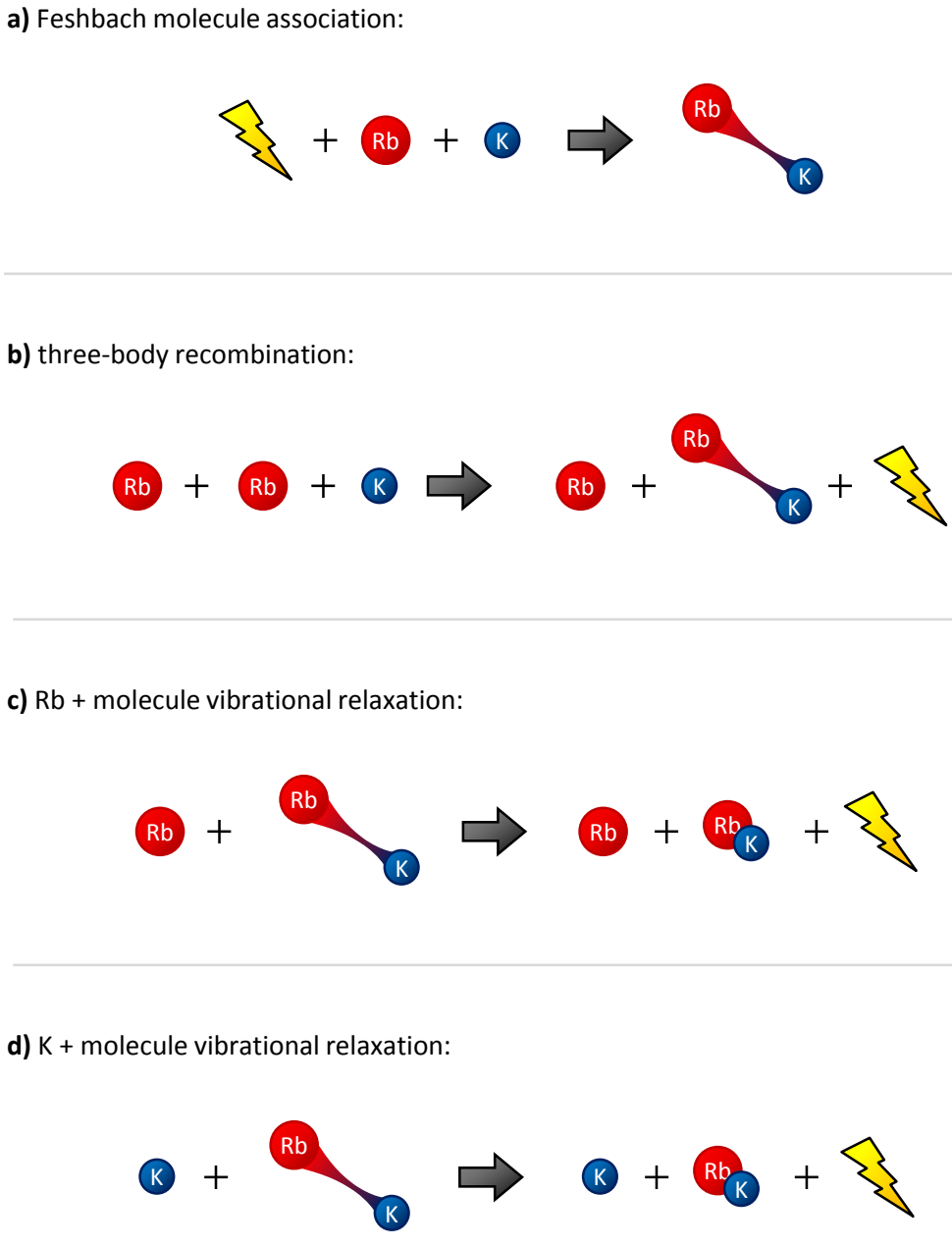

Figure 1.2: Scattering processes studied in this thesis. Energy for Feshbach molecule association (a) is provided by time-dependent magnetic fields or RF photons. In either case, the association process is coherent and the resulting ultra cold Feshbach molecules remain trapped. In contrast, three-body recombination (b) is an inelastic collision that forms a molecule and releases an amount of kinetic energy equal to its binding energy. This energy is usually sufficient to eject the resulting molecule and atom from the trap. Feshbach molecules exist in a highly excited vibrational state and they can relax to a more deeply bound state by colliding with ^{87}Rb (c) or ^{40}K (d). This releases enough kinetic energy to eject atom and molecule from the trap. The rates of processes (b) and (c) are modified by the Efimov effect due to the existence of ^{87}Rb–^{87}Rb–^{40}K Efimov trimer states.

prepared for experiments near absolute zero temperature, and how thermodynamic quantities like number and temperature of the atoms are extracted from photographs using standard absorption imaging techniques.

The next two Chapters describe the formation of ultracold fermionic ^{40}K^{87}Rb Feshbach molecules in the atomic gas (see Fig. 1.2a). Chapter 5 shows our systematic exploration of the rate and ultimate efficiency of molecule creation by magnetic-field sweeps near a Fano-Feshbach resonance. Chapter 6 shows alternative methods that were employed to make Feshbach molecules. These measurements combine to give a recipe for efficient molecule production, however they also reveal a many-body suppression of pairing and an unexpected source of heating that prevent the formation of a degenerate Fermi gas of molecules.

Chapter 7 reviews the three-body Efimov effect and the previous measurements from ultra cold atom experiments around the world. Chapter 8 focuses on our own measurements of inelastic collision rates in the atomic ^{40}K and ^{87}Rb mixture, as depicted in Fig. 1.2 (b-d). These results pinpoint the Efimov state spectrum in the ^{87}Rb–^{40}K mixture for the first time, and the location appears to deviate from the pattern established by measurements in single-species atomic gases.

Chapter 9 reviews the major results and concludes with a discussion of future experiments.

Chapter 2

Magnetically tuned interactions

A typical ultracold atomic gas is a million times less dense than air, and yet this ethereal substance is routinely made into a strongly interacting quantum system for physics experiments. Such control is made possible by magnetic Fano-Feshbach resonances, which can be used to dynamically tune the interaction strength between atoms by orders of magnitude. This phenomenon occurs when a weakly bound molecular state's energy is degenerate with two free atoms, and is reviewed here in Section 2.1. Section 2.2 introduces the ^{40}K-^{87}Rb interspecies Fano-Feshbach resonance that is central to the work in this thesis. Finally, Section 2.3 describes an important side-effect to tunable interactions near Fano-Feshbach resonances. Specifically, as pairwise interactions become stronger, few-body correlations are also enhanced and the rates of atom loss due to inelastic collisions accelerate dramatically. Inelastic collisions pose a challenge to experiments that seek to create stable, strongly interacting quantum gases. However, they also create an opportunity to study universal few-body interactions, which is an interesting and surprisingly complex problem in quantum physics.

2.1 Magnetic Fano-Feshbach resonances

The interaction strength between atoms varies by orders of magnitude as a function of magnetic field near a Fano-Feshbach resonance. Leveraging this effect to control two-body interactions, ultra cold atom experiments can access a huge variety of few- and many-body phenomena. Magnetic Fano-Feshbach resonances are an important tool for atomic physics. As such, a number of

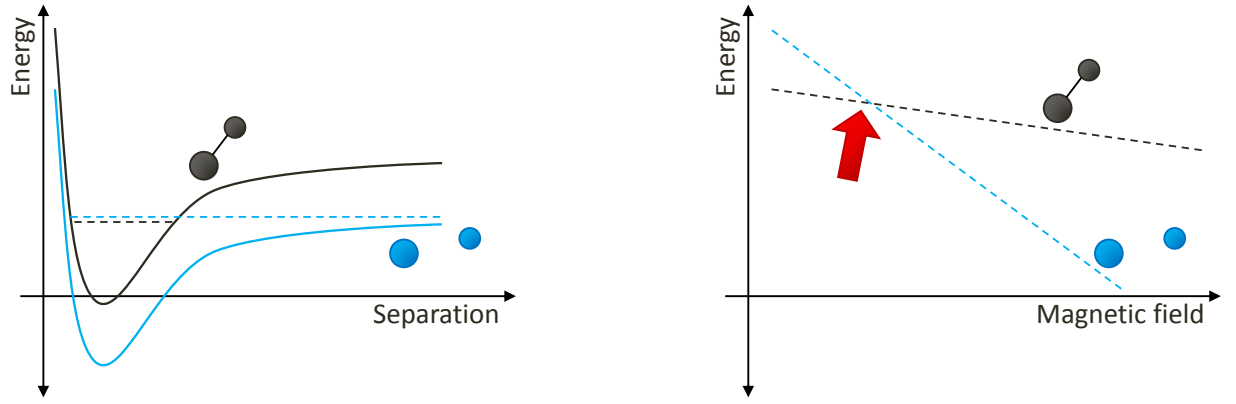

Figure 2.1: Left: Schematic interaction potentials between pairs of ultracold atoms. Right: The bound state and pair of free atoms have different magnetic moments. When their energies cross, a Fano-Feshbach resonance occurs (red arrow).

great review articles already cover the subject in detail [12, 18, 19]. This section highlights a few properties that are relevant to the observations discussed in the rest of the thesis.

A pair of ultra cold atoms can interact through a potential like the one shown in Figure 2.1 (left). For small internuclear separation, there is a hard core repulsion. At large separation, interactions are dominated by a $1/r^6$ tail characterized by the van der Waals length, r_{vdW}. Two potentials are drawn in the figure, one in which we consider a pair of free atoms (the 'entrance channel') and another with a bound state having similar energy (the 'closed channel'). Consider the free atoms, which are in a state with nonzero magnetic moment (right, Figure 2.1). As the magnetic field is varied, their energy changes too. The bound state, formed by atoms in a different Zeeman sub level, has a different magnetic moment. Coupling between the entrance and closed channels mixes the two states as their energies approach each other. A magnetic Fano-Feshbach resonance occurs when the energies are degenerate, and the strength of atom-atom interactions diverges.

And what does this atom-atom interaction look like? In the limit of zero temperature, kinetic energy vanishes. As a consequence, atoms cannot climb centrifugal barriers and collisions with nonzero angular momentum are suppressed. Spherically symmetric s-wave collisions dominate.

The interatomic scattering potential can then be renormalized as a hard sphere with radius a, such that the elastic collision cross section is $\sigma_{\rm el} = 4\pi a^2$. The interspecies scattering length a near an interspecies Fano-Feshbach resonance follows

$$a(B) = a_{\rm bg}\left(1 - \frac{\Delta}{B - B_0}\right) \tag{2.1}$$

where B is the magnetic field, $a_{\rm bg}$ is the background scattering length, Δ is the resonance width, and B_0 is the location of the Fano-Feshbach resonance [28]. Larger $|a|$ means stronger interaction, $a < 0$ is attractive, and $a > 0$ is repulsive. Although the work in this thesis is focused on Fano-Feshbach resonances that enhance s-wave interactions, many resonances also exist for higher angular momenta.

A two-body bound state called a Feshbach molecule is also associated with each resonance [29, 19]. The Feshbach molecule's binding energy, E, is determined by the scattering length, a, near a resonance.

$$E = \frac{\hbar^2}{2\mu(a - \bar{a})^2} \tag{2.2}$$

where $\hbar$ is Planck's constant divided by 2π, μ is the reduced mass of the atoms forming the molecule, and $\bar{a} = 0.96\ r_{\rm vdW}$ is the average scattering length of the system. This bound state exists when $a > 0$, with the binding energy approaching zero as a approaches infinity. Feshbach molecules belong to a universal class of 'halo states', which are named for their enormous size that can exceed the scale of inter-particle (or inter-atomic) forces [29]. Feshbach molecules play a key role in the BCS-BEC crossover in gases of ultra cold Fermions [30], and also serve as a starting point for the creation of ultra cold polar molecules [20].

Fano-Feshbach resonances are classified according to their strength [18]. For strong 'entrance channel dominated' resonances, the universal formulae 2.1 and 2.2 dominate the scattering properties over a large range of a. Near weaker 'closed-channel dominated' resonances, a competes with other interaction length scales like $R^* = \hbar^2/(2\mu a_{\rm bg}\delta_\mu\Delta)$. Here, δ_μ is the differential magnetic moment between the entrance and closed channels. These ideas are summarized by the parameter $s_{\rm res} = \bar{a}/R^*$, where $s_{\rm res} \gg 1$ belongs to an entrance channel dominated resonance and $s_{\rm res} \ll 1$

belongs to a closed-channel dominated resonance. The former type usually has $\Delta > 1$ G, leading them to be called 'broad' Fano-Feshbach resonances. These are the most useful resonances from an experimental perspective, because the scattering length is less sensitive to magnetic-field noise. Entrance channel dominated Fano-Feshbach resonances also provide the best access to universal scattering phenomena.

A huge diversity of Fano-Feshbach resonances exists across the Alkali atoms, which impacts the efficiency of evaporative cooling as well as the types of experiments available to each species [18]. For example, the Fermion ^{6}Li has the unusual configuration of three strong overlapping Fano-Feshbach resonances between the three lowest energy spin states, meaning that all possible pairwise interactions are simultaneously enhanced. Although ^{40}K's strongest Fano-Feshbach resonance is much weaker, this Fermion has better options for detection and spectroscopy thanks to the existence of a nearby spin state that is unaffected by any resonance. The Boson ^{133}Cs has a strong resonance near zero magnetic field, meaning that the gas must be cooled at a higher field to prevent the destructive inelastic collisions that accompany Fano-Feshbach resonances (see Section 2.3). This inconvenience is more than offset by the existence of several extremely strong resonances at higher magnetic fields [31]. In contrast, ^{87}Rb is a particularly easy Boson to cool but it possesses no strong Fano-Feshbach resonances at all.

2.2 The interspecies ^{40}K-^{87}Rb Fano-Feshbach resonance

Fortunately, there are several interspecies Fano-Feshbach resonances between the ^{40}K atoms and ^{87}Rb atoms. The strongest of these resonances has $s_{\rm res} = 1.9$, and is located at $B_0 = 546.62$ G with $\Delta = 3.04$ G and $a_{\rm bg} = -187\ a_0$ as measured by Ref. [32], where a_0 is the Bohr radius. Figure 2.2 plots the scattering length as a function of magnetic field. This resonance is between the $|f, m_f\rangle = |1, 1\rangle$ and $|9/2, -9/2\rangle$ states of ^{87}Rb and ^{40}K, where f is the total angular momentum and m_f its projection on the magnetic-field axis. These are the lowest energy states in a magnetic field, and so the mixture is protected against inelastic spin-changing two-body collisions.

These resonance parameters set requirements for the electromagnet systems and their cali-

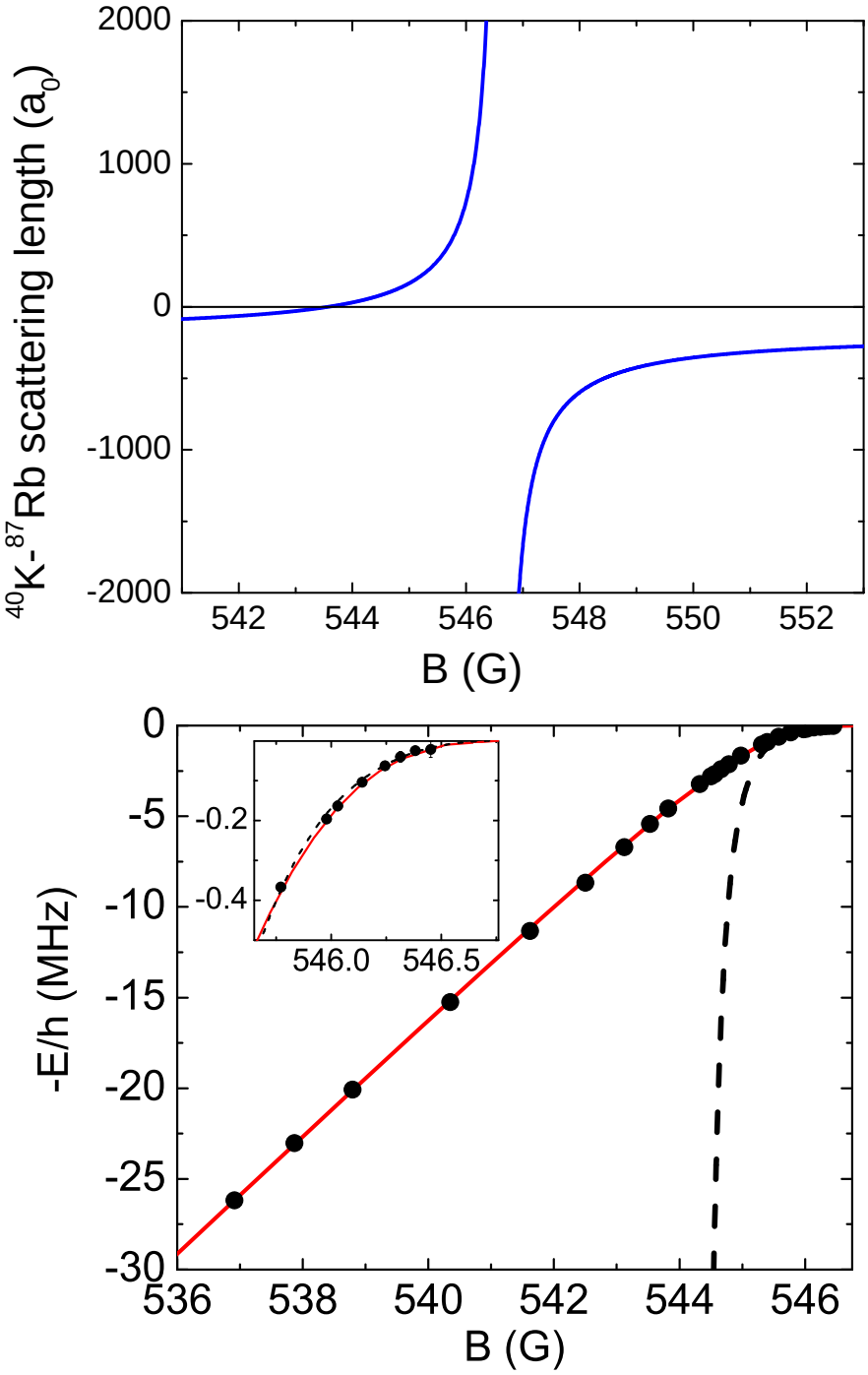

Figure 2.2: Top: The ^{40}K-^{87}Rb interspecies scattering length a as a function of magnetic field B near a magnetic Fano-Feshbach resonance, calculated using parameters measured by Ref. [32]. Bottom: The KRb Feshbach molecule energy, $-E$, as a function of B, adapted from [33]. The solid line is a coupled-channel calculation of the molecule binding energy that includes non-universal contributions from the closed-channel wave function. The dashed line indicates the universal formula for molecule binding energy (Equation 2.2), which is accurate at high scattering lengths.

bration. To access the large field B_0 (within the spatial constraints of our experiment) requires hundreds of Amps of current through coils of water-cooled hollow-core copper tubing. Chapter 3 describes the implementation of a new magnet system for this purpose. The resonance width Δ is also relatively small, which makes the scattering length quite sensitive to magnetic-field fluctuations. For example, formula 2.1 predicts a scattering length $a = 2420\ a_0$ when the magnets are turned on to a field of 546.4 G near the Fano-Feshbach resonance. The lab's ambient magnetic field changes by about 5 mG when a nearby freight elevator changes floors; this increases the scattering length to 2480 a_0, which is a noticeable shift. To avoid additional noise, the electromagnet current control is constructed to achieve better than 10 ppm fractional instability.

For our purposes, the most useful range near the Fano-Feshbach resonance is where the interspecies scattering length a_{KRb} dominates over all other length scales and interactions are universal. This is bounded from below by the interspecies van der Waals length $r_{\mathrm{vdW}} = 72\ a_0$. Figure 2.2 shows how the KRb molecule binding energy deviates from Eqn. 2.2 at low scattering lengths. For three-body ^{87}Rb–^{87}Rb–^{40}K interactions, the nearly magnetic-field independent ^{87}Rb–^{87}Rb scattering length $a_{\mathrm{RbRb}} = 100\ a_0$ also plays a role. The useful range for a_{KRb} is bounded from above by either the thermal deBroglie wavelength $\lambda_{\mathrm{dB}} = h/\sqrt{3\mu k_{\mathrm{B}} T}$ or the mean inter-particle spacing $n^{1/3}$, whichever is smaller. Here, h is Planck's constant, $\mu = 27.4$ amu is the reduced mass of ^{40}K and ^{87}Rb, k_{B} is the Boltzmann constant, and T is the temperature. For a typical gas mixture at $T = 500$ nK and mean density $n = 5 \times 10^{12}$ cm^{-3}, we have $\lambda_{\mathrm{dB}} = 13000\ a_0$ and $n^{1/3} = 11000\ a_0$.

2.3 Inelastic loss: the cost of tunable interactions

A gas of ultra cold neutral atoms is really in a metastable state, beneath which lies a zoo of two-body bound states (Fig. 2.3). Inelastic scattering into one of these states converts binding energy to kinetic energy, which can propel atoms out of the trap entirely. At least three atoms are required for a collision to form a bound state while conserving energy and momentum. The odds of such a few-body encounter are predicted to increase dramatically with the magnitude of the interspecies scattering length, a (Table 2.1). Although gases with only one or two types of

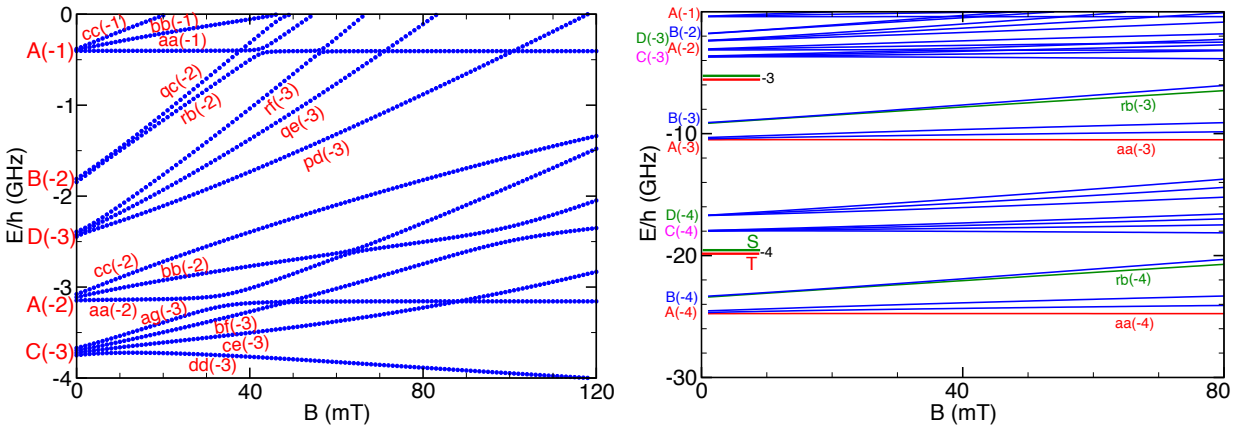

Figure 2.3: A zoo of bound states in the ^{40}K-^{87}Rb mixture with binding energies 0 to 3 GHz (left) and 0 to 30 GHz (right). Inelastic scattering into these bound states leads to atom loss, since a typical optical trap for our experiments can only hold atoms with a kinetic energy of $h\times$20 kHz or less. The magnetic Feshbach resonance that we use in our experiments is at a magnetic field of 54.6 mT. Adapted from [34].

Table 2.1: Three-body inelastic scattering processes in the ^{40}K-^{87}Rb mixture near an interspecies Fano-Feshbach resonance and their universal scaling with interspecies scattering length [35]. In these reactions, ^{40}K^{87}Rb denotes the Feshbach molecule state and (^{40}K^{87}Rb)' denotes a more deeply bound state like the ones in Figure 2.3. The processes are categorized by quantum statistics where 'B' are identical ^{87}Rb atoms (Bosons), 'F' are identical ^{40}K atoms (Fermions), and 'X' are distinguishable atoms in a third state. In practice, the role of 'X' can be played by a ^{40}K atom in a different spin state.

Process			Type	Predicted Scaling
^{87}Rb+^{40}K+^{40}K	$\rightarrow$	^{40}K^{87}Rb+^{40}K	B+F+F Three-body recombination	a^6
^{40}K+^{87}Rb+^{87}Rb	$\rightarrow$	^{40}K^{87}Rb+^{87}Rb	B+B+F Three-body recombination	a^4
^{40}K^{87}Rb+^{40}K	$\rightarrow$	(^{40}K^{87}Rb)'+^{40}K	F+BF Atom-molecule relaxation	$a^{-3.12}$
^{40}K^{87}Rb+^{87}Rb	$\rightarrow$	(^{40}K^{87}Rb)'+^{87}Rb	B+BF Atom-molecule relaxation	a^1
^{40}K^{87}Rb+X	$\rightarrow$	(^{40}K^{87}Rb)'+X	X+BF Atom-molecule relaxation	a^{-1}

Fermions are protected by the Pauli Exclusion principle, inelastic collisions and atom loss can rapidly deplete strongly interacting Bose gases, Bose-Fermi mixtures, or Fermi mixtures with more than two distinguishable states. The ^{40}K-^{87}Rb mixture's most prevalent inelastic loss mechanisms are three-body recombination and atom-molecule vibrational relaxation.

In three-body recombination, three atoms collide to produce a two-body bound state, with a kinetic energy equal to the binding energy distributed between the molecule and third atom. This process can form a deeply bound molecule at negative scattering lengths and either a deeply bound molecule or a Feshbach molecule at positive scattering lengths. In either case, all three atoms are typically propelled out of the sample. A Fano-Feshbach resonance amplifies three-body recombination for any triplet of atoms where at least two pairwise interactions are strong. In fact, the resonant loss of atoms as a function of magnetic field is one of the most common signals used to search for Fano-Feshbach resonances in quantum gases [18]. In the case of the ^{40}K-^{87}Rb mixture, B+F+F recombination (

) is suppressed by the Pauli exclusion principle and B+B+F recombination (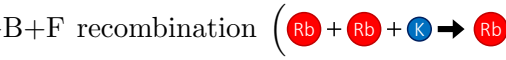

) dominates the inelastic loss.

Atom-molecule vibrational relaxation occurs in quantum gas mixtures of atoms and Fesh-

bach molecules. When an atom collides with a molecule, the molecule can relax to a more deeply bound state like the ones in Fig. 2.3. This process releases the difference in the molecule's binding energy as kinetic energy, invariably propelling atom and molecule out of the trap. As is the case with three-body recombination, quantum statistics play a role in determining which molecule relaxation collisions are enhanced near an interspecies Fano-Feshbach resonance. F+BF relaxation  is suppressed by the Pauli exclusion principle and B+BF relaxation  dominates near the Fano-Feshbach resonance.

Three-body recombination and atom-molecule relaxation rates constrain the possible experiments that can be performed at strong interactions. This is particularly true for three-body recombination, which scales as a^4 and quickly overwhelms thermalizing elastic collisions that only scale as a^2. This means that ^{40}K-^{87}Rb gases at high scattering lengths can be depleted by inelastic loss before even reaching thermal equilibrium. Chapters 5 and 6 of this thesis will describe the optimization of Feshbach molecule formation, which is another dynamical process that competes against these inelastic loss timescales. A quantitative understanding of the loss rates is useful to these experiments. On a more positive note, the rates of three-body recombination and atom-molecule relaxation are sensitive probes of three-body correlations. Chapters 7 and 8 will explore how the presence of three-body bound states modulates the scaling laws in Table 2.1, giving rise to sequences of resonances that occur near most Fano-Feshbach resonances. Before I describe any of these results, however, the next two Chapters will summarize how we prepare our quantum gas mixtures for experiments.

Chapter 3

An improved electromagnet system for trapping and manipulating atoms

Electromagnets are essential to the work in this thesis. Large, homogeneous, and stable magnetic fields enable tunable interactions near the interspecies ^{40}K-^{87}Rb Fano-Feshbach resonance at 547 G. Magnetic traps are the workhorses of the cooling sequence, which collects atoms from a hot vapor and creates a gas at less than one millionth of a degree above absolute zero temperature. Reliable atom state preparation, spectroscopy, and imaging also depend on stable magnetic fields. This Chapter introduces an electromagnet system that improves the magnetic trapping and control capabilities of our apparatus. Optical access is also enhanced, which paves the way for new methods to image and manipulate the atoms in future experiments. Section 3.1 describes the electromagnetic coils and the fields they individually produce. Section 3.2 is about the high-current control system. In Section 3.3, water cooling and thermal dissipation are discussed.

3.1 The magnetic coils

The idea to build a new magnetic trap was sparked when a worn piece of electrical insulation suddenly caused bursts of electrical current to arc across an air gap into the grounded surface of the old trap's supporting structure. The failure occurred deep inside of the trap assembly, which had to be painstakingly deconstructed and surgically repaired. Although the old trap was temporarily revived, a safer and more robust mechanical structure was clearly needed. We took advantage of the redesign to improve other aspects of the trap as well. The old copper support structure had a large electrical inductance that limited the speed of the magnet system. We replaced it with a

rigid Garolite G-10 phenolic support that has negligible electrical conductivity. The old system only ran cooling water through the support structure. Now, the chilled water runs through the hollow cores of the copper wires themselves, which provides more uniform thermal dissipation with a smaller spatial footprint. To improve experiments near Fano-Feshbach resonances, the new design also features a pair of Helmholtz coils that we can turn on independently of the other trap coils to provide a homogeneous field while the atoms are confined in an optical trap. The design of these new coils was detailed in Ty Cumby's thesis [36]. Tracy Keep from the JILA instrument shop precisely wound the coils and mounted them to their rigid frame. Here, I will describe their testing and implementation. This section describes characterization of the fields produced by the coils when they are conducting a few hundred Amps of electrical current, which is their normal mode of operation during an experiment.

The new magnet system is arranged in a Ioffe-Pritchard configuration [37] as shown in Fig. 3.1. It consists of three pairs of coils, and it is designed to trap the atoms at a magnetic-field minimum. The tight trapping radial directions are labeled x and y, and the weak axial trapping direction along the axis of the Pinch and Bias coils is labeled z. Near the center, the Pinch coil pair creates a magnetic field whose z-component follows $B_z = B_{\mathrm{P0}} + \frac{1}{2}\gamma(z^2 - \frac{x^2+y^2}{2})$. The field offset B_{P0} and curvature γ are both proportional to the electrical current in the Pinch coils. A pair of Bias coils in Helmholtz configuration contributes a homogenous $B_z = -B_{\mathrm{B0}}$ in the z direction, the strength of which is likewise proportional to the current through the Bias coils. The dominant contribution from the Ioffe coils is a linear quadrupole field in the radial directions, $B_x = \beta x$ and $B_y = -\beta y$.

These fields combine to form a harmonic trap with potential $U = \frac{1}{2}m\omega_x^2 x^2 + \frac{1}{2}m\omega_y^2 y^2 + \frac{1}{2}m\omega_z^2 z^2$ in the region near the center. Following Pritchard [37], the trap frequencies are approximately

$$\omega_x = \omega_y = \sqrt{\frac{\mu}{m}\left(\frac{\beta^2}{B_0} - \frac{\gamma}{2}\right)} \tag{3.1}$$

$$\omega_z = \sqrt{\frac{\mu}{m}\gamma} \tag{3.2}$$

for a magnetic moment μ, mass m, and magnetic-field minimum $B_0 = B_{\mathrm{P0}} - B_{\mathrm{B0}}$. In an experiment, the ^{87}Rb and ^{40}K atoms are both trapped in states that have $\mu = \mu_{\mathrm{B}}$, where μ_{B} is the Bohr

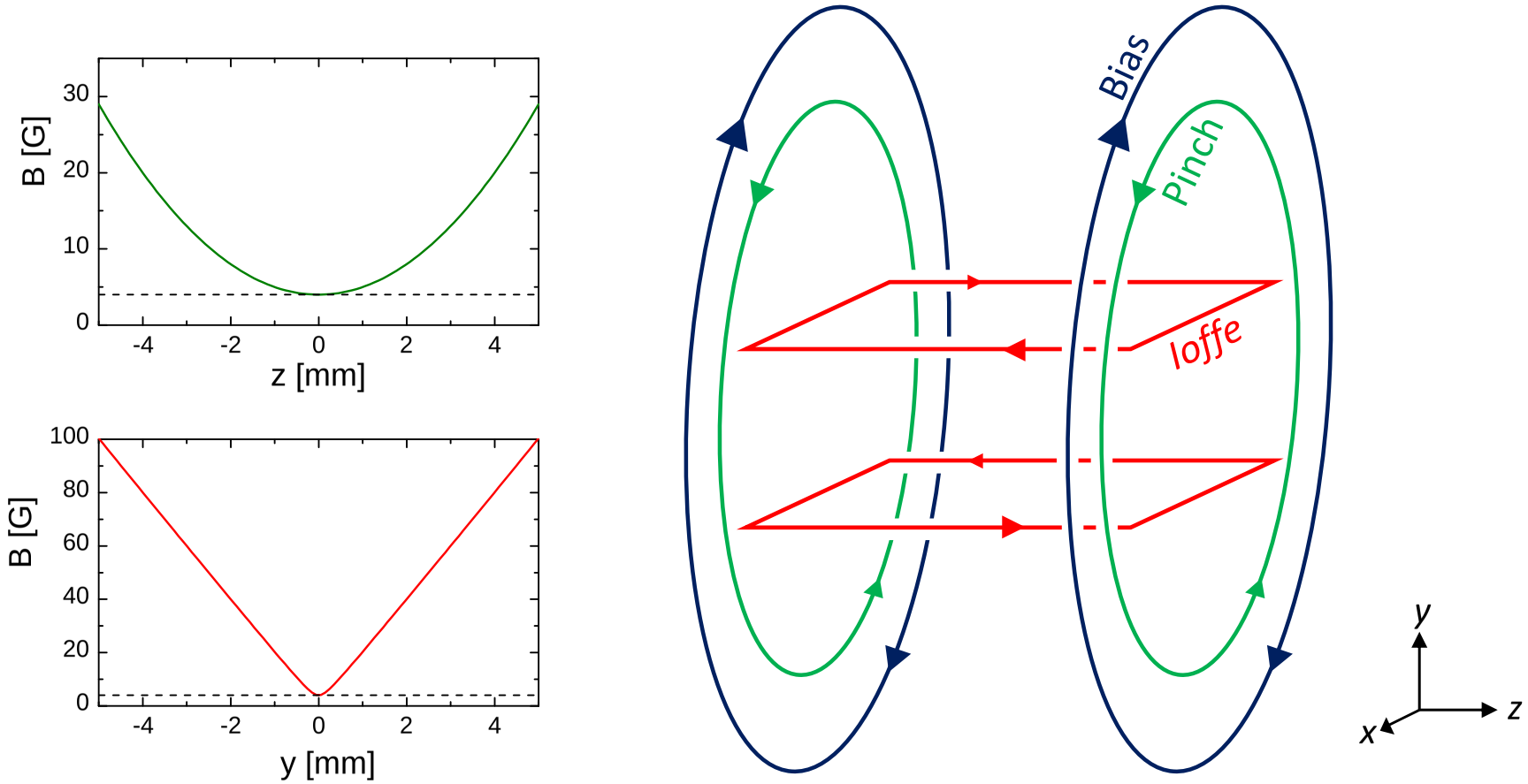

Figure 3.1: Left: Calculated magnitude of the trap magnetic fields for $x = y = 0$ (top) and for $x = z = 0$ (bottom). The atoms are trapped at the field minimum at the center. Right: Arrangement of coils in the Ioffe-Pritchard magnetic trap. The Pinch coils create an axial field with a curvature and the opposing Bias coils subtract a constant field to bring the value at the center of the trap down to 4 Gauss. The Ioffe coils create a radial quadrupole field to confine the atoms in the radial directions. The Bias coils can also be turned on alone, which generates a large homogeneous magnetic field.

magneton. For typical magnetic trap currents, the trap frequencies are $\omega_x = \omega_y = 125$ Hz and $\omega_z = 18$ Hz.

To better understand the magnet system, we constructed a test setup to measure β, γ, B_{P0}, and B_{B0}. One coil pair at a time was connected to a high-current power supply and a water cooling line while an F.W. Bell Gauss/Tesla meter on a three-axis translation stage was used to map out the field between the coils. Table 3.1 lists the results and Figure 3.2 shows some of the measurements. We measured the Ioffe coil pair's magnetic-field gradient to be 89.7(2) G/cm in the radial y direction near the trap center, at a current of 90.0 A. The Pinch field was mapped out in the x-z plane for near the center of the trap at a current of 100 A. A two-dimensional surface fit to the equation $B_z = B_{\mathrm{P0}} + \frac{1}{2}\gamma(z^2 - x^2/2)$ gave $\gamma = 106(2)$ G/cm^2 and $B_{\mathrm{P0}} = 334(1)$ G. At a current of 160 A, the Bias coils made a field of 524(1) G. All of the measured values were close to the predictions based on models of the coils [36].

The scattering properties of ultracold ^{40}K and ^{87}Rb atoms are particularly sensitive to magnetic fields during phases of the experiment where only the Bias coils are turned on. A good calibration of this field is especially important. Figure 3.3 shows a map of the Bias field for an electrical current of 163 A, near the interspecies Fano-Feshbach resonance, as measured by spatially resolved RF spectroscopy on an elongated ^{40}K cloud in an optical trap. We used the $|f, m_f\rangle = |9/2, -9/2\rangle \rightarrow |9/2, -7/2\rangle$ transition resonance to identify the magnetic-field values. The dashed line indicates a 0.079(3) G/cm gradient along the axial z direction. The solid line indicates a curvature of $3.2(6) \times 10^{-7}$ G/cm^2, which corresponds to a confining trapping frequency of 0.01 Hz for the ^{40}K atoms in the $|9/2, -9/2\rangle$ state that we use for our experiments. Although the Bias coils and leads were carefully designed [36] to generate no magnetic-field gradient, this value is just over half of the stray gradient that existed with the previous Bias system. It is possible that the residual gradient is caused by a magnetized object near the atoms. This could be tested by measuring the gradient at a different Bias field to see if it is proportional to the Bias current. In any case, the gradient is acceptably small for the applications in this thesis. External gradient-compensating coils may be required in future work.

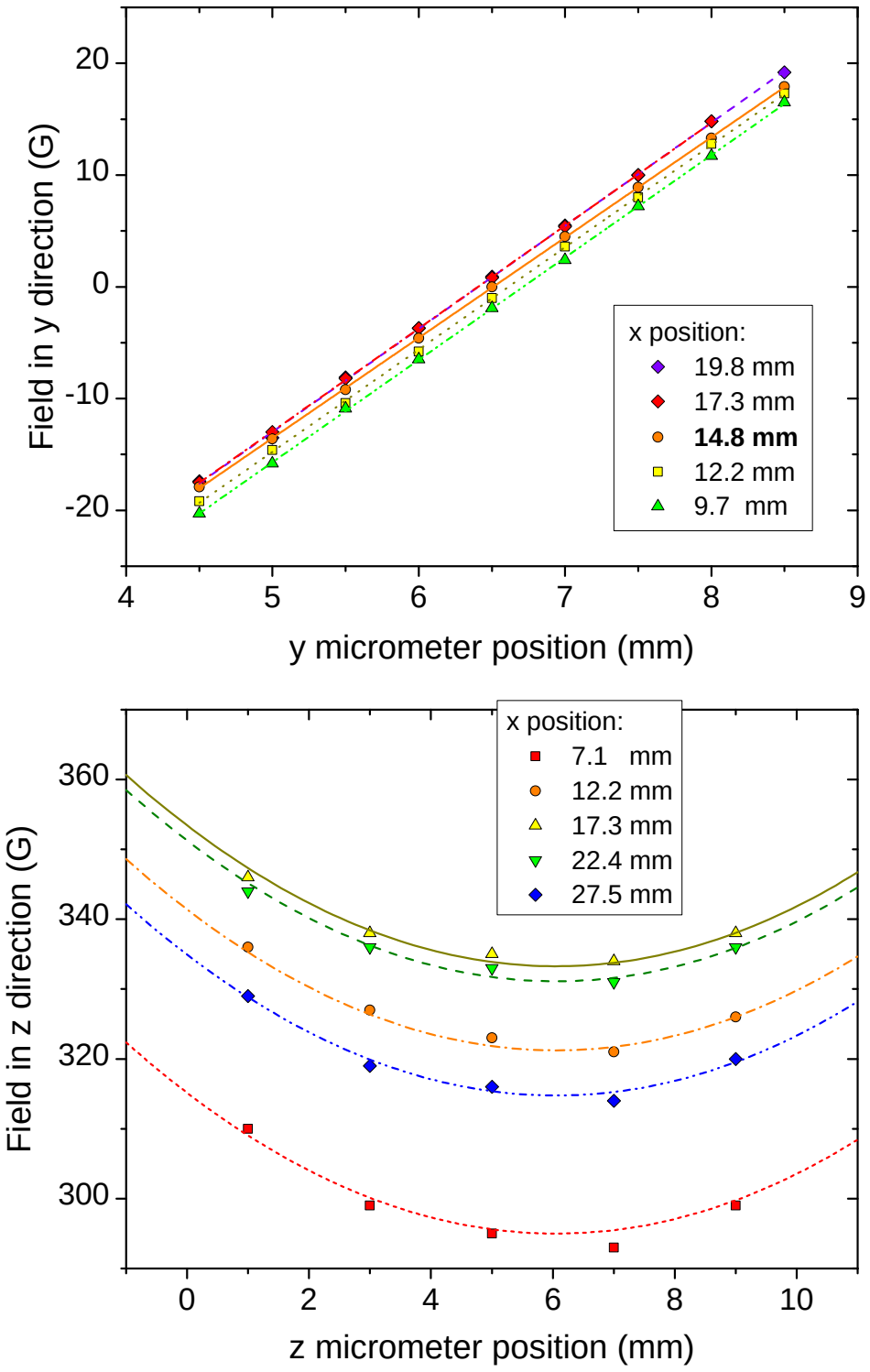

Figure 3.2: Top: Measurements of the gradient from the Ioffe coils at 90 Amps (points) with linear fits to extract the field gradient (lines). Bottom: Measured curvature from the pinch coils at 100 Amps. The lines show the result of a surface fit to the data. For both plots, the positions include arbitrary offsets due to the initial positions of the micrometers.

Table 3.1: Measured parameters of the fields from the new magnetic coil system. I denotes the current through the relevant coil. Error bars are statistical.

Parameter	Variable	Model [36]	Measured value	Units
Ioffe radial gradient	β/I	1.00	1.00(2)	G/cm/A
Pinch axial curvature	γ/I	1.06	1.06(2)	G/cm^2/A
Pinch axial field	B_{P0}/I	3.48	3.34(1)	G/A
Bias axial field	B_{B0}/I	3.32	3.306(1)	G/A
Bias axial gradient	β_{B0}/I		$4.8(2)\times10^{-4}$	G/cm/A
Bias axial curvature	γ_{B0}/I		$2.0(4)\times10^{-9}$	G/cm^2/A

RF spectroscopy is also the tool of choice for calibrating the field's absolute value. A combination of measurements on the ^{87}Rb $|2,2\rangle \rightarrow |1,1\rangle$ microwave transition and the ^{40}K $|9/2,-9/2\rangle \rightarrow |9/2,-7/2\rangle$ transition over a range of magnetic-field values gives the calibration, $B_{\mathrm{B0}} = 0.36(5)\mathrm{G} + \mathrm{I} \times 3.306(3)\mathrm{G/A}$ where B_{B0} is the Bias coil field in units of G, I is the current in units of A, and the error bars are statistical. The offset is presumably caused by the Earth's magnetic field, which is oriented along the axis of the Bias coils.

3.2 The high-current control system

The electrical currents are another key part of the magnet system. At various stages of the experiment, the magnetic fields from different coils need to be ramped on and off in repeatable sequences. We accomplish this by placing an Insulated Gate Bipolar Transistor (IGBT) in series with each current path as shown in Figure 3.4 and controlling the gate voltages with servo electronics. The priorities for the new control electronics are low noise, low sensitivity to RF interference, and reliability. This section describes the transistors, sensors, cabling, and servos that make it all work.

The magnet coils are wired in two parallel paths with the Bias coils in one path and the Ioffe and Pinch coils in the other (Fig. 3.4). The entire high-current system is powered by one Agilent 6690A power supply, which can provide up to 440 A at 15 V. The power supply provides a constant voltage and the transistors control the currents through each path. There are two main modes of operation. First, to form a magnetic trap, both current paths are turned on to about

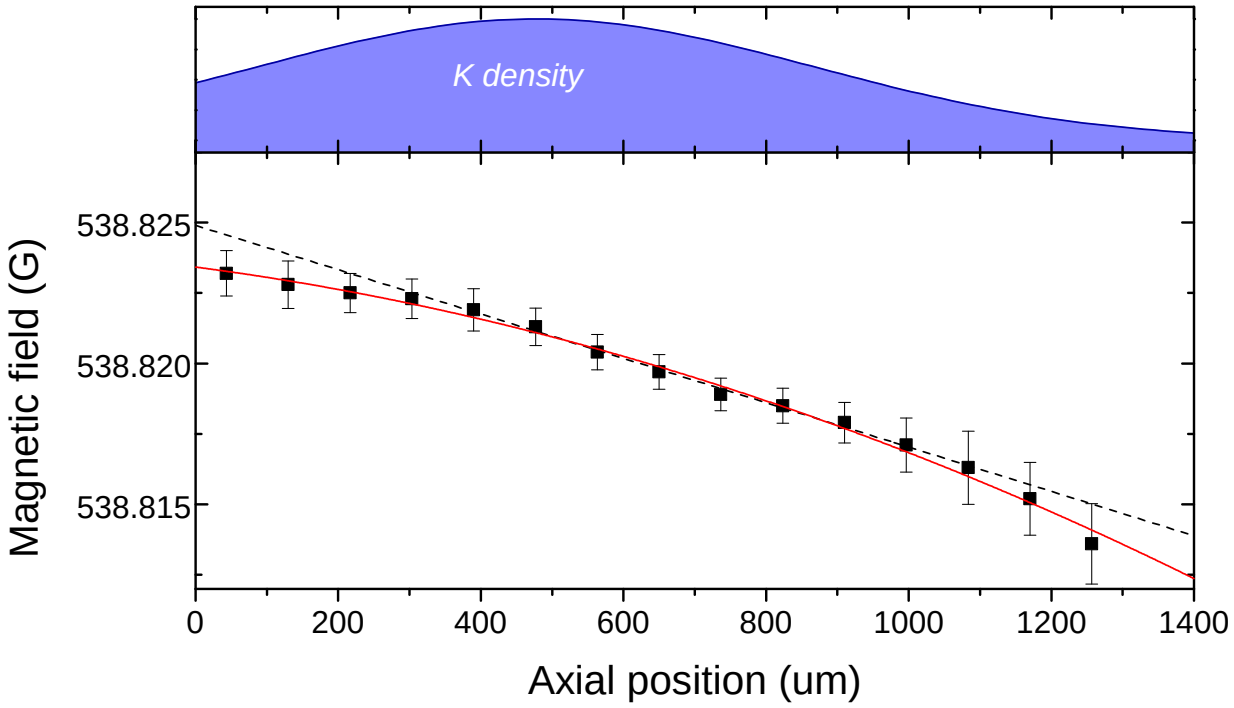

Figure 3.3: Using RF spectroscopy on a gas of ^{40}K atoms, we measure the Bias magnetic field as a function of axial position. A fit to the central linear region gives a field gradient of 0.079(3) G/cm for an average magnetic field close to the interspecies ^{40}K-^{87}Rb Fano-Feshbach resonance (black dashed line). A fit to the entire data set gives a field curvature of $3.2(6) \times 10^{-7}$ G/cm^2. Zero position on the x axis represents the edge of the imaging camera.

200 A. Second, most experiments are eventually performed in an optical trap with a homogenous magnetic field close to the interspecies Fano-Feshbach resonance. This requires 160 A of current through the Bias coils while the Ioffe and Pinch coils are turned completely off.

Previous high-current electromagnets in our group had pushed power transistors to their limits such that a failure occurred every few months, one of which even started a small fire. To handle high current loads it was also necessary to connect several transistors in parallel. Progress in the power electronics industry has made these problems obsolete. There is now a variety of high-power transistors to choose from that can individually handle the maximum output of our power supply. For the same price point and physical size, Metal Oxide Semiconductor Field Effect Transistors (MOSFETs) are typically faster and can handle the highest currents, but they are also more easily damaged by transient voltage swings. Insulated Gate Bipolar Transistors (IGBTs) are popular in arc welding applications because they can typically survive several thousand volts across the conduction path. Since the inductive backlash of quickly turning off our electromagnets pushes hundreds of Volts onto the transistors, and because the sizable inductance and capacitance of the magnet coils prevents us from taking advantage of a MOSFET's fast response, we use IGBTs.

Specifically, the SKM400GA-12V IGBT model by Semikron is used for IGBTs 1 and 2 in Figure 3.4. They each have three terminals: Gate (G), Emitter (E), and Collector (C). A positive G-E voltage turns the device on, allowing current to flow from C to E. A 30 Ohm resistor is attached to each gate to smooth out the turn-on behavior of the circuit. The transistor is rated for V_{CE} up to 1.2 kV, so no additional protection circuitry is needed for the high-current path. Like a MOSFET, however, the IGBT is easily damaged by transient gate voltages so a 20 V back-to-back TVS diode is placed between terminals G and E. These IGBTs enter a linear mode of operation that is well-controlled by a servo when $V_{\mathrm{CE}} > 2$ V, and so we choose the output voltage of the high-current supply such that V_{CE} is at least 3 V on each IGBT. Since the magnetic trap operates with 200 A of current through each current path, each transistor dissipates 600 W of power. To protect the IGBTs from thermal overload, we mount them to a water-cooled plate as discussed in Section 3.3.

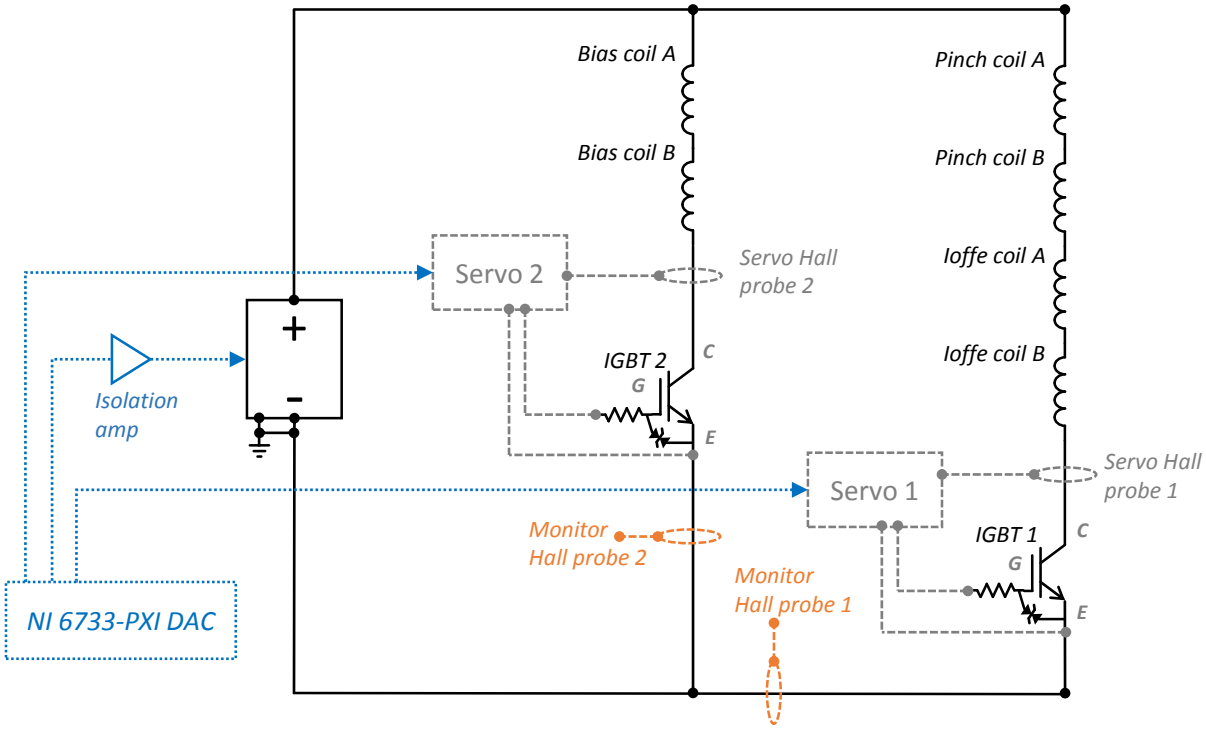

Figure 3.4: Electrical schematic for the new magnet system. Solid lines indicate the high-current path. The current through each path is controlled by a SKM400GA-12V transistor (IGBTs 1 and 2). A feedback loop consisting of a Hall effect current sensor (Danfysik IT-600s) and a servo controls the Gate-Emitter voltage of each IGBT to achieve the desired current. A LabVIEW program controls the NI PXI-6733 DAC, which in turn outputs analog voltages to control the power supply voltage and the current through each path. We use out-of-loop 'monitor' hall probes, which are identical to the in-loop 'servo' hall probes, to measure the current without making any connection to the ground of the control system.

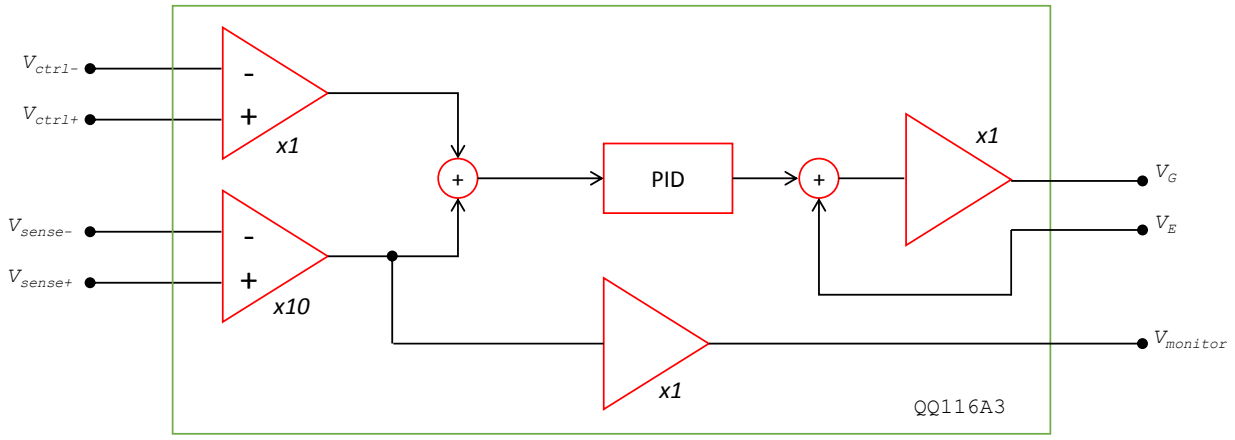

Figure 3.5: Diagram of the feedback electronics ('Servo 1' and 'Servo 2' in Figure 3.4) used to control the magnetic trap currents. The circuit was designed by Terry Brown and James Thompson, and a complete schematic can be found under the reference number 'QQ116A3' in the JILA electronics shop.

The Gate-Emitter voltage of each IGBT is controlled by a QQ116A3 coil driver servo from the JILA electronics shop, which we configure for unipolar operation. Figure 3.5 shows a simplified schematic. There are two differential voltage inputs to the servo: a sense voltage, V_{sense}, that is proportional to the measured electrical current; and a control voltage, V_{ctrl}, which is generated by a National Instruments PXI-6733 DAC installed in our main experiment control computer. Each of these voltages goes through a buffer as soon as it enters the servo. The sense buffer has gain of 10 and the control buffer has gain of 1. The buffered signals are added to each other to generate an error signal, which is fed into a Proportional-Integral-Differential (PID) filter. The PID output is then fed to an output buffer stage. This two-terminal output connects to the IGBT's Gate and Emitter with a twisted pair of wires. Because the servo's Emitter connection is isolated from the servo ground, the high-power and low-noise paths are also isolated from each other. A secondary output, V_{monitor}, samples and buffers the sensor input so that we can monitor the current.

We measure the current in each path using a Hall effect current sensor[1] . A precision 2.5 Ohm resistor measures the sense current, and the resulting sense voltage is connected by a twisted

[1] Each current sensor is a IT 600-s ULTRASTAB probe, which produces a sense current equal to 1/1500 of the measured current. Although this probe is rated to a much higher current than we require, it was chosen for its superior resistance to thermal drift.

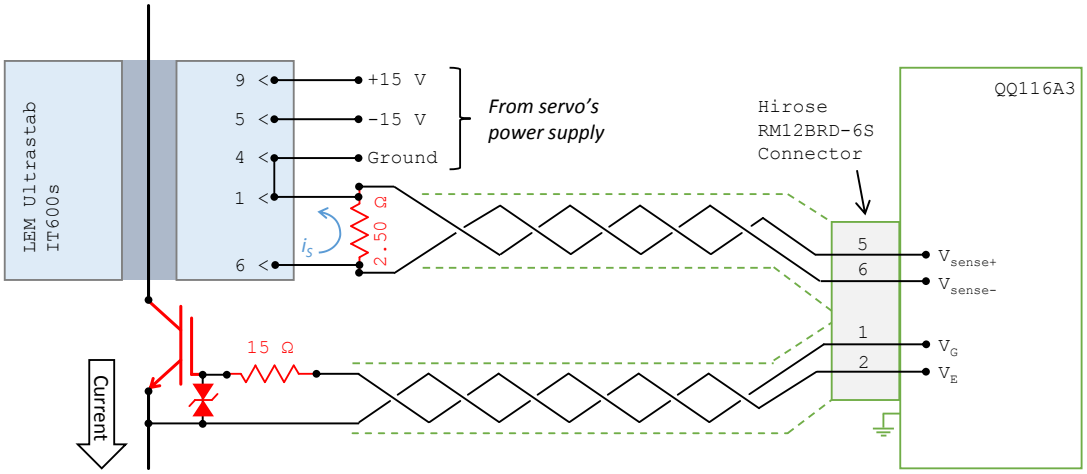

Figure 3.6: Connections between a servo, IGBT, and Hall effect current sensor. Green dashed lines show grounded shielding around each cable.

shielded cable to the servo's sense input. Since the servo's sense buffer amplifies the signal by a factor of ten, the control voltage into the servo commands a current of 30 A/V. Hall effect current sensors are useful for measuring high currents because they can be electrically isolated from the circuit being measured. One downside is that they can consume significant power when sensing larger currents. The original design placed the sense resistor to measure the Hall current sensor output inside of the servo, but we found that the heat dissipated in the resistor caused drifts in the servo electronics. Instead, the sense resistor should ideally be placed on a heatsink near the probe. Similarly, the power supply for the Hall probe, which had previously been connected through the servos, was rerouted through a separate box to avoid thermal drifts.

Nearly all of our experiments use pulses of radio and microwave radiation to manipulate or detect the atoms' states. These signals can interfere with sensitive laboratory equipment, which pick up the radiation and rectify it into DC drifts. RF rectification is a particularly tricky problem for magnetic-field servos, where a small DC drift in V_{sense} or V_{ctrl} changes the magnetic field at the atoms. This can noticeably alter the atoms' interactions with each other or entirely disrupt the radiation's interaction with the atoms by shifting the Zeeman resonance. The new control system attacks RF rectification in four ways. First, each servo is constructed in its own well-shielded

aluminum NIM module. We sandblast the anodization on the backside of the front panel to ensure a good electrical connection to the rest of the module as well as to the grounded rack. The NIM rack itself is mounted away from RF amplifiers and synthesizers. Second, we use a dedicated power supply for the servos and Hall probes to minimize the paths by which RF can enter the system. Third, signal paths outside of the servo are transmitted by twisted pairs of wires with grounded shielding (Figure 3.6). The one exception is the control voltage signal, which is transmitted over a coaxial BNC cable. All cables are kept as short as possible. Fourth, RF choke filters are installed wherever any signal or power supply connects to the servo. The filters, which are similar to Π filters, are screwed directly into the grounded case of the servo (complete diagrams are included in the servo's schematic in the JILA electronics shop, under reference QQ116A3). These strategies appear to be successful. We measure RF rectification from a relatively high power square pulse on the ^{40}K $|9/2, -9/2\rangle \rightarrow |9/2, -7/2\rangle$ transition near 80 MHz (Rabi frequency $\Omega = 2\pi \times 15$ kHz), and find that the radiation shifts the measured magnetic field by less than 10ppm as measured by the atoms.

3.3 Power dissipation and water cooling

Under magnetic trap operating conditions, the high-current power supply outputs 400 A at 8V. With this much power dissipated in the magnetic trap system and servo electronics, heating is a serious concern. Runaway heating can occur because copper's resistance increases with temperature. The new electromagnet system is designed for 'walk-away safe' steady-state power dissipation: under normal conditions the system can be turned on for an arbitrary amount of time, and if an anomalous temperature or cooling water flow rate is detected then the system turns itself off. This gives experiments maximum flexibility in terms of duty cycle, plus the magnet system is protected from programming errors, cooling failures, or other accidents. A combination of coil design, water cooling, low-resistance cabling, choice of control electronics, and safety interlocks are used to accomplish this.

Power dissipation in the magnetic coils themselves is particularly important because they

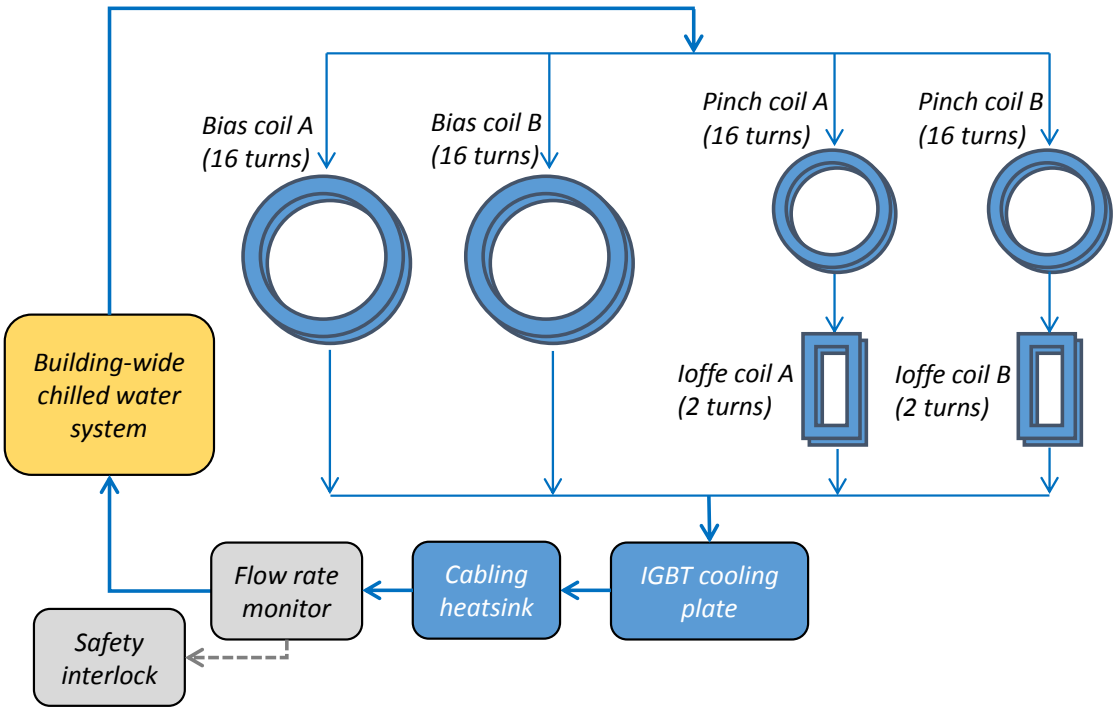

Figure 3.7: Schematic of the electromagnet water-cooling circuit. Water is split into four parallel paths to improve the efficiency of cooling. The heated water from the coils is recycled through a water cooling plate and used to cool the IGBTs. A Proteus 800-series flow rate monitor is connected to a safety interlock so that the high-current power supply is turned off in the event of a water cooling failure. All water connections through non-conducting paths are made with flexible poly-flo tubing and push-to-connect plumbing fittings.

are the most time-consuming parts to replace if something goes wrong. Each coil is wound from copper tubing with a square cross section that is 1/8 inch per side [36]. Water flows through the center of the tubing in a round channel to carry away heat. Previous designs of similar magnet coils at JILA involved 3/16 inch tubing, however the smaller 1/8 inch cross section was chosen to make the coils as small and close to the atoms as possible. This choice has paid off in terms field strength for a given operating current. For example, to reach the Fano-Feshbach resonance with the new Bias coils requires less than half of the current that was needed with the previous larger 'Helmholtz' coils. To simultaneously connect electricity and water, leads at the end of each coil are soldered to 1/4" round copper tubing, which passes through a copper block to which high-current wires are bolted. This configuration has the nice side effect of water-cooling the ends of the high current cabling as well.

Process cooling water flows through the coils in four parallel paths as shown in Figure 3.7. This scheme ensures that cold water is delivered to each coil. At room temperature each Bias coil has a measured electrical resistance of 9.3 mΩ, whereas each Pinch coil has 6.1 mΩ and each Ioffe coil only has 1.5 mΩ. We measure these resistances between points near the junctions between square and round copper tubing at the ends of the coils. Since each coil is wound from the same tubing, and each water cooling path has a similar electrical resistance and electrical current, the parallel water paths also have similar steady-state power dissipation and resistance to water flow. However, the Bias coils have the highest resistance and operating temperature, so we use them to characterize the water cooling system.

Figure 3.8 shows the steady-state operating temperatures of the Bias coils for the range of electrical currents that can be produced by the Agilent 6690A power supply. We take these measurements under typical laboratory conditions, where the process cooling water is supplied with 65 psi of pressure and a temperature of 13 C. We measure the temperatures at the hottest points on the coils, which are at the ends of the copper tubing where water flows out of each coil. The electromagnet system has two modes of operation. In trap mode, it draws a total of 400 A, where 200 A flows through each of the parallel paths shown in Figure 3.4. When the Bias coils

are turned on alone to manipulate optically trapped atoms near the interspecies Fano-Feshbach resonance, they draw 160 A. Under both conditions, we can see that the coils' temperatures heat to near room temperature.

In addition to the coils, about 2 kW of power is also dissipated in the servo IGBTs and high-current wiring in the steady-state magnetic trap. We mount the control IGBTs together on a single water-cooling plate. We were unable to destroy any transistors in testing steady-state dissipation of up to 1 kW per (water-cooled) transistor, and neither of the IGBTs has failed after a year of regular use in the experiment. At this point, it seems safe to conclude that the power is adequately dissipated at the IGBTs. Somewhat unsurprisingly, the hottest parts of the high-current systems are those without any water cooling, namely the leads. Current is delivered from the power supply to the coils by flexible braided copper 4/0 welding cables and copper bus bars. The wires themselves have a resistance of 49 $\mu\Omega$/ft at room temperature. As measured on our installed cabling at room temperature, a crimp joint that attaches a copper lug to the end of a 4/0 welding cable has an average resistance of 50 $\mu\Omega$. The Y-connections where the power supply cables are split into the two current paths (see Figure 3.4) contain three such crimps in close proximity, plus additional resistance where the lugs are bolted together. This concentration of higher resistances leads to localized heating which, in turn, increases the resistance and therefore leads to more heating. Although we did not observe any effect on the stability of the current, the steady-state temperatures of these joints make them painful to the touch. Therefore, for safety, we heat sunk the junctions to small cooling blocks connected to the exhaust of the process cooling water (Figure 3.7).

Due to the high currents flowing through the system, a water cooling failure can quickly damage the coils and IGBTs or even start a fire. We implemented a safety interlock to turn the power supply off in the event of such a problem. The most common cooling failures are building-wide pressure drops in the chilled water supply. A Proteus 800 series flow meter trips the interlock when the water flow rate falls below a safe value. Other types of failures, like clogs in certain tubes, programming errors, or loosened connections, don't effect the overall flow rate but have caused

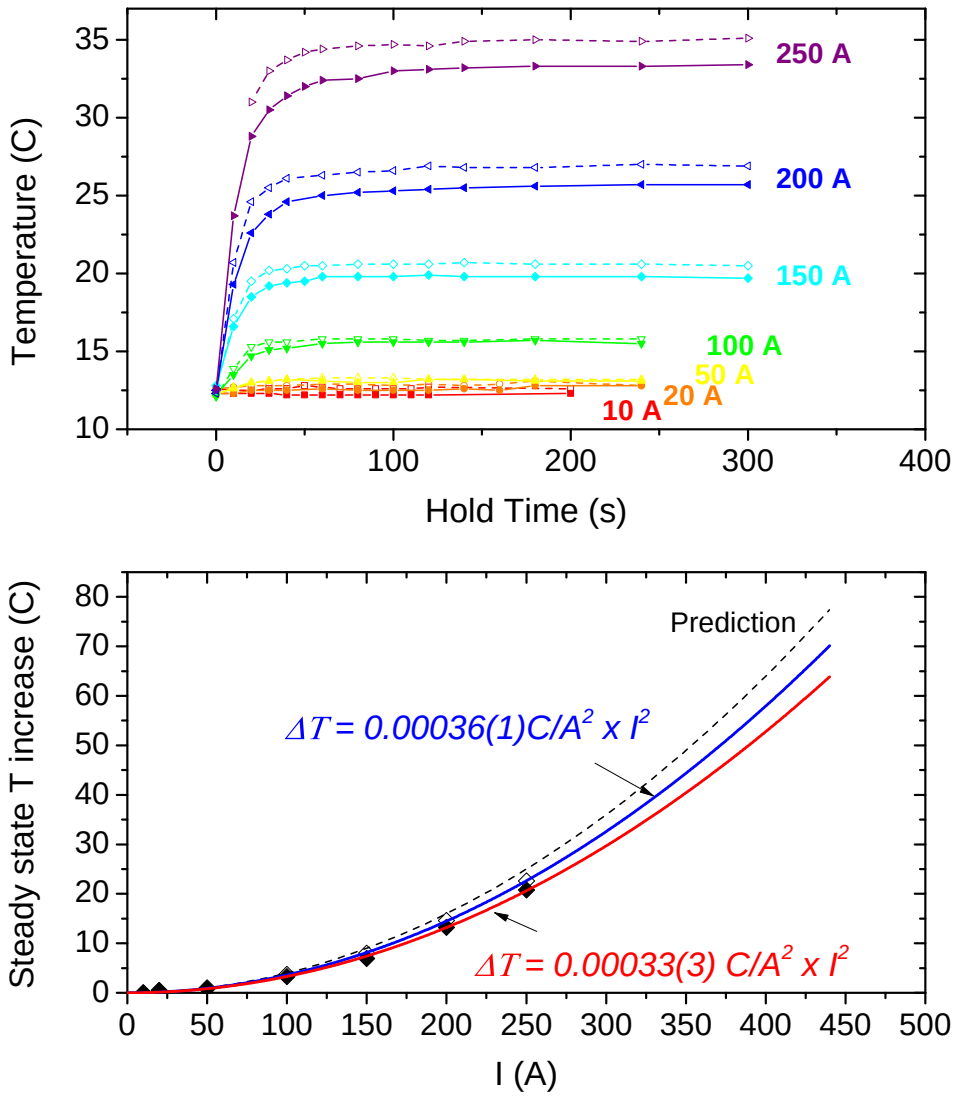

Figure 3.8: Top: Temperatures of the Bias coils vs. time for a variety of currents flowing through the Bias coil pair. A steady-state temperature is achieved after about 45 seconds, which is similar to duration of the magnetic trap stage of a typical experiment. Open symbols show one coil's temperature, closed symbols show the other. The temperature difference between the two coils could be caused by a small kink or burr that impedes the flow of cooling water, or it could simply be a calibration difference between the two sensors. Bottom: Steady-state Bias coil temperature vs. current follows the quadratic dependence predicted in Ty Cumby's thesis [36].

catastrophic overheating in previous systems within our group. A series of Sensata/Airpax 67L050 airfoil temperature sensors are attached to each coil and the high-current leads near each transistor. If any measured temperature rises above 50 C, then the safety interlock is triggered. We chose this cutoff because it is significantly higher than the normal operating temperatures – it is not clear that any damage would actually occur to the system at 50 degrees.

Chapter 4

Procedure: from room temperature to ultra cold

Our quantum gas machine has been in operation for more than a decade since it was originally constructed by Jon Goldwin [38]. The design incorporates popular techniques from experiments with Bose-Einstein condensates, including a vapor-cell Magneto-Optical Trap [39, 3, 40], sympathetic cooling in a magnetic trap [41, 42], and a far-detuned optical trap [43] that sets the stage for our measurements. The apparatus is constantly being updated, with changes catalogued in graduate student theses [44, 36]. For my part, updates to the apparatus include the magnet system from the previous Chapter as well as improved laser systems, microwave delivery, optical trapping, and imaging. For completeness and to define experimental parameters relevant to our data, I will describe these updates while reviewing our typical sequence for preparing and measuring a quantum gas.

To that end, Section 4.1 introduces the main characters: the Boson ^{87}Rb and the Fermion ^{40}K. These atoms are first collected from a dilute room-temperature vapor inside of a vacuum chamber and then cooled to a temperature of 1 microKelvin by the four-stage process that is described in Section 4.2. This ultracold gas is subsequently transferred into the focus of an intense infrared laser beam in Section 4.3. Within this optical trap, we further cool the atoms to a few hundred nanoKelvin. Experiments are performed on the atoms at a magnetic field near the interspecies Fano-Feshbach resonance at 547 G. Finally, the optical trap is snapped off and the atoms drift outwards into the vacuum. Resonant light illuminates the gas, which casts a shadow onto a CCD camera, which transfers the data to a computer for analysis (Section 4.4). Because the measurement

process scatters atoms to the outer reaches of the vacuum chamber, we create a new sample for every data point.

4.1 ^{40}K and ^{87}Rb atoms

^{40}K and ^{87}Rb are an all-star team in the world of quantum gases. ^{87}Rb atoms formed the first Bose-Einstein condensate [4] and ^{40}K was the first atomic degenerate Fermi gas [7]. In the ultra cold regime, the interactions between different ^{40}K atoms or between ^{40}K and ^{87}Rb atoms can be tuned by magnetic Fano-Feshbach resonances, which yields a rich phase diagram that includes interaction-driven BEC collapse and phase separation [45, 46]. More recently, ^{40}K-^{87}Rb interactions in optical lattices were used to shift the superfluid to Mott insulator quantum phase transition temperature in ^{87}Rb atoms [47]. ^{40}K-^{87}Rb Feshbach molecules were the also first ultra cold Fermionic molecules to be created in the lab [48]. This development led to the association of ultra cold ground-state polar ^{40}K-^{87}Rb molecules [20], which promise to bring controlled quantum chemistry and stable long-ranged interactions to the world of quantum gases.

Both ^{40}K and ^{87}Rb are Alkali metals, which means that they each have a single unpaired valence electron with an energy level structure similar to an oversized Hydrogen atom. Figure 4.1 outlines the states relevant to our work. The D2 lines for these atoms are located at 767 nm and 780 nm respectively. We use laser light that is resonant with these transitions to manipulate and measure each species. Figure 4.2 shows schematics of these laser systems for ^{40}K and ^{87}Rb. Beam shaping optics, wave plates, polarizers, optical isolators, shutters, and mirrors are omitted for clarity. The ^{40}K lasers are locked to the $F = 2 \rightarrow F'$ line in the ^{39}K saturated absorption spectrum, and the ^{87}Rb lasers are locked to the $F = 1$ to $F' = 1, 2$ crossover peak in the ^{87}Rb saturated absorption spectrum. Although the laser systems are drawn separately for each species, we combine the laser beams into a smaller number of paths before they hit the atoms: the K 'MOT' beam and Rb 'MOT trap' beam are coupled into the same optical fiber before they are used to trap and cool the atoms; the 'OP Zeeman' and 'OP Repump' beams for both species are combined into a single path used for optical pumping after the MOT stage; and the 'Low B' and 'High B' imaging

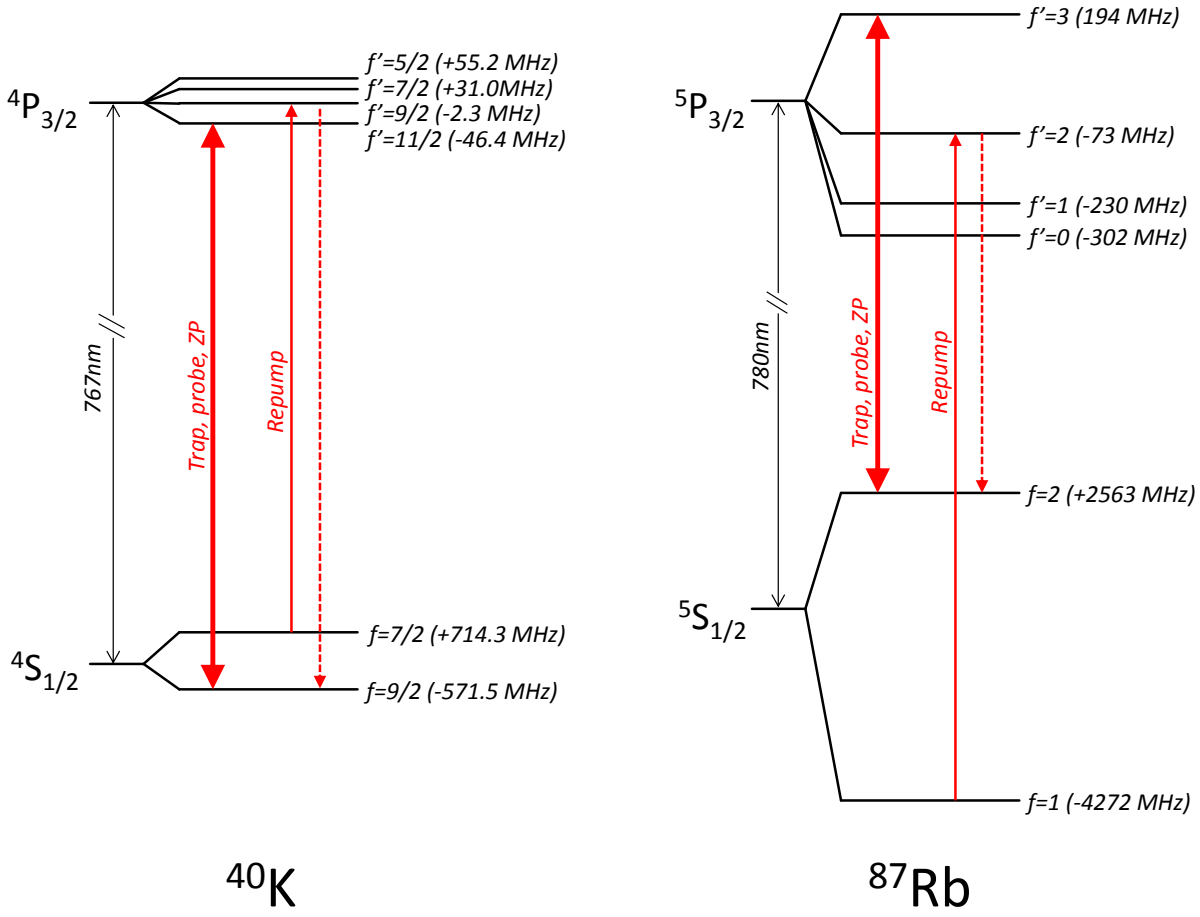

Figure 4.1: The D2 lines for ^{40}K (left) and ^{87}Rb (right). Thick vertical red arrows indicate the primary transitions that we use for trap, cool, optically pump, and image the atoms. The thin vertical red arrows show the repump transitions, and dashed lines show spontaneous decay paths to the other groundstate. Hyperfine splittings for both species are indicated at zero external magnetic field and are not to scale [49, 50]. ^{40}K has nuclear spin $I = 4$ and ^{87}Rb has $I = 3/2$.

beams for both species are also combined into a single imaging beam path. Before the beams are combined, we use shutters and Acousto-Optic (AO) modulators to independently switch different beams on and off.

Recent years have seen a few improvements to our lasers. The saturated absorption locks for both atoms' repump lasers now generate an error signal by modulating the laser phase at 10 MHz with electro-optic modulators, which provides more bandwidth and stability than the previous method of modulating the laser current at 300 kHz. We also replaced the ^{87}Rb repump laser, which was previously a commercial ECDL, with a DBR from Photodigm. The DBR puts out enough power that the Rb repump light can now be sent directly to the atoms in the MOT, which bypasses the tapered amplifier and shortens the optical path. New beam-shaping and polarization optics have also been employed to improve the imaging beams, which are described in more detail in Section 4.4.

As for the atoms themselves, the entire preparation and measurement of the quantum gas occurs in an ultra-high vacuum environment. The vacuum system contains two glass chambers, the (relatively) high-pressure collection cell and the lower-pressure science cell (see Figure 4.3). These two cells are separated by a long tube to maintain differential pressure between the two chambers. Each experiment begins with a dilute vapor of K and Rb atoms in the collection cell. Rb atoms are dispensed by a commercial getter source from SAES. K atoms come from a similar home-built dispenser [51]. Since the natural abundance of ^{40}K is only 0.012 percent, our K source uses enriched material that contains 5 percent ^{40}K [44]. Whereas the atom dispensers were originally pulsed every morning to fill the collection cell with alkali atoms, we now run them at a lower constant current to get more consistent day-to-day atom numbers.

4.2 Initial cooling stages

To transform the warm vapor into an ultra cold quantum gas, we subject the ^{40}K and ^{87}Rb to multiple stages of cooling. Although the apparatus can produce a quantum-degenerate mixture of a Bose-Einstein Condensate and a Degenerate Fermi Gas, the experiments in this thesis cut the

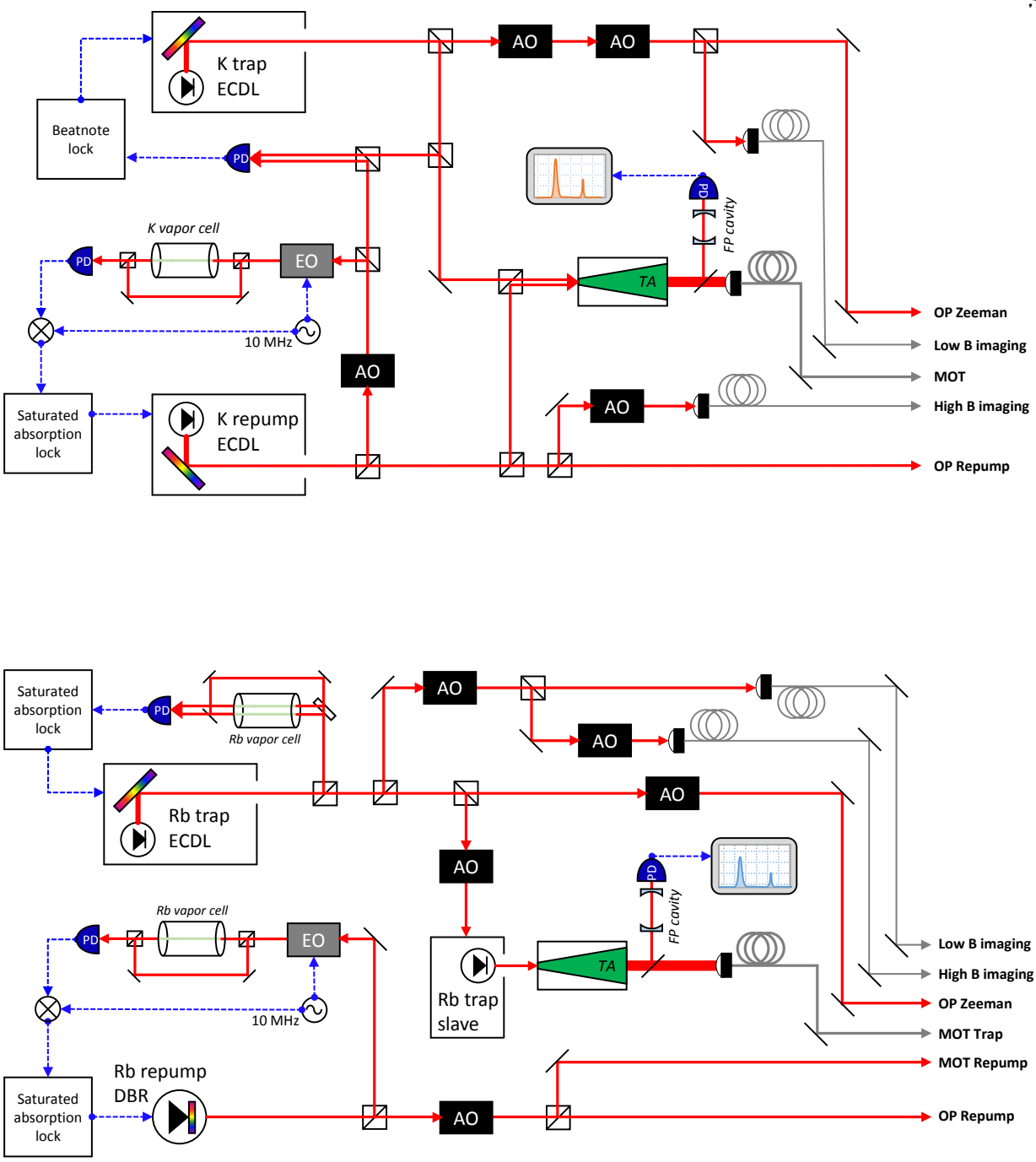

Figure 4.2: **Top:** Our ^{40}K laser system. Laser light is generated by a pair of Extended Cavity Diode Lasers (ECDLs) and amplified by a Tapered Amplifier (TA), the spectral output of which is monitored on a scanning Fabry-Perot (FP) cavity. To repump laser phase is dithered at 10 MHz by an Electro-Optic (EO) modulator before the beam passes through a K vapor cell. The transmitted light is measured on a photodiode (PD) and then demodulated to generate an error signal. **Bottom**: Our ^{87}Rb laser system is similar to the ^{40}K system except that the ^{87}Rb repump light is generated by a Distributed Bragg Reflector (DBR) laser diode, and then it is transmitted directly to the atoms without being amplified by a TA. Another difference is that the ^{87}Rb trap laser is locked to the Rb vapor cell by modulating the laser current directly at 300 kHz rather than using an EO to modulate the laser phase.

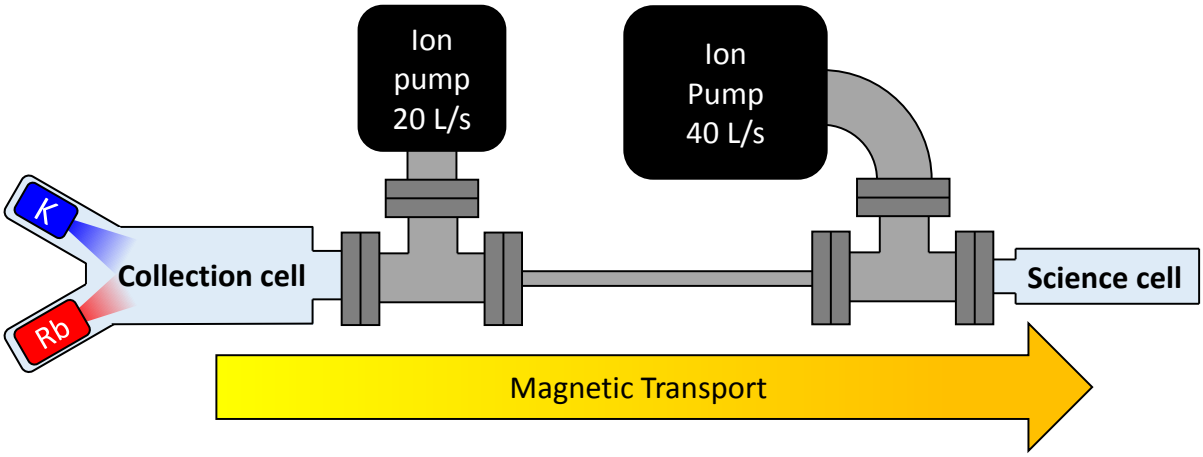

Figure 4.3: A cartoon of the vacuum system. A dilute vapor of K and Rb is dispensed into the collection cell (left) where the atomic sample is formed at the beginning of an experiment. The sample is then transferred through a narrow differential pumping tube into the science cell where experiments take place (right).

evaporative cooling short just before the onset of quantum degeneracy. This maximizes the spatial and momentum overlap between the ^{40}K and ^{87}Rb clouds and simplifies our analysis of data on the interactions between the two species. A huge variety of experiments are possible once the quantum gas mixture is prepared. The preparation and cooling of the gas is a repeatable sequence that is more or less the same for every data point.

The ^{40}K and ^{87}Rb atoms are initially captured by a three dimensional dual-species vapor-cell MOT in the vacuum chamber's collection cell. Next, we spatially compress the ^{87}Rb MOT by reducing the repump power and detuning the trap light to reduce the photon scattering rate. At the same time, we jump the ^{40}K trap light towards resonance for improved Doppler cooling. Next, we zero the magnetic field using several shim coils and the ^{87}Rb atoms are further cooled by polarization gradient cooling. A quantization field is then applied along with a pulse of circularly polarized optical pumping light (the 'OP Zeeman' and 'OP Repump' beams in Figure 4.2) to bring ^{40}K and ^{87}Rb into the low-field-seeking $|f, m_f\rangle = |9/2, 9/2\rangle$ and $|2, 2\rangle$ states respectively. At this point, we load the atoms into a quadrupole magnetic trap (Qtrap), which is generated by a pair of high-current electromagnet coils. The Qtrap coils are mechanically translated 81 cm to the other end of the vacuum chamber to deliver the atoms to the science cell. At this point, we typically have a few million ^{40}K atoms and a few times 10^8 ^{87}Rb atoms at a temperature near 400 microKelvin.

Once the atoms are in the science cell, we briefly reduce the quadrupole field so that any residual ^{87}Rb atoms in the $|2, 1\rangle$ state fall out of the trap. Next, we load the purified gas into the Ioffe-Pritchard (IP) magnetic trap that was described in Chapter 3, and the Qtrap coils return to their home at the collection cell on the other end of the chamber. This trap is approximately harmonic in all three directions, with trap frequencies $\omega_x = \omega_y = 125$ Hz and $\omega_z = 18$ Hz. The atoms are trapped at the minimum of the magnetic field. In the IP trap, we cool the gas by forced evaporation on the ^{87}Rb atoms, which sympathetically cools the ^{40}K atoms through elastic collisions between the two atom species [38, 42]. We apply an RF field, which is resonant with $|f, m_f\rangle = |2, 2\rangle \rightarrow |2, 1\rangle$ and $|2, 1\rangle \rightarrow |2, 0\rangle$ transitions at the edge of the atom cloud, to remove the "hot" ^{87}Rb atoms. The $|2, 0\rangle$ atoms have no magnetic moment and so they fall out of the magnetic

trap. The atom cloud shrinks as it cools and we sweep the RF frequency downwards to remove atoms closer and closer to the center of the magnetic potential. After evaporation in the magnetic trap we typically have about one million ^{40}K atoms and two million ^{87}Rb atoms at a temperature near 1 microKelvin.

4.3 The optically trapped mixture

After an ultra cold mixture is produced in the magnetic IP trap, we transfer the atoms into a far-detuned Optical Trap (OT) formed by light from a 10 W multimode fiber laser with a wavelength of 1090 nm. This wavelength is red-detuned from the strong D1 and D2 lines, so that the ^{40}K and ^{87}Rb atoms both feel an attractive potential that is proportional to the intensity of the light. The OT potential is independent of hyperfine or Zeeman states, which opens the possibility of experiments with different spin mixtures. This trap also enables access to tunable interactions near Fano-Feshbach resonances at high magnetic fields, which are the crucial to the work in Chapters 5, 6, 7, and 8.

Following Grimm *et al.* [43], the potential U for OT light with intensity I is given by

$$U = -\frac{3\pi c^2 \Gamma}{2\omega_0^3}\left(\frac{1}{\omega_0 - \omega} + \frac{1}{\omega_0 + \omega}\right) I \tag{4.1}$$

where Γ is the transition line width, c is the speed of light, ω_0 is the resonant frequency, and $\omega = \frac{2\pi c}{1090\text{ nm}}$ is the frequency of the light. In the limit of large detuning, the D1 and D2 lines in alkali atoms can be combined into a single effective 'D' line whose resonant frequency is the average of the frequencies for the D1 and D2 lines. Using parameters from [49], the ^{87}Rb D transition has $\omega_0 = \frac{2\pi c}{787.6\text{ nm}}$ and $\Gamma = 2\pi \times 5.9$ MHz. Similarly, the ^{40}K transition has $\omega_0 = \frac{2\pi c}{768.4\text{ nm}}$ and $\Gamma = 2\pi \times 6.0$ MHz [50]. Plugging these numbers into Eq. 4.1, we can see that the ratio of the optical potentials is $U_{\mathrm{K}}/U_{\mathrm{Rb}} = 0.88$. In practice, gravity pulls the atoms down away from the OT center. The heavier ^{87}Rb atoms sag further and so they sit in a slightly different part of the beam intensity profile.

Figure 4.4 shows the geometry for an experiment in the optical trap. The horizontal OT

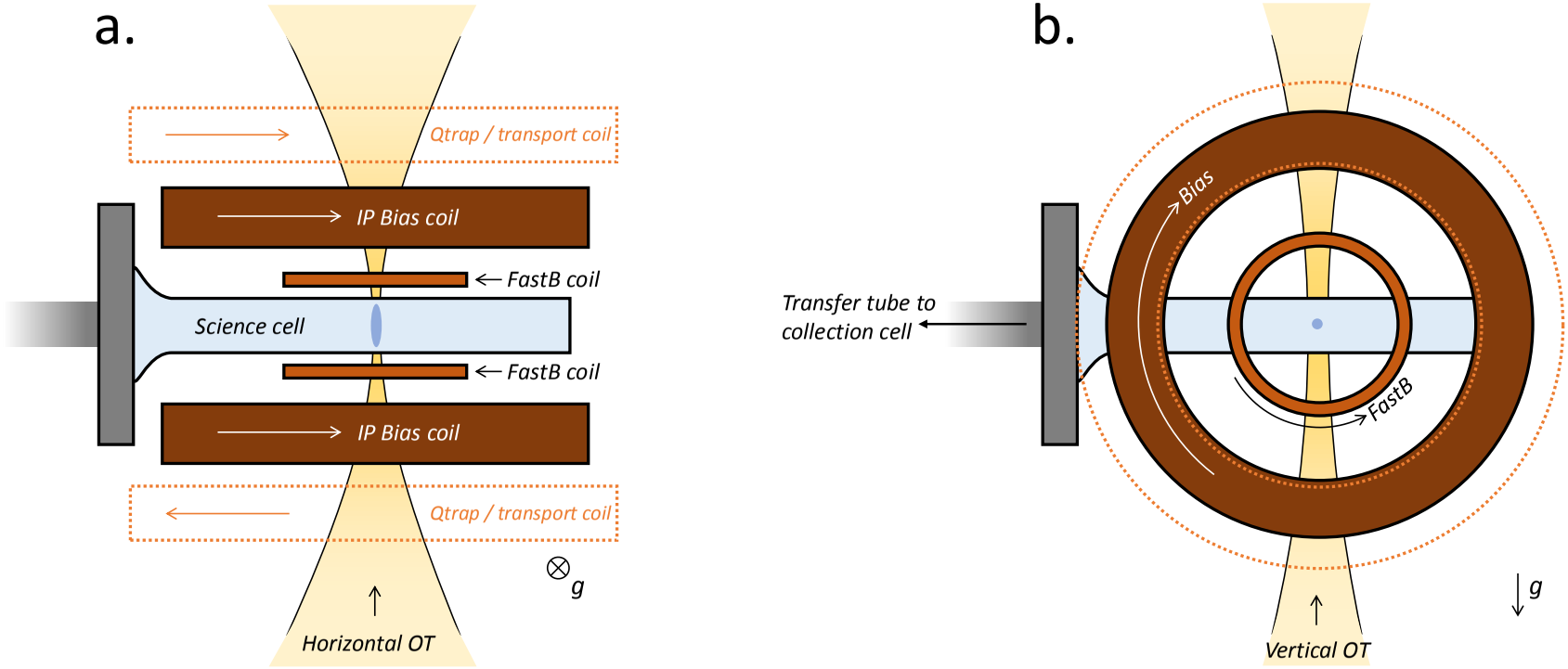

Figure 4.4: The arrangement of the optical traps, glass science cell, and magnetic bias coils used for an experiment at high magnetic fields (not to scale). The arrows on magnetic field coils show the direction of electric current, and the arrows on laser beams show the direction of propagation. Subfigure (a) shows the top view and subfigure (b) shows a side view. The vertical OT beam shown in (b) is only turned on for some experiments. The Qtrap magnetic transfer coils (dashed lines) are only present during the transfer into the IP trap. During experiments at high fields, the transfer coils rest near the collection cell at the other end of the vacuum chamber.

beam has a $1/e^2$ radius of 19 μm. Alone, it forms an elongated trap with an aspect ratio of 100 that is used in the majority of experiments. The vertical OT beam has a $1/e^2$ radius of 200 μm. The trap formed by the combination of horizontal and vertical beams has an aspect ratio of about 20, which is useful if a spatially compressed cloud is desired. The Bias magnetic field is oriented along the axis of the horizontal optical trap beam. This field is actually the sum of two Helmholtz pairs: the strong Bias coils (which are also part of the IP trap) and the lower-inductance FastB coils.

The ^{40}K and ^{87}Rb atoms are initially loaded into the optical trap in the low-field-seeking $|9/2, 9/2\rangle$ and $|2, 2\rangle$ states. To prepare the atoms for experiments near the interspecies Fano-Feshbach resonance, we transfer the to the high-field-seeking $|9/2, -9/2\rangle$ and $|1, 1\rangle$ states. During these transfers, the Bias coils provide a quantization axis with a 28 G magnetic field. For the ^{40}K atoms, an RF pulse with a linear chirp from 9.7 MHz to 8.0 MHz drives an Adiabatic Rapid Passage (ARP) across the $m_f = 9/2 \rightarrow 7/2 \rightarrow 5/2 \rightarrow 3/2 \rightarrow 1/2 \rightarrow -1/2 \rightarrow -3/2 \rightarrow -5/2 \rightarrow -7/2 \rightarrow -9/2$ states [52]. The ^{40}K atoms are transferred into the $|9/2, -9/2\rangle$ state with about 90 percent efficiency. For the ^{87}Rb atoms, a microwave pulse with a linear chirp between 6.893 GHz and 6.896 GHz drives an ARP from $|2, 2\rangle$ to $|1, 1\rangle$ with about 98 percent efficiency.

With the installation of the new electromagnet system (Chapter 3), the radio and microwave antennae which were attached to the old magnet system needed to be replaced. Of these, the ^{87}Rb microwave antenna was the most challenging since it needed to have dual resonant frequencies at 6.9 GHz and 8.0 GHz. These frequencies of interest are resonant with the $|2, 2\rangle \rightarrow |1, 1\rangle$ transition at magnetic fields of 28 G and 545 G respectively. Figure 4.5 shows the antenna at an early stage of construction and its final measured reflection coefficient. The antenna, which was designed by Carl Sauer in the electronics shop, consists of copper traces on both sides of a thin phenolic substrate. It is mounted between the magnetic bias coils near the science cell, about 6 mm above the position of the atoms. The emitted microwave radiation is centered on the circular aperture, which is aligned above the atoms. Two small pieces of copper tape (not shown) are soldered to the long straight section of the lead on the top side. We adjusted their positions and orientations to stub tune the

resonant frequencies.

Once the atoms are prepared in their high-field seeking states in the optical trap, the Bias coils ramp the field up to 550 G. The power in the horizontal OT beam is gradually lowered so that the most energetic atoms fall out and the sample is evaporatively cooled. Next, we ramp the OT power back up by a factor of two or so to ensure that the atoms are confined in the harmonic region at the center of the trap. At this point, the quantum gas is fully prepared for the sorts of experiments that are described in the next four Chapters. Most of these take the form of DC magnetic field sequences to manipulate atomic interactions, radio / microwave pulses to control and measure the atoms' states, or deformations of the optical potential, which help us to learn about the scattering properties of the atoms under different conditions.

4.4 Imaging

All of the data in this thesis comes from pictures of quantum gas mixtures. From these images we extract the number (N), temperature (T), and density (n) of each atom species selectively. We track the evolution of these quantities to extract the scattering rates in Chapter 8. In the next Chapter, we apply these techniques to image ^{40}K^{87}Rb Feshbach molecules. They are also used to diagnose and optimize the preparation or manipulation of the atoms. For any of these applications, we initiate the imaging sequence by quickly snapping the optical trap off. After the clouds have expanded into the chamber for a few milliseconds, we perform destructive absorption imaging with pulses of resonant light [53]. This method measures the optical depth of a shadow cast by the atoms, which is imaged using the optics depicted in Figure 4.6.

The resulting pictures reveal the 2D column density profile $n(x, y)$ in the strong radial y direction and weak axial x direction of the optical trap. We fit these to a Gaussian surface:

$$n(x, y) = \frac{N}{2\pi\sigma_x\sigma_y} e^{-\frac{x^2}{2\sigma_x^2} - \frac{y^2}{2\sigma_y^2}}. \tag{4.2}$$

Based on the cylindrical symmetry of the trap, we assume that the shape of the density distribution along the imaging axis is the same as it is in the measured radial y direction. Formula 4.2 is valid

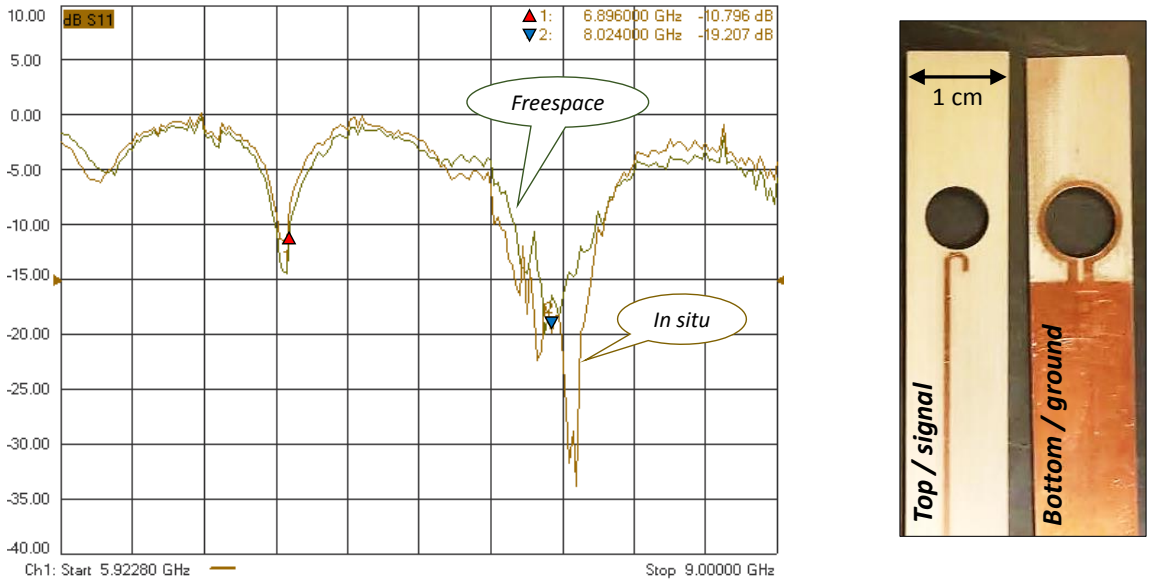

Figure 4.5: A dual-resonant antenna for ^{87}Rb. Left: the magnitude of the power reflection coefficient S11 as measured by a network analyzer. A lower reflection coefficient presumably implies more efficient transmission of radiation to the atoms, since there are no dissipative elements in the system. Right: Photographs of the top and bottom sides of antennae before stub tuning. An edge-mounted SMA jack is soldered to the lower end of the antenna (as oriented in the picture). The center SMA pin is connected to the copper trace on the top side and the ground pins are soldered to the ground plane on the bottom side.

for a harmonically confined thermal gas in the Maxwell-Boltzmann limit. For an ideal gas in this limit, the in-trap RMS cloud sizes are given by $\sigma_{x,0}^2 = \frac{k_B T}{m\omega_x^2}$ and $\sigma_{y,0}^2 = \frac{k_B T}{m\omega_y^2}$ where k_B is the Boltzmann constant and the trap frequencies are defined such that the trap potential has the form $U = \frac{1}{2}m\omega_x^2 x^2 + \frac{1}{2}m\omega_y^2 y^2 + \frac{1}{2}m\omega_z^2 z^2$. When the trap is switched off at time $t = 0$, a thermal noninteracting gas will undergo ballistic expansion such that

$$\sigma(t) = \sqrt{\sigma_0^2 + \frac{k_B T}{m} t^2}. \tag{4.3}$$

in each direction. We use this formula to extract the temperature from the measured sizes of the expanded clouds. In some of our data the ^{40}K gas is quantum degenerate, with T/T_F as low as 0.2. For this degeneracy, a Gaussian fit to the density profile can measure the number of atoms but not its temperature [54]. Since the Fermi gas is in thermal equilibrium with a ^{87}Rb Bose gas that still follows a Maxwell-Boltzmann distribution, we use the ^{87}Rb cloud size as a measurement of temperature for both atom species in these situations. For $T/T_F > 0.6$, we find that the temperatures measured from the expanded ^{87}Rb and ^{40}K clouds agree with each other.

For all data points, we image the ^{87}Rb atoms with light tuned to the cycling $f = 2 \rightarrow f' = 3$ transition, and we image the ^{40}K with light tuned to the cycling $f = 9/2 \rightarrow f' = 11/2$ transition. However, there are a few differences in the imaging procedure depending on the specific experiment. For diagnostic images of early experiment stages, the magnetic-field quantization axis is provided by an auxiliary coil that points along the imaging axis. In this case, the probe light is circularly polarized. For imaging the atoms at high magnetic fields, the Bias field sets the quantization axis, and is perpendicular to the imaging axis. The probe light in this case is linearly polarized and the atoms' measured OD is consequently reduced by a factor of two. Furthermore, experiments at low magnetic fields are insensitive to the Zeeman state whereas high field imaging selectively images ^{40}K atoms in the $|9/2, -9/2\rangle$ state and ^{87}Rb atoms in the $|2, 2\rangle$ state. Finally, since high-field experiments are performed on ^{87}Rb atoms in the $|1, 1\rangle$ state, a microwave ARP transfers ^{87}Rb atoms into the $|2, 2\rangle$ state immediately before imaging.

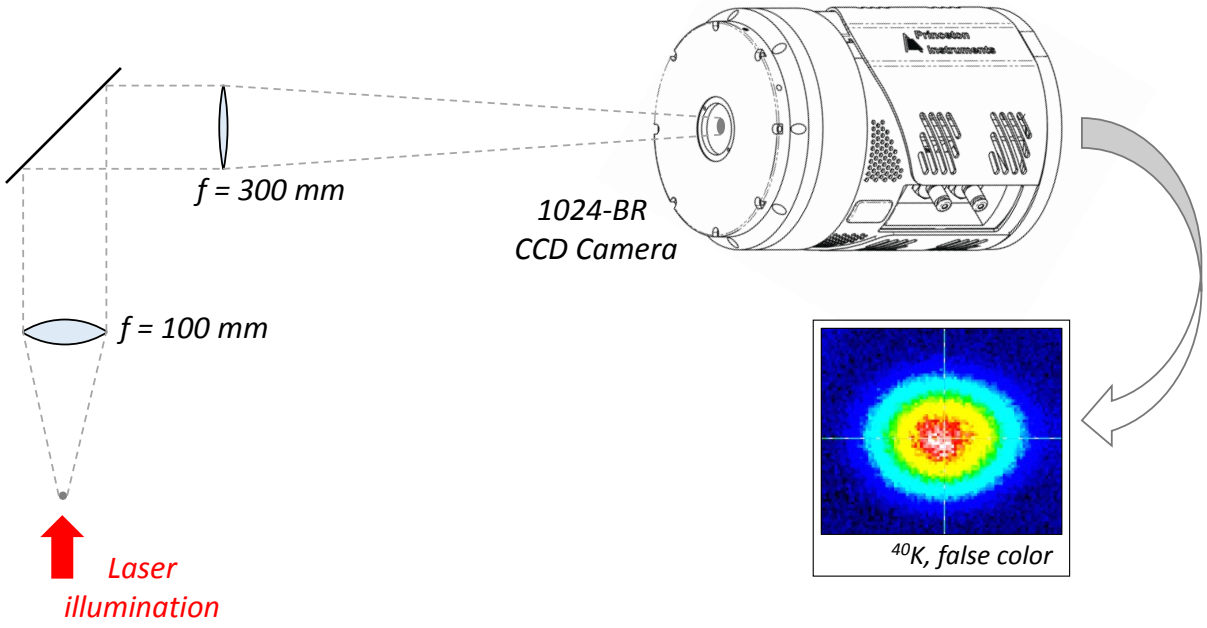

Figure 4.6: A cartoon of the low-magnification imaging system. Resonant laser light propagates along the magnetic transport axis of the vacuum system. The atoms' shadow is imaged on a CCD camera with a magnification of three. A sample OD image of ^{40}K atoms is shown with false color indicating the optical depth.

Chapter 5

Efficient magnetoassociation of KRb Feshbach molecules

Magnetic Fano-Feshbach resonances can be used to convert an ultra cold gas of atoms into an ultra cold gas of molecules. These weakly bound Feshbach molecules act as a starting point for experiments from superfluidity to quantum chemistry, and so the physics of how these pairs form has been an active topic of research [19, 18]. Previous work has mostly focused on bosonic Feshbach molecules formed out of two fermionic or two bosonic atoms, whereas less is known about the association of fermionic Feshbach molecules from one Boson and one Fermion. This Chapter presents our detailed measurements of fermionic ^{40}K^{87}Rb in the atomic gas mixture of ^{40}K and ^{87}Rb. Section 5.1 describes how Feshbach molecules are created when a magnetic field sweeps through the Fano-Feshbach resonance. Section 5.2 reviews our tools for detecting and imaging the molecules. In Section 5.3, a quantitative model based on the Landau-Zener paradigm accurately predicts the rates of molecule formation in the limit of small molecule numbers. When the atomic sample is substantially depleted, molecule production saturates. Section 5.4 shows how the maximum number of ^{40}K^{87}Rb molecules falls short of a theoretical prediction for experiments that begin with a degenerate Fermi gas of ^{40}K atoms.

The bulk of the material in this Chapter is published in Reference [55]. In particular, Sections 5.3 and 5.4 are published nearly verbatim in that work. Sections 5.1 and 5.2 also contain material from the paper, but they are expanded to include more detail and background information.

5.1 How magnetoassociation works

One way to make Feshbach molecules in an atomic gas is to sweep the magnetic field across a Fano-Feshbach resonance. This process, called magnetoassociation, has proven to be one of the most robust methods of Feshbach molecule formation and is effective for both wide and narrow Fano-Feshbach resonances as well as for gases of fermionic atoms, bosonic atoms, or mixtures of two atomic species [19, 18]. Figure 5.1 illustrates the two-body energy spectrum for Feshbach molecules in a gas of ^{40}K and ^{87}Rb atoms. In the limit where the atoms' kinetic energy is much greater than the harmonic oscillator level spacing in the trap, there is a continuum of free-particle states on both sides of the Fano-Feshbach resonance. The two-body Feshbach molecule state has zero binding energy at the resonance, and increasing binding energy as the field is lowered. For these experiments, we use the broadest ^{40}K–^{87}Rb Fano-Feshbach resonance at $B_0 = 546.618$ G.

To transfer free atoms into the Feshbach molecule state, we ramp the magnetic field downwards from 550 G through the resonance to 545.7 G, which is from right to left in Figure 5.1. The ramp rate $\dot{B}$ is key to the magnetoassociation process as shown in Figure 5.2. Let f be defined as the number of molecules divided by the lesser of the initial numbers of atoms of ^{40}K and ^{87}Rb, $N_<$. If $\dot{B}$ is fast compared to the timescales of two-body adiabaticity, then f is small. In this fast sweep limit, molecule association is essentially the independent sum of many two-body pairing processes between nearby atoms. Section 5.3 characterizes this regime. As the field sweeps get slower and more adiabatic, f increases and saturates. Notice that f saturates well below unity, which is explored in Section 5.4. In order to extract information about the fast-sweep and saturated regimes independently, we fit the molecule conversion efficiency as a function of the magnetic-sweep rate $|\dot{B}|$ to the following formula:

$$f = f_0 \left(1 - e^{-\Gamma/(f_0|\dot{B}|)}\right). \tag{5.1}$$

Here, f_0 is the saturated molecule conversion fraction and $f = \Gamma/|\dot{B}|$ in the fast-sweep limit. Before moving on to the measurements of these quantities, I will first describe how we detect and image the Feshbach molecules.

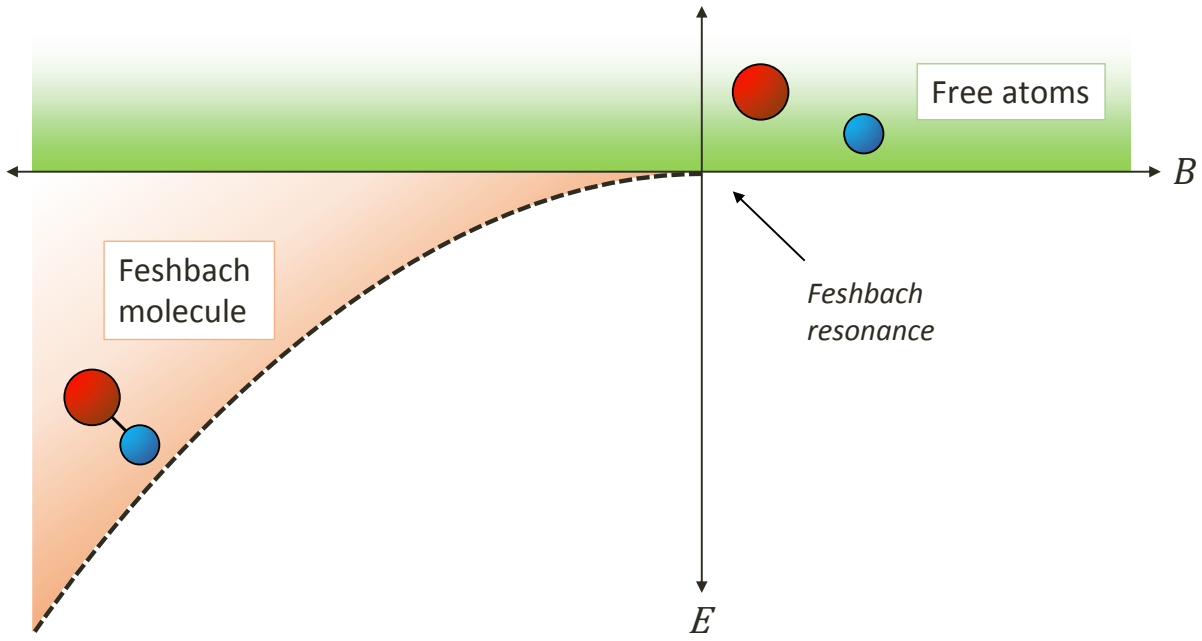

Figure 5.1: Schematic two-body energy diagram for ^{40}K and ^{87}Rb as a function of magnetic field near an interspecies Fano-Feshbach resonance. Zero on the vertical axis represents the threshold for a continuum of free two-body states. The Feshbach molecule state (dashed line) exists at fields below the Fano-Feshbach resonance. In magnetoassociation, we sweep the field from right to left on these axes.

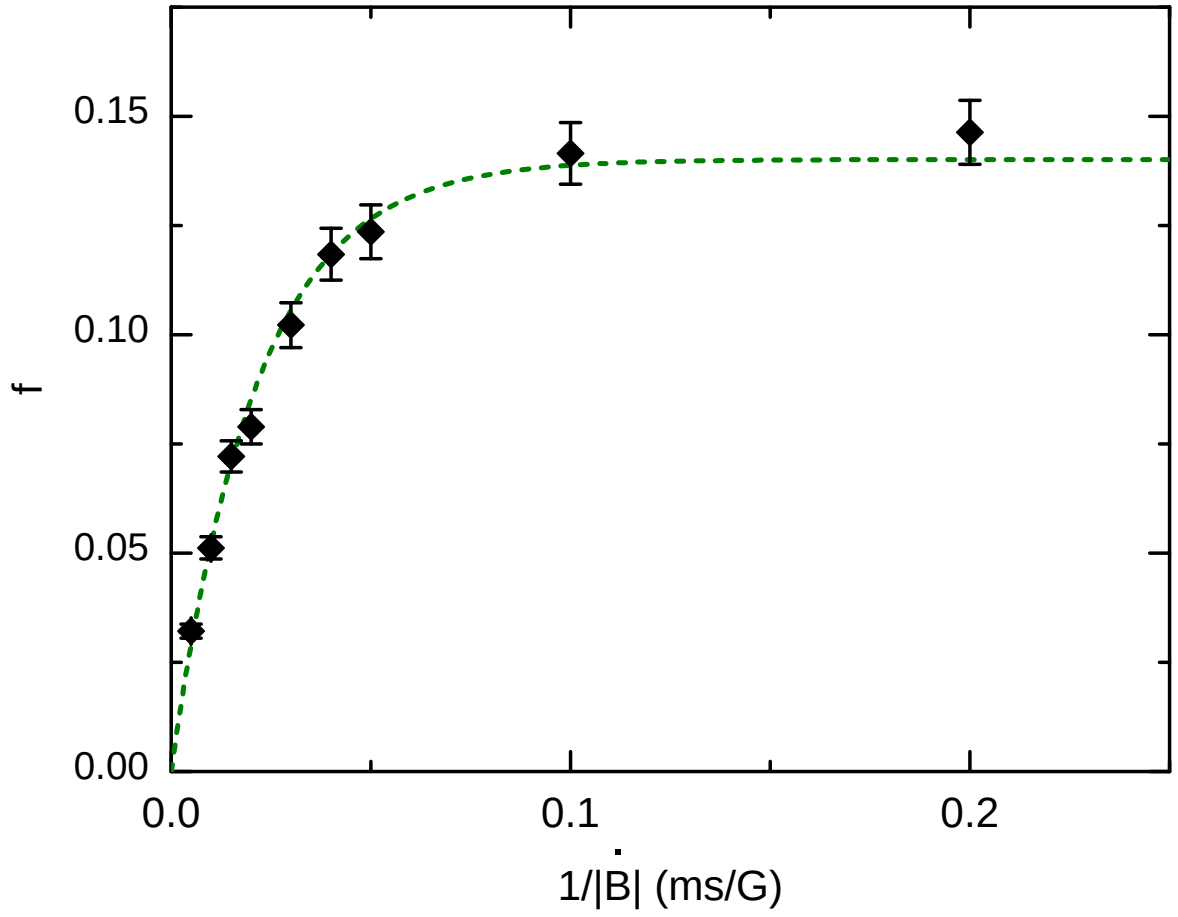

Figure 5.2: The fraction of the minority atom species converted to molecules, f, vs the inverse magnetic-sweep rate, $1/|\dot{B}|$, across the Fano-Feshbach resonance. The dashed line shows a fit to Eq. (5.1), which gives $\Gamma = 6.5(5)$ G/ms and $f_0 = 14(2)\%$, or $3.8(5) \times 10^4$ molecules, for this data. The initial gas consisted of 2.6×10^5 ^{40}K atoms and 3.4×10^5 ^{87}Rb atoms at T= 490 nK. This data was published in Reference [55].

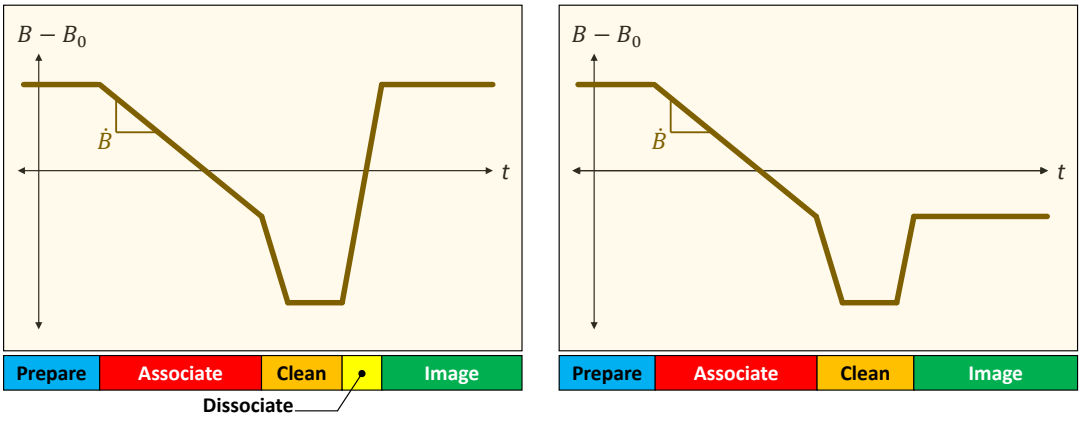

Figure 5.3: Schematic timing sequences for creating and imaging molecules. The colored bars along the bottom label the various stages of the sequence. Left: Imaging dissociated molecules. Right: Direct molecule imaging.

5.2 Counting the molecules

Much like atoms, ^{40}K^{87}Rb Feshbach molecules are probed by resonant absorption imaging after a brief expansion from the optical dipole trap. Figure 5.3 describes two different methods to make the molecules visible on the atomic transitions. In both cases, we prepare the atoms at a field of 549.9 G, which is above the 546.62 G interspecies Fano-Feshbach resonance. We sweep the magnetic field down through the resonance to 545.7 G to form molecules. A typical speed for this adiabatic magnetoassociation is 3 G/ms. To clean out the unpaired ^{40}K atoms, we ramp the field in 50 μs down to 544.7 G and then transfer unpaired ^{40}K atoms from the $|9/2, -9/2\rangle$ state to the $|9/2, -7/2\rangle$ state using RF Adiabatic Rapid Passage (ARP). The binding energy of the molecules here is $h\times$3 MHz [33] and the ARP for atoms does not affect the molecules. The atoms become invisible to probe light once they are in the $|9/2, -7/2\rangle$ state.

At this point, we have two options. The most straightforward of these is to ramp the field back through the Fano-Feshbach resonance to dissociate the molecules. Since all unpaired ^{40}K atoms were rendered invisible by the ARP, the usual imaging of ^{40}K atoms only counts the atoms that were previously part of molecules. Unfortunately, images of dissociated molecules are potentially prone

to systematic errors from heating as the field is ramped back through the strong interactions at the resonance. An alternative strategy, which was employed for the data discussed in the remainder of this Chapter, is to image the molecules directly. By ramping the magnetic field back up to 546.0 G, we reduce the binding energy of the molecules so that they become resonant with the ^{40}K imaging transition. The molecule number measured with this technique is 85±5% of the number measured after dissociating the molecules and imaging the resulting atoms. Therefore, when imaging the molecules below the Fano-Feshbach resonance, a multiplicative factor is applied to correct the number for this measurement inefficiency.

To minimize the loss of molecules due to inelastic collisions, we can release the gas from the optical trap immediately after the molecules are formed. The sudden turn-off of the optical trap initiates an expansion of the gas that rapidly lowers the densities and switches off inelastic collisions. Figure 5.4 shows the measured molecule number and kinetic energy as a function of the time that the optical trap is turned off, t_{release}. Here, $t_{\mathrm{release}} = 0$ is defined as the time when the magnetic field crosses the Fano-Feshbach resonance. For $t_{\mathrm{release}} > 0$ we observe a heating and decrease in the molecule number with increasing t_{release}. We attribute this to inelastic collisions as the molecules spend more time in a relatively high density atom-molecule gas mixture in the trap. For $t_{\mathrm{release}} < 0$, the magnetic field crosses the Fano-Feshbach resonance after the gas starts expanding. For short expansion times, where $-0.3 < t_{\mathrm{release}} < 0$, the measured number and energy of the molecules is constant within the measurement uncertainty. For longer expansion times, corresponding to $t_{\mathrm{release}} < -0.3$, the rapidly dropping atom gas density reduces the efficiency of magnetoassociation according to the model in Section 5.3. Thus, we find that $t_{\mathrm{release}} = 0$ gives the most accurate measurement of the number and temperature of molecules that are created. While this Chapter focuses on the number of molecules created, the kinetic energy of the molecules will be the topic of Section 6.3 in the next Chapter.

Another issue with quantifying the molecule formation process is that inelastic collisions can cause loss and heating of the atoms even before molecules are formed. In particular, three-body recombination is an inelastic collision process for three atoms that produces a molecule plus an atom,

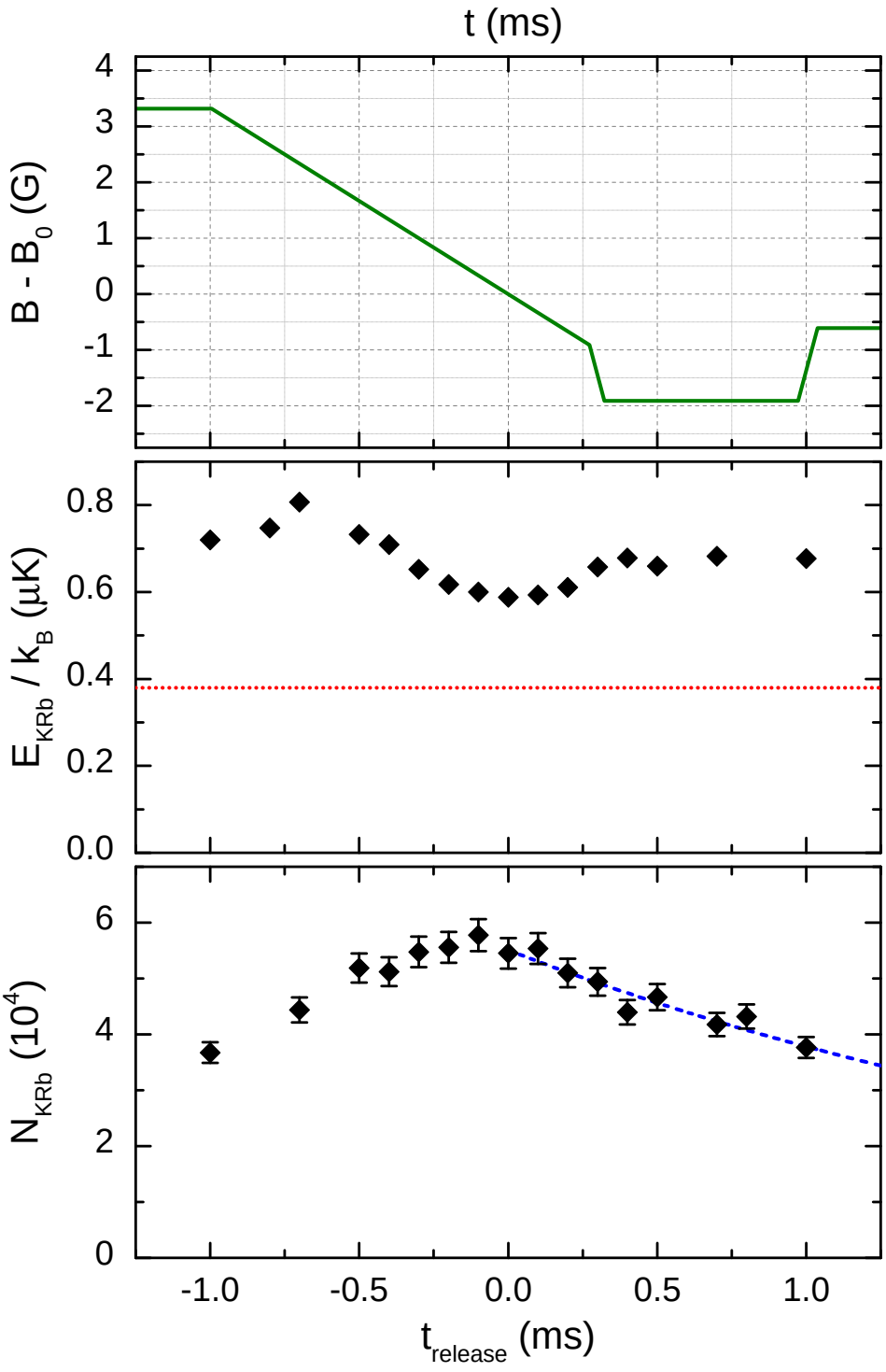

Figure 5.4: Top: A typical magnetic-field sweep sequence for molecule association. Here, $t = 0$ is defined as the time when B crosses the Fano-Feshbach resonance. Middle: measured molecule kinetic energy, from the RMS cloud size after time-of-flight expansion between 2.5 ms and 3.5 ms, vs the time, t_{release}, at which the optical trap is suddenly turned off to release the gas. The red dotted line shows the initial atom temperature, $T = 380$ μK. Bottom: Measured molecule number vs t_{release}. For comparison, the dashed line shows an exponential decay with a time constant of 2.7 ms. This data was published in Reference [55].

both with excess kinetic energy. The rate for three-body recombination increases dramatically near the Fano-Feshbach resonance, which I will explore in much more detail in Chapters 7 and 8. For a Bose–Fermi mixture, the dominant three-body recombination process removes two bosons and one fermion from the trap. Characterizing the initial atom conditions by the peak ^{87}Rb density squared times the peak ^{40}K density, we estimate the fractional atom loss to be below 10 percent as long as this density product remains lower than $2\times(10^{13}\ \mathrm{cm}^{-3})^3$. To isolate our measurements from inelastic loss, the initial atom conditions for data in Sections 5.3 and 5.4 are chosen to satisfy this condition. However, it is worth noting that our largest molecule clouds are produced from higher atom densities even though inelastic loss complicates the formation process. For example, 7×10^4 ^{40}K^{87}Rb molecules were measured in a mixture whose density product $n_{\mathrm{Rb}}^2 n_{\mathrm{K}}$ was initially $3\times(10^{13}\ \mathrm{cm}^{-3})^3$. The atom gas in this case was prepared at 560 nK, with 6.5×10^5 ^{40}K atoms at $T/T_{\mathrm{F}} = 0.51$ and 2.1×10^5 ^{87}Rb atoms at $T/T_{\mathrm{c}} = 2.0$.

5.3 Dependence on the magnetic-field sweep rate

This section focuses on the fast-sweep regime of molecule creation, where a simple extension of a two-body picture predicts that the molecule number increases linearly with the sweep duration [56, 19]. Here, the molecule number follows a Landau–Zener-like behavior [57, 19] with the transition probability into the molecular state given by $P = 1 - e^{-2\pi\delta_{\mathrm{LZ}}} \approx 2\pi\delta_{\mathrm{LZ}}$. For two particles in a box with volume $\mathcal{V}$, the Landau–Zener parameter δ_{LZ} depends on the Fano-Feshbach resonance parameters and is given by [56]

$$\delta_{\mathrm{LZ}} = \frac{1}{\mathcal{V}}\frac{2\pi\hbar}{\mu}\left|\frac{a_{\mathrm{bg}}\Delta}{\dot{B}}\right| \tag{5.2}$$

where $\hbar = h/2\pi$ and μ is the two-body reduced mass. Interestingly, this result applies for thermal atoms (fermions or bosons) as well as for atoms in the motional ground-state, such as atoms in a Bose–Einstein condensate or optical lattice [56]. Using classical probability theory, Eq. (5.2) can be generalized to multiple particles simply by multiplying P by the total number of available atom pairs to get the number of molecules [56]. Using a local density approximation, the molecule density

at position $\mathbf{r}$ is then given by

$$n_{\mathrm{mol}}(\mathbf{r}) = n_1(\mathbf{r}) n_2(\mathbf{r}) 2\pi \frac{2\pi\hbar}{\mu} \left| \frac{a_{\mathrm{bg}}\Delta}{\dot{B}} \right|. \tag{5.3}$$

Integrating Eq. (5.3) over the trapped atom gas distribution, and dividing by $N_<$, gives

$$f \approx \langle n_> \rangle 2\pi \frac{2\pi\hbar}{\mu} \left| \frac{a_{\mathrm{bg}}\Delta}{\dot{B}} \right| = \frac{\Gamma}{|\dot{B}|} \tag{5.4}$$

where $\langle n_> \rangle = \frac{1}{N_<} \int n_1(\mathbf{r}) n_2(\mathbf{r}) \mathrm{d}^3 r$ describes the density overlap of the two atom clouds.

Plugging the relevant Fano-Feshbach resonance parameters into Eq. (5.3) yields

$$\Gamma / \langle n_> \rangle = (2.8 \pm 0.1) \times 10^{-12} \text{ cm}^3 \text{ G/ms}. \tag{5.5}$$

This prediction for Γ, which is shown as a solid line in Fig. 5.5, agrees well with our measurements of Γ as a function of the density overlap of the initial atom gas, $\langle n_> \rangle$. From this it seems reasonable to conclude that magnetoassociation in the perturbative regime of fast magnetic-field sweeps behaves as expected in our Bose–Fermi mixture. Systematic errors in the measured atom number or molecule number would also change the measured value of Γ. The agreement between data and model in Figure 5.5 suggests that our imaging process accurately counts the number of molecules. To accomplish this agreement, it is crucial for the model to include a maximum molecule fraction f_0 which is below unity. In the next section we turn our attention to this saturation, which is important for experiments where one would like to create larger numbers of fermionic Feshbach molecules.

5.4 Saturated molecule number

Feshbach molecule conversion efficiencies as high as 90 percent have been observed in homonuclear Fermi gases [58]. In these experiments, it was found that the adiabatic molecule fraction f_0 is determined by the phase-space density in the parent gas of atoms [58]. Monte-Carlo simulations that select atom pairs within a phase-space distance criterion γ accurately predict f_0 over a broad range of initial gas conditions. The phenomenological criterion γ was determined by a fit to the

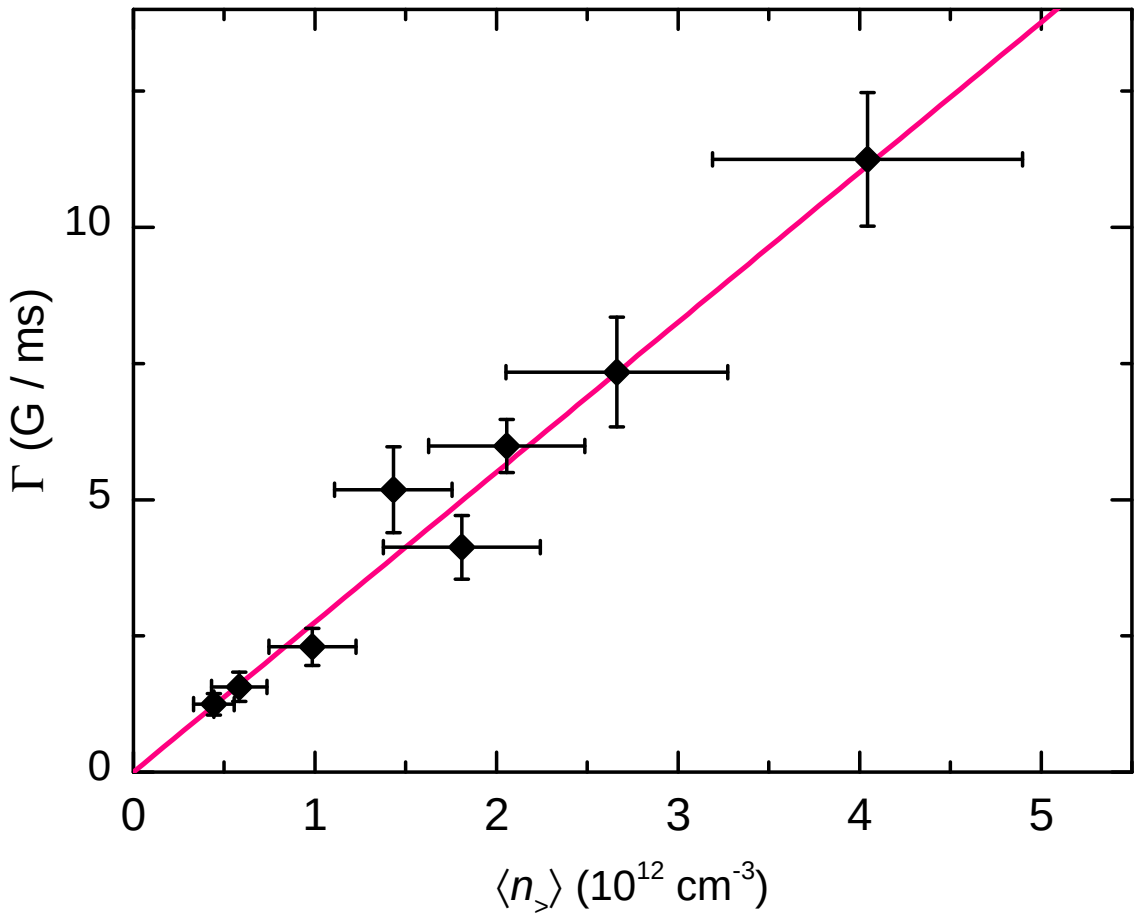

Figure 5.5: The initial molecule conversion efficiency divided by the magnetic-field sweep rate, Γ, vs the density overlap of the two atom clouds.The prediction for Γ using the ^{40}K–^{87}Rb Fano-Feshbach resonance parameters (Eq. (5.5)) is shown as a solid line. Here, the atomic densities are varied by associating molecules at different times during expansion from the optical trap (up to 1.2 ms), as well as by adjusting the evaporation trajectory and optical trap frequencies. This data was published in Reference [55].

data. The same pairing criterion also accurately predicted the saturated molecule number in thermal and degenerate Bose gases [58] and for heteronuclear molecules in a Bose-Bose mixture of ^{87}Rb and ^{85}Rb [59] as well as a Fermi-Fermi mixture of ^{6}Li and ^{40}K [60]. Intuitively, this Stochastic Phase Space Sampling (SPSS) calculation predicts a sharp increase in the molecule fraction as the atoms are brought into the quantum degenerate regime, approaching nearly unit conversion efficiency at zero temperature.

In contrast, the efficiency of molecule creation has been quite low in Bose–Fermi mixtures like ^{40}K–^{87}Rb. The problem of pairing in a strongly interacting Bose–Fermi mixture has been a topic of theoretical interest [10, 61, 62, 63]. On a more practical note, fermionic Feshbach molecules are also an essential step in creating a gas of ultracold polar ^{40}K^{87}Rb molecules. With the long-range anisotropic interactions of polar molecules, physicists could access novel quantum phases of matter and pave the way for many new experiments. However, the inefficiency of Feshbach molecule production limits the initial phase space density of the polar molecular gas. As a consequence, no experiment has yet managed to create a quantum-degenerate Fermi gas of polar molecules in the six years since Feshbach molecules were first adiabatically transferred into the rovibrational ground state [20]. In addition to ^{40}K–^{87}Rb, fermionic Feshbach molecules have also been created in ^{23}Na–^{40}K and ^{6}Li–^{23}Na mixtures [64, 65], and these molecules could conceivably be transferred into their ground state as well. In all of these experiments, the fraction of minority atoms converted to molecules was less than 30 percent.

With a phase-space density criterion for pairing, it is not hard to see why a Bose–Fermi mixture has fewer eligible atom pairs for creating molecules. At zero temperature all of the bosons condense into the ground state of the trap whereas the (spin-polarized) fermions must each occupy different trap states as shown in Figure 5.6. At high temperatures both species are spread out across a broad distribution of momenta and positions. In either limit, most of the fermions and bosons are too far apart in phase space to pair. It is the regime between these limits, where the Fermi gas is quasi-degenerate but the Bose gas has a temperature above the BEC transition, that the highest molecule conversion efficiencies are predicted by the phase-space density pairing (SPSS)

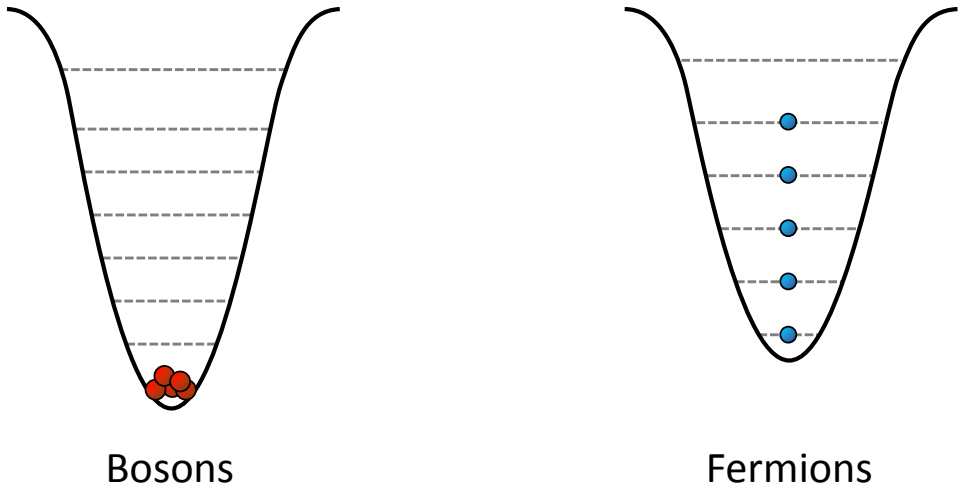

Figure 5.6: Schematic distribution of atoms in an optical trap at low temperatures. The fundamental challenge of pairing bosons with fermions lies in their low-temperature behavior. The bosons condense into the trap's ground state whereas the fermions must each occupy different trap states. Fermi-Fermi and Bose-Bose pairs, on the other hand, see improved phase-space overlap at low temperatures and so more pairs are formed.

model. Although previous measurements of molecule creation in the ^{40}K–^{87}Rb mixture followed the predictions of the SPSS calculation, these were limited to a regime of relatively high T/T_{F} and low number of the fermionic atoms. The measurements in this section pursue the initial conditions for which the greater conversion efficiency was predicted.

Another challenge for heteronuclear Feshbach molecules is that differences in the masses, polarizabilities, and/or magnetic moments of the initial atoms can cause the two atom clouds to have different equilibrium positions in the trap. To measure the significance of this effect on the molecule conversion efficiency, we intentionally separated the ^{40}K and ^{87}Rb clouds along the weak axial direction of the optical trap by applying a magnetic-field gradient before molecule formation. The results of this measurement are shown in Fig. 5.7, where we plot the saturated molecule conversion efficiency against the spatial offset of the two atom clouds. The conversion efficiency drops when the spatial separation is significant compared to the root-mean-squared (RMS) size of the ^{87}Rb gas in the trap, σ_{Rb}. For the data in this Chapter, the spatial offset of the atom clouds in the axial direction is less than 1.2 σ_{Rb} and the calculated offset in the vertical direction due to differential gravitational sag is less than 0.3 σ_{Rb}. These relative displacements of the atom clouds were accounted for in all modeling of the pairing process.

The top panel of Figure 5.8 shows our measurements of the molecule creation efficiency f_0 as a function of T/T_{F} for the initial ^{40}K atom gas. Here, we varied the magnetic-field sweep rate, using the findings of Sec. 5.3 to ensure that the sweeps were sufficiently slow that the molecule number was in the saturated regime. For this data, the number of ^{40}K atoms is larger than the number of ^{87}Rb atoms by a factor between 1.6 and 7. Rb radial (axial) trap frequencies range from 360 to 550 Hz (4 to 6 Hz), and initial atom temperatures are between 250 nK and 770 nK. This broad range of initial conditions is used to provide a stronger test for the SPSS calculation and also to make sure that the ^{87}Rb gas is above the BEC transition temperature for all measurements even when T/T_{F} is low. The absence of a condensate improves phase-space overlap between the two species and minimizes the inelastic loss processes that increase with ^{87}Rb density. As was observed for homonuclear molecules, the conversion efficiency increases for higher initial atomic phase-space

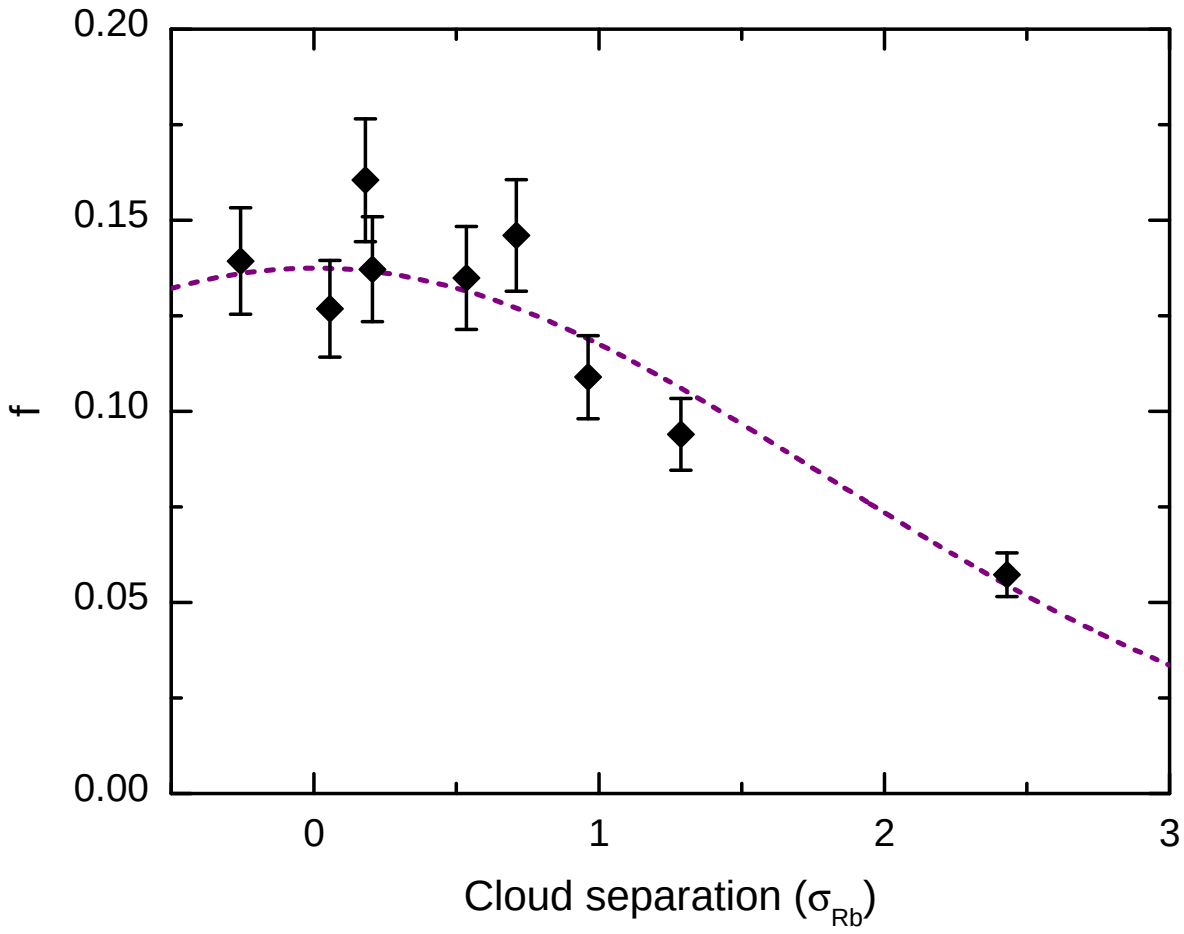

Figure 5.7: Molecule conversion efficiency, f, as a function of the separation between the ^{40}K and ^{87}Rb clouds in units of the width, σ_{Rb}, of the ^{87}Rb cloud, which is the smaller of the two atom clouds. The solid curve shows an empirical fit to a Gaussian with an RMS width of 1.8(1) σ_{Rb}. For this data, molecules are created from 2.8×10^5 ^{87}Rb atoms and 2.1×10^5 ^{40}K atoms at $T =$ 490 nK and T/T_{c}=1.6. This data was published in Reference [55].

densities.

In the bottom panel of Figure 5.8, we compare these results against the Stochastic Phase-Space Sampling (SPSS) calculation developed by Hodby *et al.* [58]. This semi-classical model is based on the idea that two atoms are able to pair if they lie within a volume of relative phase-space set by an adjustable parameter γ:

$$\mu \left| v_{\mathrm{rel}} \right| \left| r_{\mathrm{rel}} \right| < \frac{h}{2}\gamma \tag{5.6}$$

where v_{rel} is the relative speed of the two atoms and r_{rel} is their separation. Another property of the calculation is that atoms are only allowed to pair once (i.e., paired atoms are removed from further consideration). To determine the parameter γ in our system, we fit the molecule creation efficiency data from Fig. 5.8 to the SPSS calculation. First, a Monte-Carlo calculation generates atom distributions matching the initial conditions for each measurement. These atoms are then randomly paired according to the criterion in Eq. (5.6) to determine the molecule creation efficiency, as described in [36]. A fit to the data with initial $T/T_{\mathrm{F}} > 0.55$ returns a value of $\gamma_{\mathrm{BF}} = 0.38(3)$. The error bar is dominated by a 10 percent systematic uncertainty in the measured conversion fraction. This measured γ_{BF} for ^{40}K–^{87}Rb is consistent with the values $\gamma_{\mathrm{F}} = 0.38(4)$ found in ^{40}K and $\gamma_{\mathrm{B}} = 0.44(3)$ measured in ^{85}Rb [58]. Thus, Feshbach molecule formation appears to operate in much the same way for bosons, fermions, and Bose–Fermi mixtures as long as the parent atoms' distributions are well overlapped in the case of the two-species mixture.

As T/T_{F} is lowered, the bosonic ^{87}Rb gas continues to shrink while Pauli pressure forces the ^{40}K atoms into a relatively broad distribution of momenta and positions. The SPSS simulation fully takes into account the differences between Bose and Fermi-Dirac distributions in this regime. Even so, the bottom panel of Fig. 5.8 shows that the SPSS calculation with $\gamma_{\mathrm{BF}} = 0.38$ significantly overestimates the conversion efficiency for atom clouds with low T/T_{F}. No single value of the pairing criterion γ fits the entire temperature range of our data. In contrast, previous measurements for homonuclear Feshbach molecules in ^{40}K agreed with SPSS predictions for T/T_{F} as low as 0.05 [58]. The failure of the SPSS model to describe our measurements in the quantum-degenerate regime

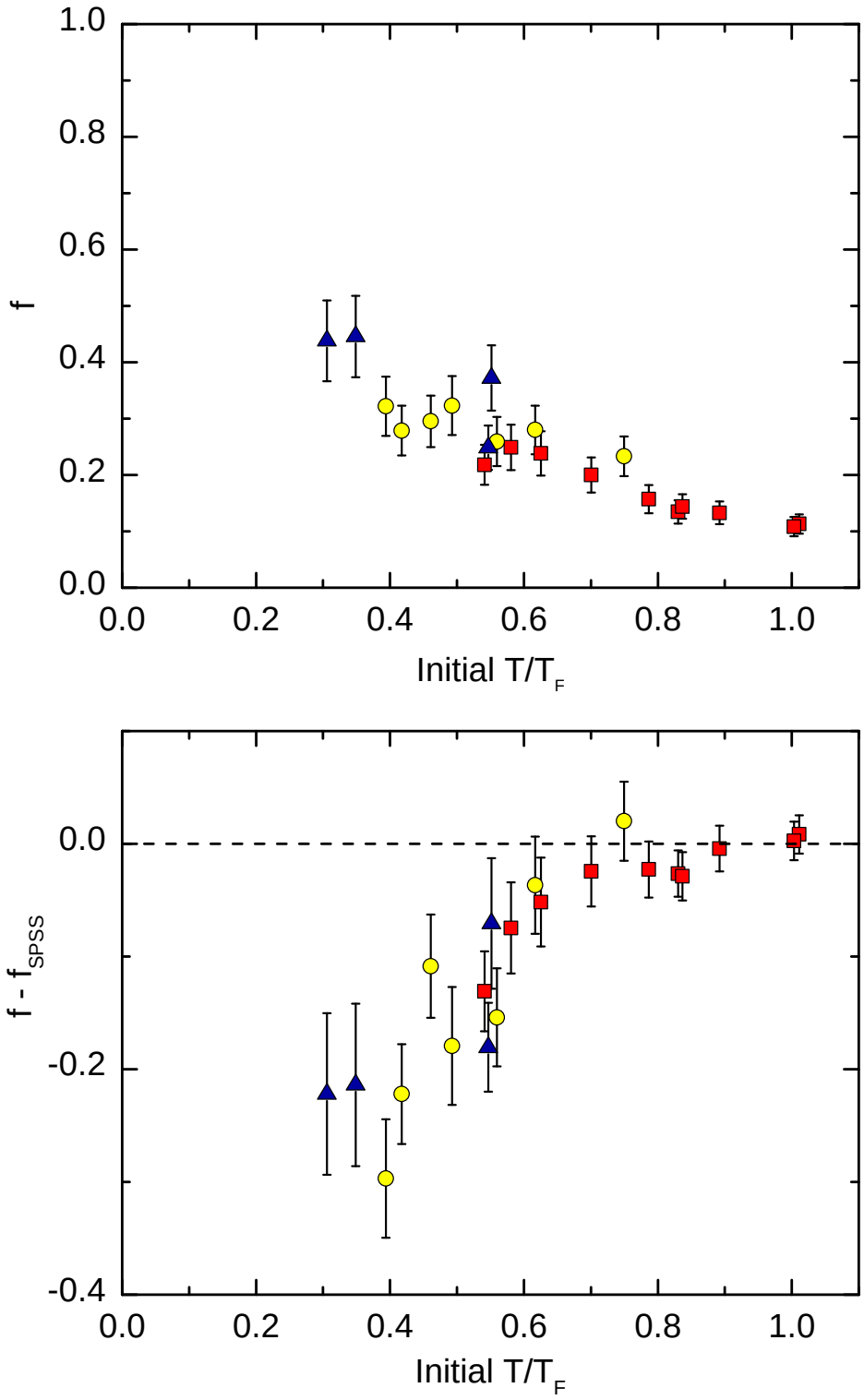

Figure 5.8: Top: Measured conversion efficiency, f, vs the initial T/T_{F} of the ^{40}K atoms. The atom number ratio ranges from $1.6 \leq N_{\mathrm{K}}/N_{\mathrm{Rb}} \leq 2$ (squares), $2 \leq N_{\mathrm{K}}/N_{\mathrm{Rb}} \leq 4$ (circles), or $4 \leq N_{\mathrm{K}}/N_{\mathrm{Rb}} \leq 7$ (triangles). Molecule conversion efficiency increases for higher atomic phase-space density (lower T/T_{F}). Bottom: The difference between the SPSS calculation and the data, $f - f_{\mathrm{SPSS}}$, vs the initial T/T_{F} of the ^{40}K atoms. This data was published in Reference [55].

suggests that this model is inadequate for describing the production of *fermionic* molecules from quantum-degenerate atom gas mixtures.

The phenomenological SPSS model is popular because of its intuitive simplicity and (until now) successful track record. Nevertheless, the pairing criterion γ is not derived but instead is extracted from experiments. This has motivated the development of other, possibly more rigorous, theoretical models. One theory, based on the assumption that chemical equilibrium is maintained through the entire magnetic field ramp, has successfully duplicated the SPSS results with no free parameters for Bose-Bose and Fermi-Fermi pairing in both thermal and quantum-degenerate gases [66]. This model was later extended to include heteronuclear molecules with all combinations of quantum statistics [67]. A more recent theoretical paper compared various incarnations of the SPSS model against this chemical equilibrium theory for all possible combinations of quantum statistics, revealing that the models differ for fermionic molecules in a way that depends on the ratio of the number of atoms from each species [68]. Since the chemical equilibrium models automatically include the quantum statistics of the molecules, it would be interesting to compare these theories against the data of Figure 5.8. Another possibility is that heteronuclear molecule formation involves higher partial waves due to the mismatch in the trap energy levels between the two atom species [69]. A different theoretical approach includes few-body interactions and their influence on the Bose–Fermi pairing process [70], predicting a suppression of pairing that could be related to our observations. Chapters 7 and 8 of this thesis will explore few-body interactions in the ^{40}K–^{87}Rb mixture specifically.

Chapter 6

More KRb molecule results

This Chapter will dive deeper into the world of fermionic Feshbach molecules. Magnetoassociation, which was studied in the previous Chapter, is only one of several ways to generate molecules. Section 6.1 highlights the competing timescales of inelastic collisions that can both produce and destroy Feshbach molecules in a gas of atoms. Just by holding at a magnetic field below the Fano-Feshbach resonance, in some cases we can create as many molecules in the gas as we do by magnetoassociation. In Section 6.2, we use radio frequency photons to directly transfer the atoms into the Feshbach molecule state. Finally, Section 6.3 reports measurements of the temperature of the molecules using time-of-flight expansion after the optical trap is switched off. These experiments reveal a surprising excess of molecular kinetic energy, which is independent of the method by which the molecules are produced.

6.1 Molecules formed by three-body recombination

Inelastic collisions are notorious enemies of ultra cold atom experiments: they release heat and eject atoms from traps, which diminishes the effectiveness of evaporative cooling and can make it essentially impossible for many strongly interacting gases to be studied in equilibrium. This section casts inelastic collisions in a slightly more positive light: at large interspecies scattering lengths, inelastic collisions in the ^{40}K–^{87}Rb mixture actually produce trappable ^{40}K^{87}Rb Feshbach molecules. Recall that three-body recombination results in a diatomic molecule, with kinetic energy equal to the binding energy shared between the molecule and a third atom. When this binding

energy is sufficiently small, as is the case with Feshbach molecules at a high scattering length, the reaction products remain trapped and molecules accumulate in the gas.

Figure 6.1 shows a magnetic-field sequence designed to explore these dynamics by imaging the molecules themselves. As with the data in the previous Chapter, we initially prepare a gas of ^{40}K and ^{87}Rb atoms in the $|f, m_f\rangle = |9/2, -9/2\rangle$ and $|1, 1\rangle$ states. The molecules are dissociated and imaged above the Fano-Feshbach resonance, similar to the timing in the left part of Figure 5.3. A small imaging background, typically about 10^4 atoms, is left over by an imperfect transfer of unpaired K atoms into the invisible $|9/2, -7/2\rangle$ state during the 'clean' stage of the imaging sequence. We measure the size of this effect by preparing a spin-polarized sample of ^{40}K atoms only with no ^{87}Rb present. Since no Feshbach molecules can be made in this mixture, all ^{40}K atoms that can be imaged after the cleaning sequence are attributed to the imaging background. We subtract this background[1] from our measurements of molecule number.

Figure 6.2 shows the molecule number vs $t_{\rm hold}$ measured at a few different scattering lengths near the Fano-Feshbach resonance. For all of these scattering lengths, the Feshbach molecule binding energy is less than 1.2 microKelvin. At short hold times near the resonance, a fast rate of three-body recombination leads to an accumulation of molecules. At longer times, the molecules decay by vibrational relaxation. The single-beam optical trap for these experiments has a period of 160 ms in the weak axial direction and 1.7 ms in the tight radial direction for the ^{87}Rb atoms. There are initially 5×10^5 ^{40}K atoms with an average density of $8 \times 10^{12}/\mathrm{cm}^3$ and 6×10^5 ^{87}Rb atoms with an average density of $1.4 \times 10^{13}/\mathrm{cm}^3$. The two species are prepared at a temperature of 700 nanoKelvin, which is 1.5 times the BEC transition temperature of the ^{87}Rb atoms and 0.6 times the Fermi temperature of the ^{40}K atoms.

Two types of three-body recombination events occur during these experiments. The first type creates a molecule with large binding energy, and it therefore imparts a large kinetic energy to the resulting molecule and atom. Two ^{87}Rb atoms and one ^{40}K atom are lost from the trap for

[1] Since our method of preparing a ^{40}K gas without ^{87}Rb atoms results in a gas with as many as 50% more ^{40}K atoms, we could be overestimating the imaging background.

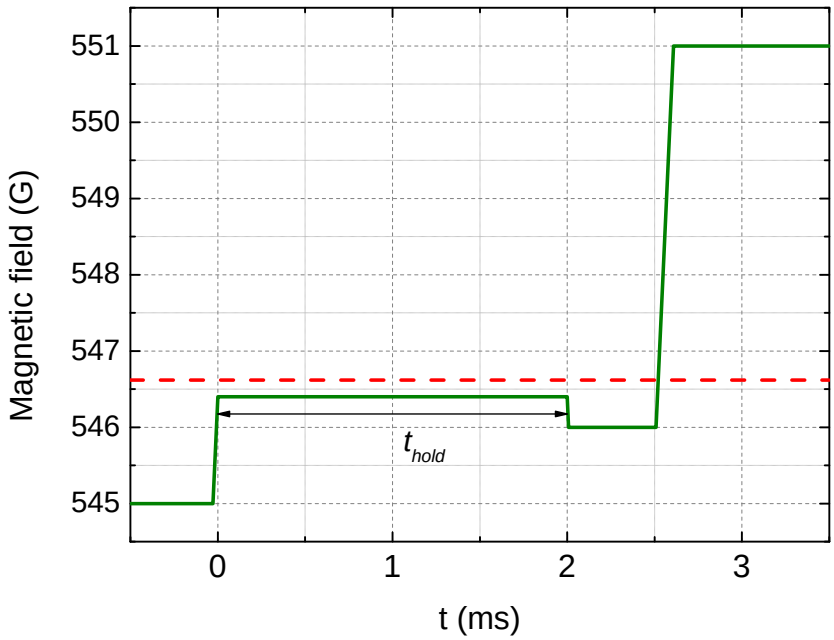

Figure 6.1: Timing sequence for measurements of Feshbach molecules formed by three-body recombination. The ^{40}K and ^{87}Rb atoms are prepared at a weakly interacting scattering length far below the interspecies magnetic Fano-Feshbach resonance. We quickly ramp the field to a strongly interacting value where three-body recombination produces trapped Feshbach molecules. After a variable hold time, t_{hold}, we switch the optical trap off. At this point we also ramp the magnetic field away from the Fano-Feshbach resonance so that a resonant RF pulse can drive the unpaired ^{40}K atoms into the invisible $|9/2, -7/2\rangle$ state. Finally, we ramp the magnetic field across the Fano-Feshbach resonance, which dissociates the Feshbach molecules. The ^{40}K atoms that were previously part of Feshbach molecules are imaged on the cycling $|9/2, -9/2\rangle \rightarrow |11/2, -11/2\rangle$ transition.

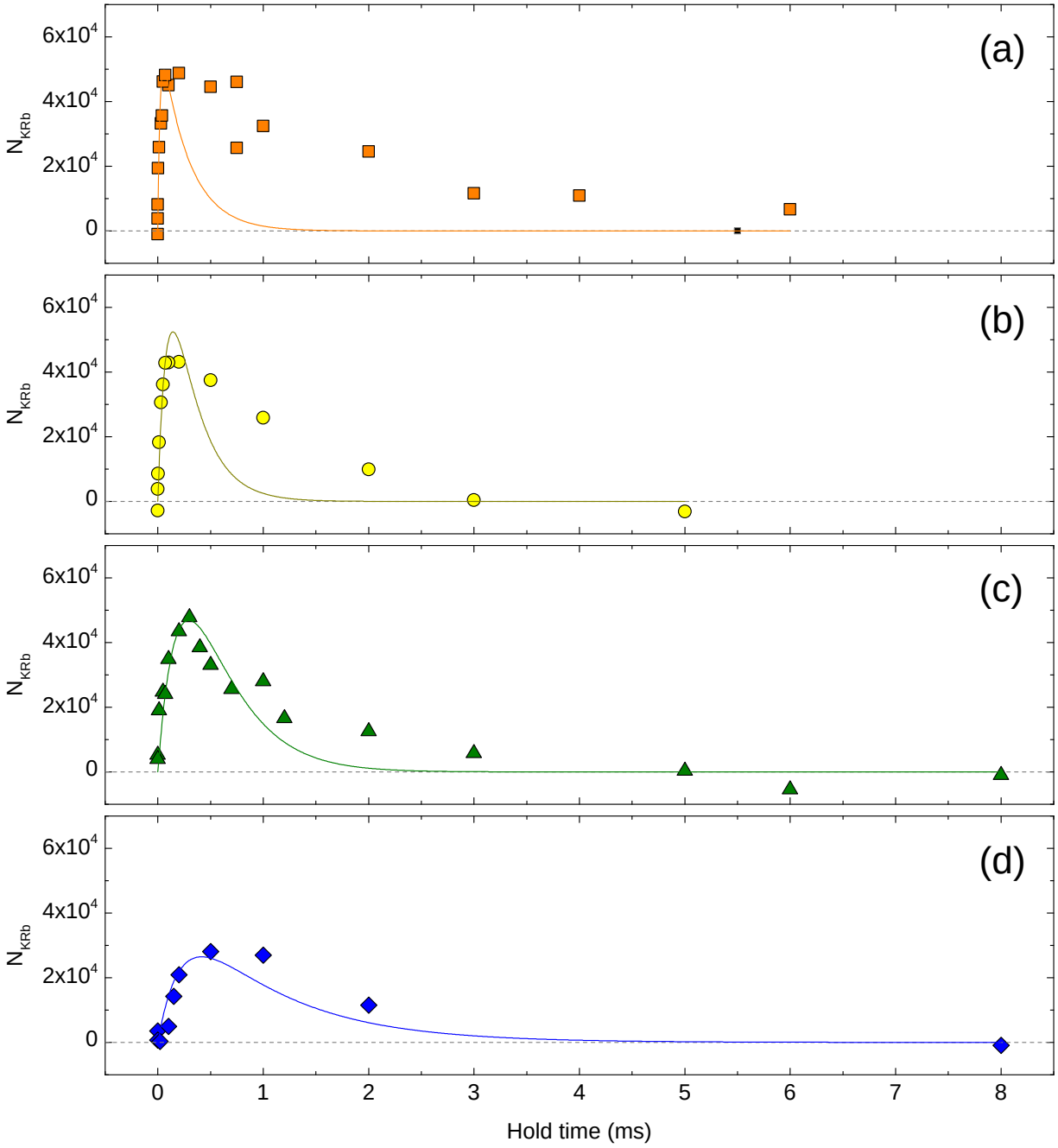

Figure 6.2: The dynamic population of fermionic Feshbach molecules in ^{40}K–^{87}Rb mixtures. The interspecies scattering length is 5100 a_0 for (a), 3400 a_0 for (b), 2500 a_0 for (c), and 1700 a_0 for subplot (d). The lines show fits to Equation 6.4, where the only free parameter is the fraction of three-body recombination events that produce Feshbach molecules, F.

each event. The second type creates a Feshbach molecule, which is trapped for the combinations of optical trap strength and magnetic field that we study here. After a recombination event, one ^{87}Rb atom and one ^{40}K atom are converted into one ^{40}K^{87}Rb Feshbach molecule, but all participants in the reaction remain trapped. The total rate of three-body recombination events is characterized by the rate coefficient α, which is defined by Equation 7.1 and measured in Figure 8.5. At a given magnetic field, a fraction F of these recombination events make Feshbach molecules and the remaining fraction $(1 - F)$ produce deeply bound molecules. In addition to three-body recombination, the molecule population is also affected by inelastic collisions with ^{87}Rb atoms (our measurements in Figure 8.2 show that the rates of inelastic molecule collisions with ^{40}K atoms are much smaller than they are with ^{87}Rb atoms, so we will leave ^{40}K collisions out of this discussion for simplicity). Each of these collisions removes a ^{40}K^{87}Rb molecule and a ^{87}Rb atom from the trap. They are characterized by the loss rate coefficient β, which is defined by Equation 8.1 and measured in Figure 8.2.

Putting all of these pieces together, we get a set of coupled differential equations to model the population of atoms and molecules in the trap as a function of the hold time, t at a magnetic field near the Fano-Feshbach resonance:

$$\dot{N}_{\mathrm{KRb}}(t) = \int d^3\mathbf{r} \ \left[F \ \alpha \ n_{\mathrm{Rb}}^2(\mathbf{r},t) \ n_{\mathrm{K}}(\mathbf{r},t) \ - \ \beta \ n_{\mathrm{KRb}}(\mathbf{r},t) \ n_{\mathrm{Rb}}(\mathbf{r},t)\right] \tag{6.1}$$

$$\dot{N}_{\mathrm{Rb}}(t) = \int d^3\mathbf{r} \ \left[(F-2) \ \alpha \ n_{\mathrm{Rb}}^2(\mathbf{r},t) \ n_{\mathrm{K}}(\mathbf{r},t) \ - \ \beta \ n_{\mathrm{KRb}}(\mathbf{r},t) \ n_{\mathrm{Rb}}(\mathbf{r},t)\right] \tag{6.2}$$

$$\dot{N}_{\mathrm{K}}(t) = \int d^3\mathbf{r} \ \alpha \ n_{\mathrm{Rb}}^2(\mathbf{r},t) \ n_{\mathrm{K}}(\mathbf{r},t) \tag{6.3}$$

Here, $n_{\mathrm{Rb}}(\mathbf{r},t)$ and $n_{\mathrm{K}}(\mathbf{r},t)$ are the atom number densities and $n_{\mathrm{KRb}}(\mathbf{r},t)$ is the number density of the molecules as a function of position and hold time.

To gain intuition about the evolution of the molecule population, let's simplify these equations with a few approximations. First, we approximate the atom clouds as sharing the same gaussian cloud sizes σ_x, σ_y, and σ_z. The equilibrium ratio of ^{40}K cloud size to ^{87}Rb cloud size is 1.07 in our optical trap, which means that the error from this approximation should be small. Second, we neglect the depletion of the majority population of ^{87}Rb atoms. With these approximations, plus

an initial condition with N_{K0} ^{40}K atoms and zero ^{40}K^{87}Rb molecules, the approximate solutions to Equations 6.1 - 6.3 are,

$$N_{\mathrm{KRb}}(t) = \frac{A_0}{A_0 - B_0}\ F N_{\mathrm{K0}}\ \left(e^{-B_0 t} - e^{-A_0 t}\right) \tag{6.4}$$

$$N_{\mathrm{Rb}}(t) = N_{\mathrm{Rb0}} \tag{6.5}$$

$$N_{\mathrm{K}}(t) = N_{\mathrm{K0}}\ e^{-A_0 t} \tag{6.6}$$

where the constant A_0 is equal to $\alpha\ \langle n_{\mathrm{Rb}}^2 \rangle_n$ and the constant B_0 is equal to $\beta\ \langle n_{\mathrm{Rb}} \rangle_n$, and the quantities in angle brackets are density-weighted averages. Equation 6.4 highlights the competition between two timescales: one is set by the rate of loss due to atom-molecule collisions (B_0) and the other by the rate of molecule production due to three-body recombination (A_0). The quantity FN_{K0} is the maximum possible number of molecules that can be created by three-body recombination when ^{40}K is the minority species.

We fit the data in Figure 6.2 the Equations 6.4–6.6, where F is the only free parameter. The results are $F = 0.12(2)$, $F = 0.19(1)$, $F = 0.31(2)$, and $F = 0.38(4)$ for subfigures (a), (b), (c), and (d) respectively. To calculate the rate constants A_0 and B_0, we use our own measurements of atom and molecule loss rates from Chapter 8. Unfortunately, it is clear from the disagreement between the fits and the data in Figure 6.2 that the approximations behind Equations 6.4 were not justified for higher scattering lengths. The depletion and heating of the ^{87}Rb atom population by three-body recombination appears to lengthen the lifetime of the molecules. For a more accurate model, we could solve Equations 6.1–6.3 numerically. In any case, the peak molecule numbers in Figure 6.2 are similar to those from magnetoassociation (see Chapter 5). This is possible because the timescales for three-body recombination are so much faster than those for atom-molecule loss in the ^{40}K–^{87}Rb mixture at high scattering lengths. However, since this method of molecule formation adds kinetic energy to the molecules and is particularly sensitive to fluctuations in the magnetic field or atom density, we do not routinely use it as a starting point for other experiments with molecules.

6.2 Radiofrequency photoassociation

Photoassociation with Radio Frequency (RF) photons is another option for creating Feshbach molecules in a gas of atoms. RF association has been well studied in the ^{40}K–^{87}Rb system, with early measurements of ^{40}K^{87}Rb molecule creation efficiency [33] and lifetime [71] as well as a characterization of the interspecies scattering length via the molecules' binding energy [32]. In this section, we revisit RF photoassociation because it avoids complications associated with crossing the magnetic Fano-Feshbach resonance. In Section 6.3, we investigate the temperature of molecules formed by magnetoassociation and by RF association, and find larger than expected expansion energies in both cases. In this section, we describe our procedure for RF association.

First, we prepare a quantum gas mixture of ^{40}K atoms in the $|9/2, -7/2\rangle$ state and ^{87}Rb atoms in the $|1, 1\rangle$ state at a magnetic field of 540 G. Since the $|9/2, -7/2\rangle$ state does not participate in the Fano-Feshbach resonance at $B_0 = 546.618$ G, the ^{40}K and ^{87}Rb atoms only interact weakly, with the background interspecies scattering length of -187 a_0. To associate molecules, we follow the timing diagram in Figure 6.3. We sweep the magnetic field to 546.1 G in 0.3 ms. We use a Toptica VFG-150 synthesizer to generate a pulse of RF with frequency ν. The RF power has a Gaussian envelope with a $1/e$ full width of 400 microseconds. This pulse is subsequently amplified by a Minicircuits ZHL-5W-1 amplifier and broadcast to the atoms using a resonant antenna.

Figure 6.4 shows the resulting RF spectrum. The leftmost peak is due to the bare $|9/2, -7/2\rangle \rightarrow |9/2, -9/2\rangle$ transition at $\nu_0 = 80.0392(4)$ MHz for the ^{40}K atoms. The resonant frequency ν_0 corresponds to a magnetic field of 546.13 G, where the interspecies scattering length is 980 a_0. The shorter asymmetric peak on the right side is from the photoassociation of Feshbach molecules, with a peak value of $N_{KRb} \approx 30,000$ molecules. The distance between these peaks corresponds to the binding energy of the KRb Feshbach molecule state. Equation 2.2 predicts a molecule binding energy of 80 kHz at this magnetic field, which would correspond to a resonant frequency of 80.12 MHz on the x axis of Figure 6.4.

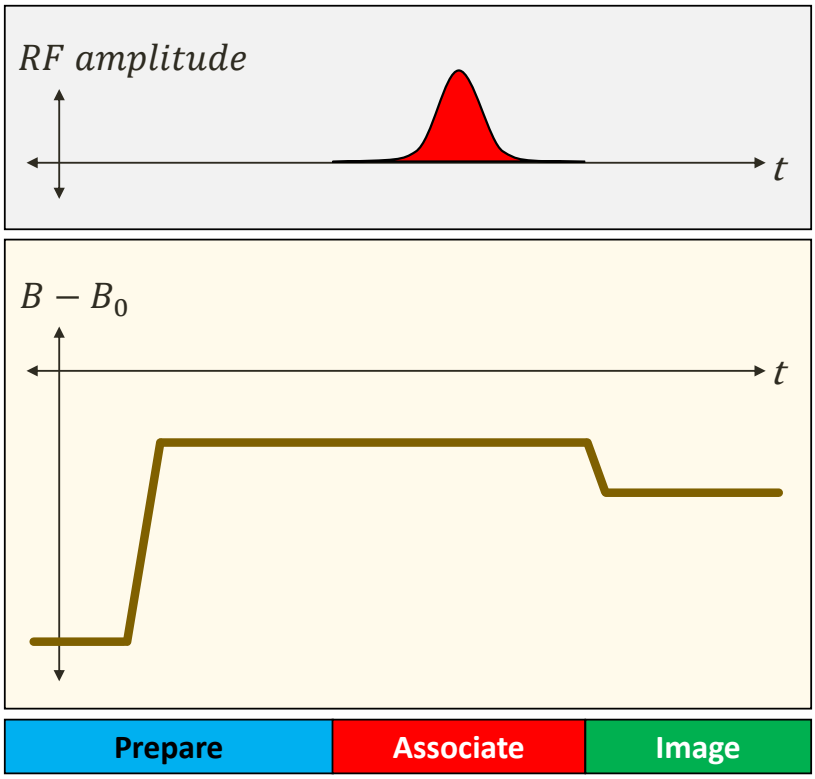

Figure 6.3: Timing diagram for RF photoassociation of fermionic Feshbach molecules. The ^{40}K and ^{87}Rb atoms are prepared in the $|9/2, -7/2\rangle$ and $|1, 1\rangle$ states. We ramp the magnetic field to a value within 1 Gauss of the Fano-Feshbach resonance and hold for a few milliseconds to allow small magnetic-field transients to damp out. A gaussian RF pulse, blue-detuned from the ^{40}K $|9/2, -7/2\rangle \rightarrow |9/2, -9/2\rangle$ transition, then drives ^{40}K atoms into the ^{40}K^{87}Rb Feshbach molecule state. Next, the optical trap is switched off and the gas of atoms and molecules expands. Finally, the molecules are imaged directly using the $|9/2, -9/2\rangle \rightarrow |11/2, -11/2\rangle$ optical transition.

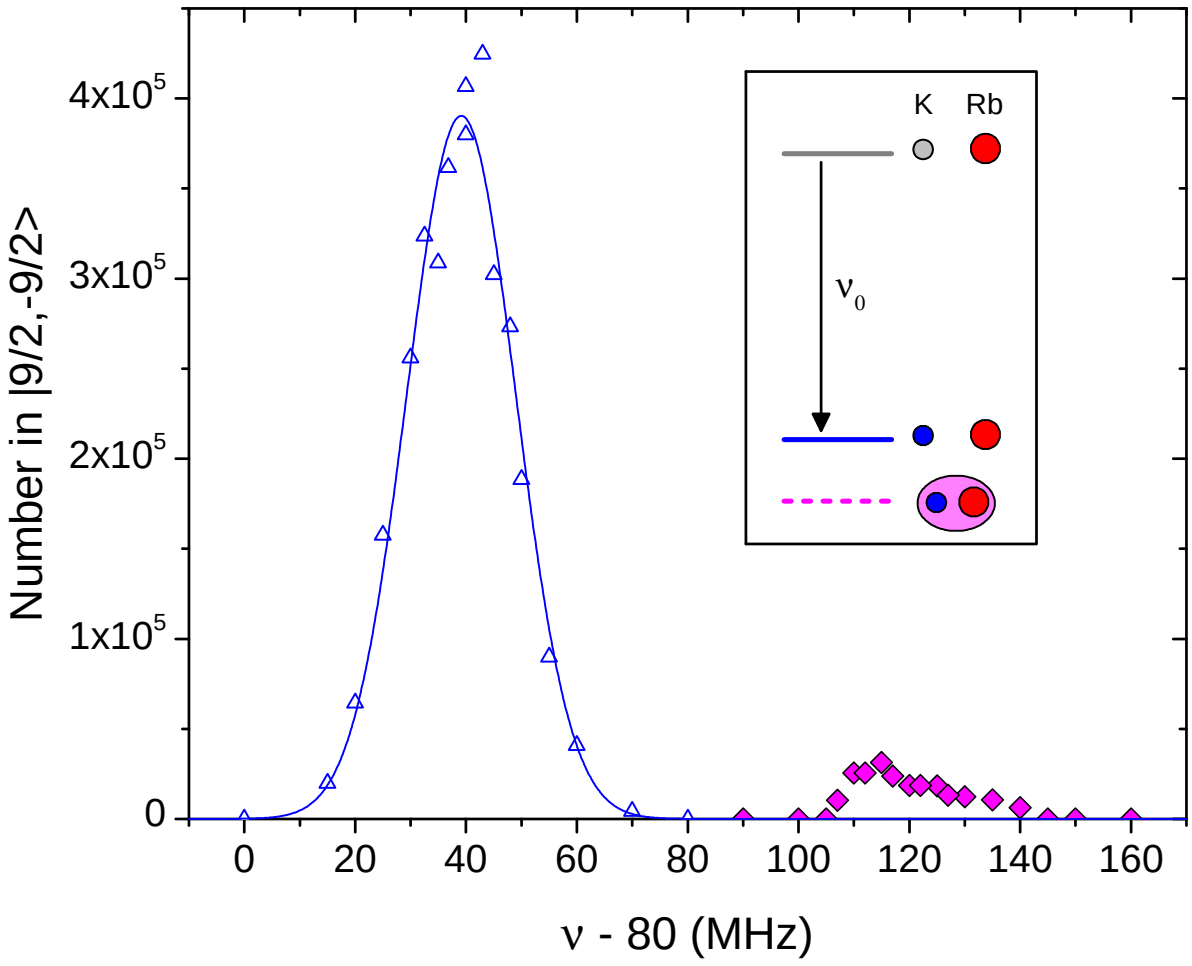

Figure 6.4: RF spectrum for ^{40}K atoms prepared in the $|9/2, -7/2\rangle$ state, in a mixture with ^{87}Rb atoms in the $|1, 1\rangle$ state. The bare ^{40}K $|9/2, -7/2\rangle \rightarrow |9/2, -9/2\rangle$ transition is measured with a 40 μs Gaussian RF pulse (left peak, hollow triangles) and the ^{40}K^{87}Rb photoassociation transition is measured with a 400 μs Gaussian RF pulse (right peak, filled diamonds). The inset shows schematic energy levels for the experiment.

6.3 Excess molecule kinetic energy

Up to this point, we have focused on the *number* of fermionic pairs in the ^{40}K–^{87}Rb mixture. Since many experiments seek to create degenerate gases of Feshbach molecules, the *temperature* of these pairs is also an essential quantity. One previous experiment created fermionic ^{40}K^{87}Rb molecules and measured their temperature to be 300 nK, whereas the temperature of the atom gas was initially 150 nK [33]. Later, a different group created fermionic ^{23}Na^{40}K molecules with a temperature of 500 nK, even though the temperature of the atoms was initially only 220 nK [64]. In contrast, an experiment with bosonic ^{6}Li^{40}K molecules found that the molecules had the same temperature as the gas of atoms that they were created from [60].

Since conservation of momentum should cause a Feshbach molecule to inherit the center-of-mass momentum of its parent atoms, it is surprising that the fermionic molecules do not also appear to inherit the temperature of the atom gas. In this Section, our measurements show that the temperature of the ^{40}K^{87}Rb molecules is consistently higher than that of the atoms, over a broad range of initial densities and temperatures, and that this behavior is consistent regardless of whether molecules are formed by magnetoassociation or by RF photoassociation. We measure the temperature of the molecules from their kinetic energy during time-of-flight expansion in one radial trap direction, which is shown in Figure 6.5. Using the ^{87}Rb atoms as a thermometer, we predict the expansion velocities of the ^{40}K atoms as well as the ^{40}K^{87}Rb molecules. Whereas the ^{40}K atoms match the expected velocity quite well, the molecules in this measurement expand faster than our prediction by a factor of 1.2.

Figure 6.6 summarizes the molecule expansion energy along one direction, $E = \frac{1}{2}m\langle v_{KRb}^2\rangle$, from measurements similar to Figure 6.5 over a broad range of initial atom conditions. At $T/T_F < 0.5$, where the ^{40}K atoms have extra average kinetic energy compared to the Maxwell-Boltzmann distribution, we modify our calculation of the expected molecule expansion energy (grey solid line). First, we calculate the kinetic energy of the ^{40}K atoms numerically from the thermal distribution of an ideal non-interacting degenerate Fermi gas following [54] (blue dashed line), at the temperature

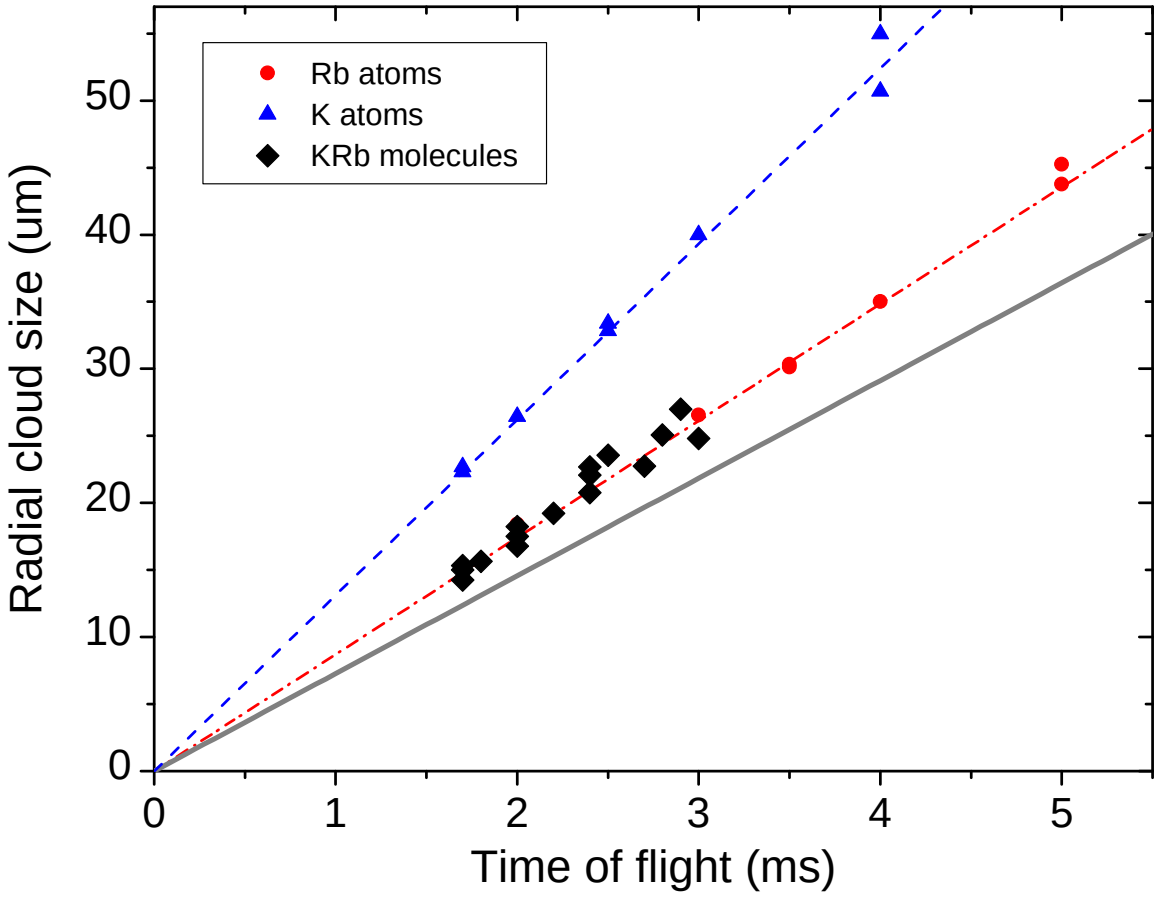

Figure 6.5: Measured RMS cloud widths σ for ^{87}Rb atoms (red circles), ^{40}K atoms (blue triangles), and ^{40}K^{87}Rb molecules (black diamonds). The ^{87}Rb expansion data fit to a line through the origin with slope $v_{Rb} = 8.71(7)\mu$m/ms (red dash-dotted line), which corresponds to $T = 800$ nK. The blue dashed line shows the predicted expansion velocity for ^{40}K atoms at the same temperature, $v_K = v_{Rb}\sqrt{m_{Rb}/m_K}$, which fits the data quite well. In contrast, the measured expansion velocity for the molecules is higher than the predicted $v_{KRb} = v_{Rb}\sqrt{m_{Rb}/m_{KRb}}$ (grey solid line). For this experiment, the molecules are created following the timing diagram in figure 5.4 with $t_{\mathrm{release}} = 0$. The initial average in-trap densities are 5×10^{12} / cm^3 for the ^{40}K atoms and 7×10^{12} / cm^3 for the ^{87}Rb atoms. The optical trap has a weak axial trapping frequency $f = 7$ Hz and two tight radial trapping frequencies of 600 Hz for the ^{87}Rb atoms. For these conditions, the ^{40}K atoms are at $T/T_{\mathrm{F}} = 0.7$.

measured from the expansion energy of the ^{87}Rb gas. Next, we use this calculation to predict the distribution of ^{40}K^{87}Rb molecule energies. Center-of-mass momentum is conserved by the molecule formation process, so that $m_{KRb}\vec{v}_{KRb} = m_K\vec{v}_K + m_{Rb}\vec{v}_{Rb}$ where the m_x refers to mass and $\vec{v}_x$ refers to velocity for each species x. Solving for the root-mean-squared molecule velocity of the molecules, we get

$$\langle v_{KRb}^2 \rangle = \frac{m_K^2 \langle v_K^2 \rangle + m_{Rb}^2 \langle v_{Rb}^2 \rangle}{m_{KRb}^2} \tag{6.7}$$

where the average of the dot product between the ^{87}Rb and ^{40}K velocities is presumed to be zero. Equation 6.7 combines the numerically calculated value for $\langle v_K^2 \rangle$ with the Maxwell-Bolzmann formula, $\langle v_{Rb}^2 \rangle = 3k_BT/m_{Rb}$, to predict the average kinetic energy of the molecules, which is plotted as a thick grey line in Figure 6.6.

On average, the measured energy for the molecules in Figure 6.6 is 1.6(2) times the simple prediction in Formula 6.7. Figure 6.6 clearly shows that the extra ^{40}K^{87}Rb molecule energy in our measurements is present regardless of the initial degeneracy of the ^{40}K gas, or the density of ^{87}Rb atoms that can undergo collisions with the molecules. Furthermore, the fact that the RF photoassociated and magnetoassociated ^{40}K^{87}Rb molecules have the same measured expansion energy rules out any heating that might have occurred as the magnetic field crossed the Fano-Feshbach resonance. Another difference between these two methods is that the unpaired ^{40}K atoms remain in the resonantly interacting $|9/2, -9/2\rangle$ state after magnetoassociation whereas they are in the non-resonant $|9/2, -7/2\rangle$ state after RF photoassociation. Therefore we can also rule out interactions with unpaired resonant ^{40}K atoms as the cause of the mysterious extra energy.

To further exclude ^{87}Rb atoms as culprits, we measured the expansion of ^{40}K^{87}Rb molecules from the trap after the unpaired ^{87}Rb atoms were removed from the trap. Figure 6.7 shows the expansion of molecule clouds with and without the ^{87}Rb removal sequence, which combines Adiabatic Rapid Passage to the $|2, 2\rangle$ state with resonant light on the cycling $|2, 2\rangle \rightarrow |3, 3\rangle$ transition. Since the experiment is performed in a crossed dipole trap, we monitor the expansion in the tight radial direction as well as the weak axial direction. In both directions, there is a negligible difference in

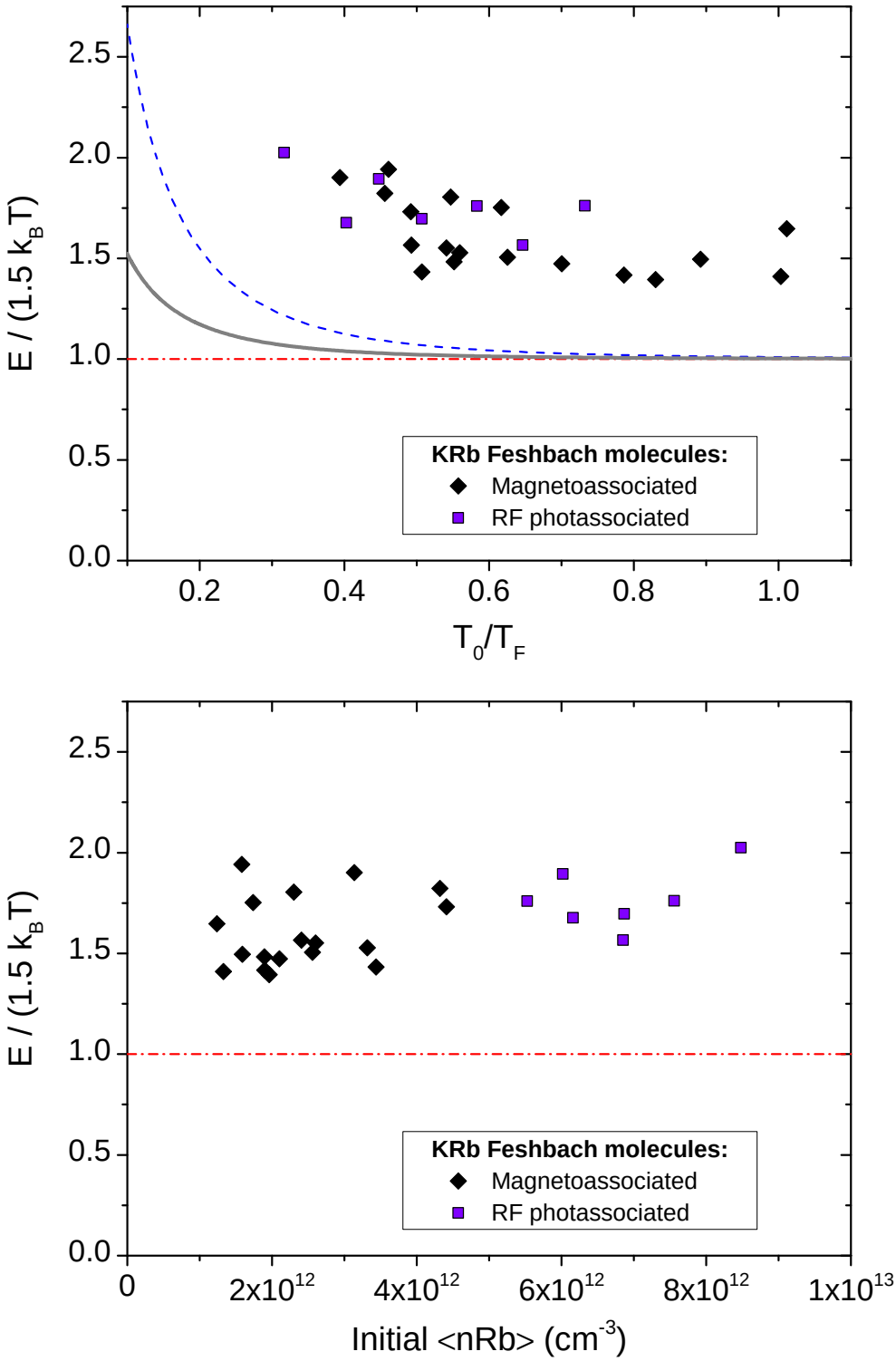

Figure 6.6: The measured kinetic energies for molecules formed by magnetoassociation (black diamonds) and RF photoassociation (purple squares). Top: For different intial T/T_F of the ^{40}K atoms. The expansion energy of the ^{87}Rb atoms is used to measure the temperature (red dash-dotted line), from which we predict the expansion energy of the ^{40}K atoms (blue dashed line) and ^{40}K^{87}Rb molecules (grey solid line). Bottom: The same data are plotted against the initial average density of ^{87}Rb atoms. Because the temperature appears to be independent of the density of ^{87}Rb atoms, we conclude that inelastic collisions with these atoms cannot account for all of the increased temperature of the molecules.

the expansion rates for molecules with and without the ^{87}Rb atoms. This result implies that the extra expansion energy is not being caused by interactions between the unpaired atoms and the molecules during expansion. In addition, the measured expansion velocities are 6.2(3) μm/ms in the axial direction and 6.6(1) μm/ms in the radial direction, which are consistent with each other. This rules out the possibility that the fast radial expansion in Figure 6.6 could be a signature of hydrodynamic expansion in the strongly interacting gas, where one would have slower expansion in the axial direction.

At the time of this writing, the temperature of the KRb molecules remains difficult to explain. In the remaining Chapters of this thesis, I will present measurements of three-body effects that indicate a strong interaction between KRb molecules and Rb atoms. It is possible that these interactions are affecting the physics of molecule formation in the ^{40}K–^{87}Rb gas mixture. Another possibility is that the Fermi statistics of the molecules somehow plays a role.

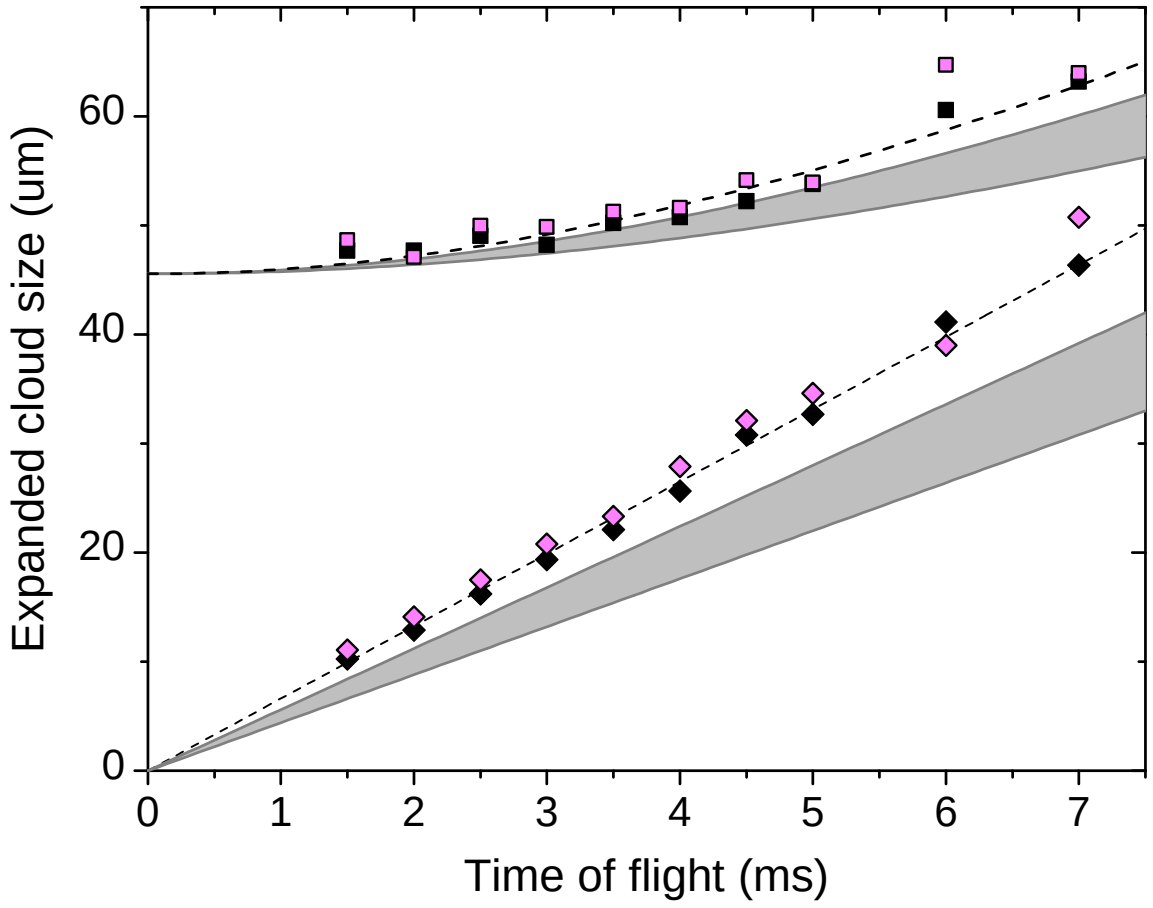

Figure 6.7: Expansion of ^{40}K^{87}Rb molecules from a crossed dipole trap. Squares (larger cloud sizes) indicate the measured axial cloud sizes and diamonds (smaller cloud sizes) indicate the measured radial cloud sizes. The solid black points show the expansion of molecules in the presences of unpaired ^{87}Rb atoms whereas the pink points show the expansion of the molecules after unpaired ^{87}Rb atoms have been removed from the trap. The grey bands show the expected molecule expansion velocities based on Equation 6.7 including the distribution of the quantum-degenerate ^{40}K atoms with initial $T/T_{\mathrm{F}} = 0.3$. The range of the bands reflects the difference between the ^{87}Rb temperature measured before and after molecule formation.

Chapter 7

The Efimov Effect

This Chapter lays the ground work for our measurements of three-body collisions, which are presented in Chapter 8. First, Section 7.1 reviews the Efimov effect, which is becoming a standard framework for understanding few-body physics in quantum systems. The Efimov effect is based on a fascinating solution to the problem of three strongly interacting quantum particles: an infinite series of three-body bound states that obey a discrete scale invariance. Although the Efimov effect was originally proposed in the context of nuclear theory, gases of ultra cold atoms are a nearly ideal platform to explore this effect because the interactions can be controlled by magnetic fields near Fano-Feshbach resonances. The Efimov states in these gases mediate resonant inelastic collisions, which is a major source of data on few-body interactions as described in Section 7.2. Finally, Section 7.3 discusses emerging patterns in the measured spectra of Efimov states across different atomic species as well as predictions of how the ^{40}K–^{87}Rb mixture might fit in.

7.1 Echoes of nuclear physics in quantum gases

The three-body problem is generically difficult; even the classical orbits of three planets with gravitational interaction need to be solved numerically, and, in many cases, the system is chaotic [72, 73]. In 1970, Vitaly Efimov insightfully observed that the problem of three resonantly interacting quantum particles can be reduced to an effective $1/R^2$ potential, and derived analytic solutions for the three-body bound states [74]. Figure 7.1 sketches the energies of Efimov's states. This solution has become an important paradigm in the study of few-body interactions (review

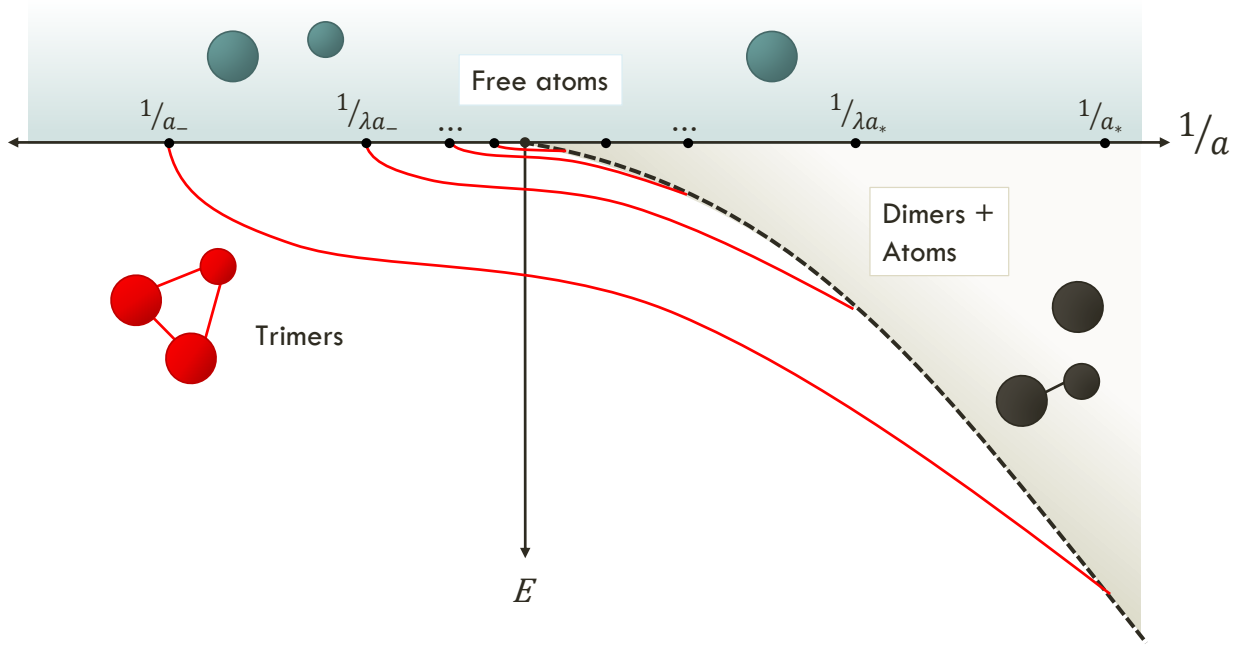

Figure 7.1: A cartoon of the energy spectrum for three atoms with resonant interactions. The two-body scattering length a diverges at the Fano-Feshbach resonance at the origin. $E = 0$ represents the threshold for a continuum of free three-atom states. A two-body Feshbach molecule state exists at positive scattering lengths (black dashed line). An infinite series of universal three-body Efimov states (red lines) is present when the interaction strength diverges. The Efimov states become degenerate with the threshold of free atom energies at negative scattering lengths $\lambda^n a_-$ where $n =\in \{0, 1, 2, ...\}$. At positive scattering lengths $\lambda^n a_*$, the Efimov states are degenerate with the threshold of energies for a Feshbach molecule plus a free atom.

articles include References [23, 75, 24, 76]). More broadly, the Efimov states set a length scale when others diverge at the Fano-Feshbach resonance. In addition, the Efimov states potentially impact many-body physics in unitary quantum gases [77, 78].

The Efimov three-body bound states have intriguing properties. Where the scattering length a diverges, they obey a discrete scale invariance: for each state there exists one even larger by a factor of λ [74]. They can even exist when the two-body potential doesn't support a bound state, which has drawn comparisons between Efimov states and Borromean rings (Figure 7.2). Like Feshbach molecules, the Efimov states reach a spatial extent that spans far beyond the scale of inter-particle forces [29]. One recent paper observed evidence of a three-atom Efimov state on the order of 1 μm in size [79]. The states are also universal, in that their properties are determined solely by the two-body scattering lengths and a three-body parameter κ_* that determines the location of the first Efimov state. This independence from microscopic detail means that Efimov's solution can be applied to both nuclear structure and interactions between ultra cold atoms in spite of the vast difference between their energy scales [76].

The scaling factor $\lambda = e^{\pi/s_0}$ is determined by a transcendental equation that only depends on the number of resonant pairwise interactions between the constituent particles and the ratio between the masses of these particles [80]. When only one of three pairwise interactions is resonant, there is no Efimov effect all. For three equal-mass particles where all three pairwise interactions are resonant, we have $\lambda = 22.7$. This is comparable to the tuning range over which a is the dominant length scale in most quantum gas experiments near Fano-Feshbach resonances. When only two pairwise interactions are resonant in three-body systems of equal-mass particles, the density of Efimov states drops to $\lambda = 1986$ [81]. The mass ratio can have a huge impact on λ. For heavy-light-light combinations with resonant interspecies interactions the value of λ increases sharply, making the observation of an Efimov state extremely unlikely. On the other hand, heavy-heavy-light combinations see an enhanced density of Efimov states. Our ^{40}K–^{87}Rb mixture has $\lambda = 123$. The recently achieved ^{133}Cs-^{133}Cs-^{6}Li quantum gas mixture has $\lambda = 5.5$, making it possible to see the Efimov state sequence repeat itself three consecutive times [82, 83]. Figure 7.3 illustrates the

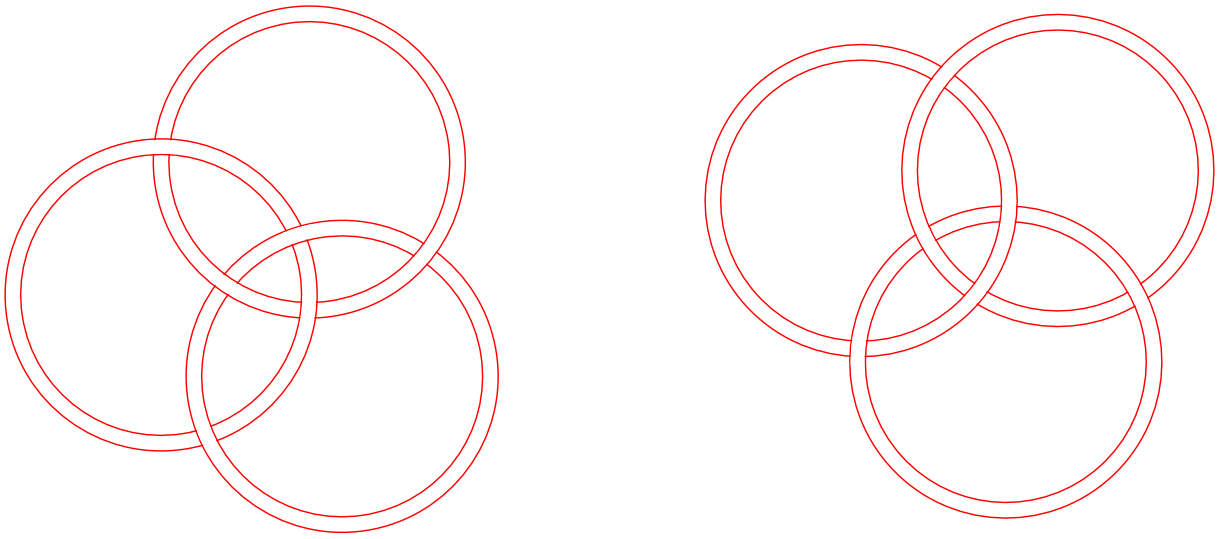

Figure 7.2: A topological analogy to the Efimov bound states. The triplet on the left is in a 'Borromean' configuration such that no single pair of rings is linked. Similarly, Efimov states remain bound at negative scattering lengths where there is no two-body Feshbach bound state. The triplet on the right is in a 'tango' configuration, where each pair of rings is linked. This matches the situation at positive scattering lengths where both two-body Feshbach and three-body Efimov bound states exist.

wide variety of λ values in three-body systems.

Another requirement for the Efimov effect to occur is that the resonant pairwise interactions overwhelm other energy scales. Since the long-ranged Coulomb repulsion between charged particles overwhelms the Efimov $1/R^2$ potential, nuclear Efimov states are most likely to exist in the so-called 'halo nuclei' where a neutral core is orbited by two loosely bound neutrons, such as ^{11}Li or ^{20}C [84, 29]. Though no definitive sign of a nuclear Efimov state has been observed at the time of this writing, the prospect of observing them in halo nuclei continues to drive experimental and theoretical research [85, 86]. The extreme mass ratio in these nuclei unfortunately leads to an unfavorable density of Efimov states. The ^{11}Li (^{9}Li$-n-n$) nucleus has $\lambda = 3 \times 10^{18}$, for example. Whereas extraordinary fine tuning is required on Nature's part to realize a nuclear Efimov states, the scattering parameters in cold atoms can be easily tuned by physicists thanks to Fano-Feshbach resonances. Dozens of Efimov states have been catalogued from observations in ultracold atomic gases since their initial observation in a gas of neutral Cesium [22]. For these experiments, Efimov physics can be explored over scattering lengths that are between the finite range of the two-body potential (set by the van der Waals length for wide Fano-Feshbach resonances) and the smallest of either the thermal deBroglie wavelength or the inter-particle spacing. In practice this means that the atoms must be in the ultra cold regime to observe Efimov effects, and that it is possible to explore a broader range of interaction strengths by reducing the temperature and density of the atomic gas [87, 79].

7.2 Inelastic collisions as a signature of Efimov states

All of the Efimov states to be identified so far in ultra cold atomic gases have been too short-lived for direct observation. Instead, experimentalists typically rely on measurements of scattering rates to point the way to the Efimov spectrum[1] . When an Efimov state becomes degenerate with the free atom threshold at negative scattering length a_-, strong three-body correlations mediate a resonant increase in the rate of three-body recombination. Similarly, at positive scattering length a_*

[1] Another less common method is to photo associate the three-body states directly [88, 89, 90].

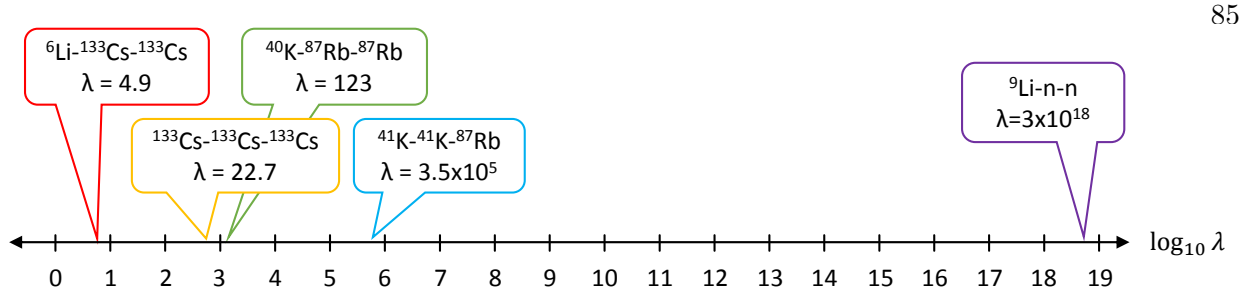

Figure 7.3: The length scaling factor $\lambda = e^{\pi/s_0}$ for a few systems of interest. Heavy-Heavy-Light mass systems have a high density of Efimov states, whereas Heavy-Light-Light mass systems have extremely sparse Efimov states.

where the Efimov state's energy intersects the threshold for an atom and a Feshbach molecule, there is a resonant increase in the rate of inelastic atom-molecule collisions. These scattering lengths are marked in Figure 7.1. There is also an interference minimum located at positive scattering length a_+, where the three-body recombination rate is reduced. These three Efimov features at a_-, a_*, and a_+ form a universal sequence that repeats itself every time the scattering length is changed by a factor of λ. The details of the universal functions for scattering rates near Efimov resonances are covered in [23] and extended to heteronuclear mixtures in [81].

The first observation of an Efimov state was performed by cataloguing the three-body recombination rate in an ultra cold gas of identical ^{133}Cs atoms [22], a method that remains widely used today. In three-body recombination, three atoms collide to form a diatomic molecule. An amount of kinetic energy equal to this binding energy is then shared between the resulting molecule and a third atom. This energy is usually sufficient to eject the atom and molecule from the trap. For the ^{40}K–^{87}Rb system with resonant interspecies interactions, two channels exist for interspecies three-body recombination; however, only ^{87}Rb+^{87}Rb+^{40}K supports Efimov resonances [23], while ^{87}Rb+^{40}K+^{40}K loss is suppressed by Fermi statistics. Therefore we are most interested in the former process, which involves two bosons and one fermion. In order to compare measurements taken under different experiment conditions, we define the density-independent three-body recombination

rate coefficient α by

$$\dot{N}_{\mathrm{Rb}}(t) = 2\dot{N}_{\mathrm{K}}(t) = -2\alpha \int d^3\mathbf{r}\; n_{\mathrm{K}}(\mathbf{r},t)\; n_{\mathrm{Rb}}^2(\mathbf{r},t), \tag{7.1}$$

where $n_{\mathrm{Rb}}(\mathbf{r},t)$ and $n_{\mathrm{K}}(\mathbf{r},t)$ are the densities of ^{87}Rb and ^{40}K, respectively.

The recombination rate increases dramatically near Fano-Feshbach resonances, where α scales as a^4 [91]. The Efimov states modulate this overall dependence, leading to a universal pattern of peaks and valleys that has been observed in a variety of cold atom experiments [24]. For $a < 0$ in the ^{40}K–^{87}Rb–^{87}Rb system [81], we have

$$\alpha(a<0) = \frac{C_\alpha}{2} \frac{\coth(\pi s_0)\sinh(2\eta_*)}{\sin^2[s_0\,\ln(a/a_-)] + \sinh^2(\eta_*)} \frac{\hbar a^4}{m_K}, \tag{7.2}$$

whereas for positive a,

$$\alpha(a>0) = C_\alpha \Bigg(\frac{\sin^2[s_0\,\ln(a/a_+)] + \sinh^2\eta_*}{\sinh^2(\pi s_0+\eta_*) + \cos^2[s_0\,\ln(a/a_+)]} + \frac{\coth(\pi s_0)\cosh(\eta_*)\sinh(\eta_*)}{\sinh^2(\pi s_0+\eta_*) + \cos^2[s_0\,\ln(a/a_+)]} \Bigg) \frac{\hbar a^4}{m_{\mathrm{K}}}. \tag{7.3}$$

Here, m_{K} is the mass of ^{40}K (or, more generally, the lighter atom). The coefficients C_α and s_0 are determined by the mass ratio and the number of resonant interactions. For ^{40}K–^{87}Rb–^{87}Rb, Reference [81] calculates $C_\alpha = 354$ and $s_0 = 0.6536$. The decay factor η_* accounts for the finite lifetime of the Efimov states, and can be different for different atomic systems. The equation for $a > 0$ contains two terms because there are two recombination channels: the first term is for recombination that forms a Feshbach molecule state, and the second term is for recombination that forms a deeply bound molecule.

The predicted loss resonances at at a_- and a_+ are quite dramatic, with a wide base and a typical height spanning orders of magnitude in α. Figure 7.4 plots Equations 7.2 and 7.3 for the ^{40}K–^{87}Rb–^{87}Rb system. Here, we choose the resonance locations based on previous measurements in the ^{41}K–^{87}Rb–^{87}Rb system [92] as described in the next Section. The different colored solid lines show a typical range of values for η_* across cold atom experiments. As η_* increases, the resonances become broader. The overall value of α also increases with η_* at negative scattering lengths, even

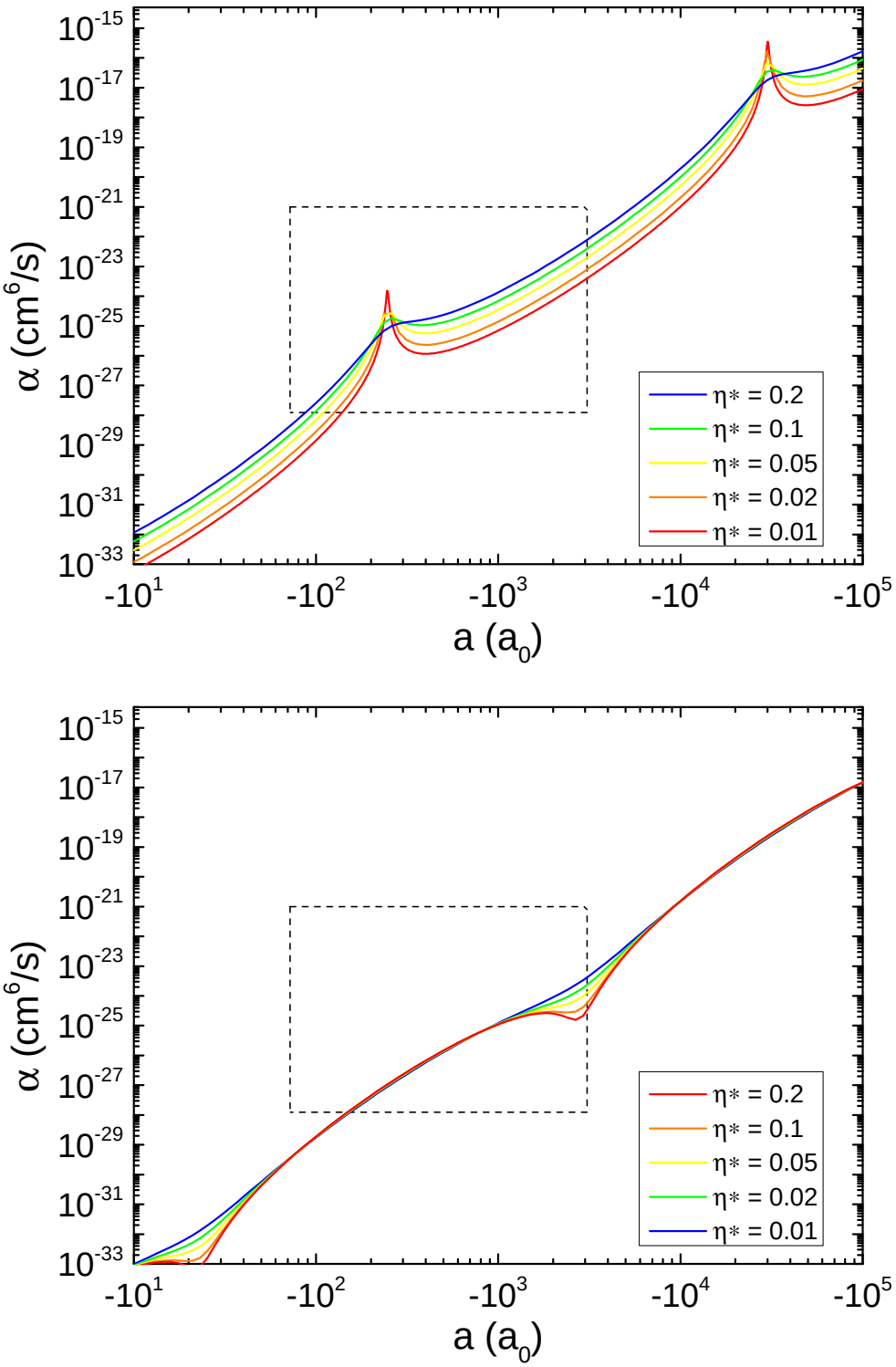

Figure 7.4: Theoretical α vs. a for ^{40}K–^{87}Rb–^{87}Rb three-body recombination from Equations 7.2 and 7.3. Top: loss peaks at negative scattering lengths $\lambda^n a_-$. Our measurements in Chapter 8 access the ranges within the dashed lines. Bottom: interference minima at positive scattering lengths $\lambda^n a_+$.

in the regions between Efimov resonances. Notice the periodicity of the resonances, which repeat each time the scattering lengths change by $\lambda = 122.7$.

Our experiments, described in Chapter 8, can measure the region inside of the dashed lines in Figure 7.4, which spans about half of the period of the Efimov spectrum. Recall that the Efimov model is valid when the scattering length overwhelms the other length scales of the system. This region is bounded at low scattering lengths by the van der Waals length, $r_{\rm vdW} = 72\ a_0$, and at high scattering lengths by the thermal wave vector $1/k \approx 3000\ a_0$. The trap lifetime for the atoms is about 45 seconds, which, for typical densities, makes it difficult to measure values of α lower than 10^{-28} cm^6/s. The upper bound for α is set by the unitarity limit which is $\alpha_{\rm sat} = \hbar 192\pi^2/(2\mu_{\text{K-Rb-Rb}}k^4) \approx 10^{-21}$ cm^6/s [87]. The maximum values for a and α both increase for colder temperatures, however we are limited to temperatures above 200 nanoKelvin in order to maintain a good overlap between the ^{40}K and ^{87}Rb clouds.

Another type of Efimov resonance occurs in the atom-molecule scattering rate when an Efimov state becomes degenerate with the energy threshold for a free atom and a Feshbach molecule [93, 23]. These resonances are less well-understood than their three-body recombination counterparts, due in part to the relatively high difficulty of preparing and measuring a gas of Feshbach molecules. In our quantum gas mixture, the Efimov states have two ^{87}Rb atoms and one ^{40}K atom. Therefore the Efimov resonance occurs in collisions between ^{87}Rb atoms and ^{40}K^{87}Rb Feshbach molecules. This atom-molecule inelastic loss rate is characterized by a coefficient β, defined such that [81]

$$\dot{N}_{\rm KRb}(t) = \dot{N}_{\rm Rb}(t) = -\beta \int d^3\mathbf{r}\ n_{\rm KRb}(\mathbf{r},t)\ n_{\rm Rb}(\mathbf{r},t), \tag{7.4}$$

where $n_{\rm KRb}(\mathbf{r},t)$ is the number density of the Feshbach molecules and $n_{\rm Rb}(\mathbf{r},t)$ is the number density of the atoms.

For collisions between ^{87}Rb atoms and ^{40}K^{87}Rb Feshbach molecules, universal theory predicts that β should increase with a modest scaling of a^1 near the Fano-Feshbach resonance [35]. As with three-body recombination, this dependence is modulated by a universal sequence of Efimov

resonances [23]:

$$\beta(a) = C_\beta \frac{\sinh(2\eta_*)}{\sin^2[s_0 \ln(a/a_*)] + \sinh^2(\eta_*)} \frac{\hbar a}{m_{\mathrm{K}}}. \tag{7.5}$$

In the ^{40}K–^{87}Rb mixture, Reference [81] calculates s_0=0.6536 and $C_\beta = 10.1$.

Figure 7.5 plots Equation 7.5 for the same range of η_* values that were used in Figure 7.4. Once again, the Efimov peaks are both broad and tall, and become broader as the decay parameter η_* increases. The dashed lines indicate the range accessible to our experiments. As with the three-body recombination measurements, the Efimov theory applies when 72 $a_0 < a <$ 3000 a_0. The lower bound for β is set by the measured lifetime of molecules in a gas where all unpaired atoms have been removed. The unitarity limit sets the upper bound on β at $\beta_{\mathrm{sat}} = \hbar\pi/(\mu_{\text{Rb-KRb}}k) \approx 5 \times 10^{-10}$ cm^3/s for typical temperatures of 300 nanoKelvin [94]. Observe that the Efimov resonances in this case are likely to be saturated at their peaks, leading to a distorted shape. In Chapter 8, we will account for this effect rather crudely by fitting a multiplicative factor to the amplitude of the universal curve.

7.3 How predictable are three-atom interactions?

Looking at the predicted loss rates in Figures 7.4 and 7.5, it is clear that the locations of Efimov resonances can have a big impact on experiments that seek to leverage tunable interactions near Fano-Feshbach resonances. Fortunately, these locations turn out to be surprisingly predictable. This Section summarizes recent measurements of the relationships between Efimov resonance locations at different scattering lengths and even across different atomic species [95, 96, 97, 98, 25, 26, 99], which has driven the development of improved models for few-body interactions between atoms [100, 27, 101, 102, 103]. Since most of the work to date has been performed with homonuclear atomic gases, our measurements in Chapter 8 are motivated by the desire to extend this understanding to mixed-species systems.

Universal theory based on the Efimov effect predicts relationships between the locations of the resonances at a_-, a_+, and a_* [23, 81]. In principle, the measurement of a single Efimov resonance

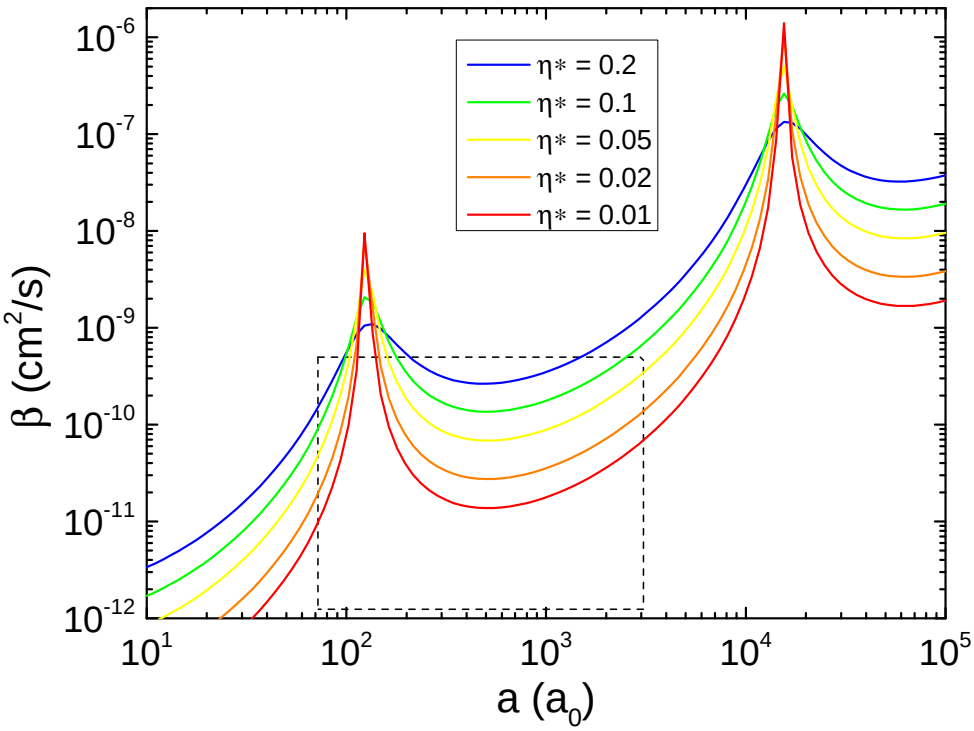

Figure 7.5: Theoretical β vs. a for ^{40}K^{87}Rb + ^{87}Rb molecule vibrational relaxation collisions from Equation 7.5. Our measurements in Chapter 8 access the range within the dashed lines.

pins down the locations for the entire Efimov spectrum in a given system. For homonuclear systems, the theoretical relationships between Efimov resonances associated with the same three-body bound state are [23]:

$$\begin{aligned} \frac{|a_-|}{a_+} &= 4.9 \\ \frac{a_+}{a_*} &= 4.46 \\ \frac{|a_-|}{a_*} &= 21.9 \end{aligned} \tag{7.6}$$

The first relation, between a_- and a_+, has been confirmed by a number of experiments [22, 97, 104]. In contrast, the values for a_* reported thus far [105, 106, 107] have not followed the predicted locations relative to a_+ and a_-. This suggests that models of the atom-molecule loss resonances in cold atoms may require additional input beyond the Efimov effect [103].

More generally, the Efimov relationships between resonance locations are a function of the mass ratio and the number of resonant interactions. For our heteronuclear mixture of ^{40}K and ^{87}Rb atoms, they are [81]:

$$\begin{aligned} \frac{|a_-|}{a_+} &= 11.1 \\ \frac{a_+}{a_*} &= 21.7 \\ \frac{|a_-|}{a_*} &= \frac{122.7}{0.51} = 240.6 \end{aligned} \tag{7.7}$$

These relationships have been imposed between the resonances in Figures 7.4 and 7.5.

Whereas Efimov theory predicts a relationship between resonance locations, the so-called 'three-body parameter' that sets the absolute resonance locations was initially understood to be a non-universal quantity subject to each system's unique interaction potential at short range [108, 23, 109]. However, as measurements of Efimov resonances accumulated in single-species cold atom experiments, an unexpected pattern emerged: Efimov loss resonances were consistently measured at

$$a_{-,\text{universal}} = -9.1\ r_{\text{vdW}} \tag{7.8}$$

for different nuclear spin states [25], different Fano-Feshbach resonances [26], and even different atomic species [95, 96, 97, 98, 25, 26, 99].

Figure 7.6 collects worldwide measurements of Efimov resonance locations in single-species cold atom experiments[2] , where each point represents a measured Efimov resonance, following the format of Reference [26]. Each vertical axis compares the measured Efimov resonance location to a 'universal value' by combining Equation 7.8 with the universal relationships in Equations 7.6. For each plot, the full span of the vertical axis represents a period of the Efimov spectrum, where a varies by $\lambda = 22.7$.

If the three-body parameter were determined by a detailed interplay between non-universal short-ranged potentials, as was originally expected from the Efimov theory, then the points in Figure 7.6 would be scattered over the whole vertical range of the plots. Instead, the points in subfigures (a) and (b) tightly cluster around a simple prediction based on only the van der Waals length (Equation 7.8, dashed horizontal line), which implies that the three-body parameter is universal. The points in subfigure (c), on the other hand, appear to depart from that pattern. The pink circle points are measured by the types of atom-molecule loss resonances shown in Equation 7.5 and Figure 7.5. Since they are measured in the same systems where a_- follows the universal three-body parameter, it seems likely that Equation 7.6 misses some important aspect of the way atoms and molecules collide. The blue diamond points represent 'avalanche peaks,' which are small atom loss resonances that appear near the universal a_* location in several experiments [97, 98, 112]. The mechanism by which atom loss occurs near a_* in a gas of pure atoms remains poorly understood at the time of this writing [113].

The unexpected pattern shown in Figure 7.6(a) stimulated theoretical research, which has since shown that the van der Waals potentials of cold atoms screen out the details of the non-universal short-ranged potentials [114, 100, 27, 101, 102]. This leads to the universal three-body parameter in ultra cold atoms. Measurements in the three-body recombination rate for ultra cold

[2] One data point measuring a non-universal value of a_- for ^{39}K in Ref. [97] is deliberately excluded because a later publication by the same group [110] claimed that the measurement was not repeatable.

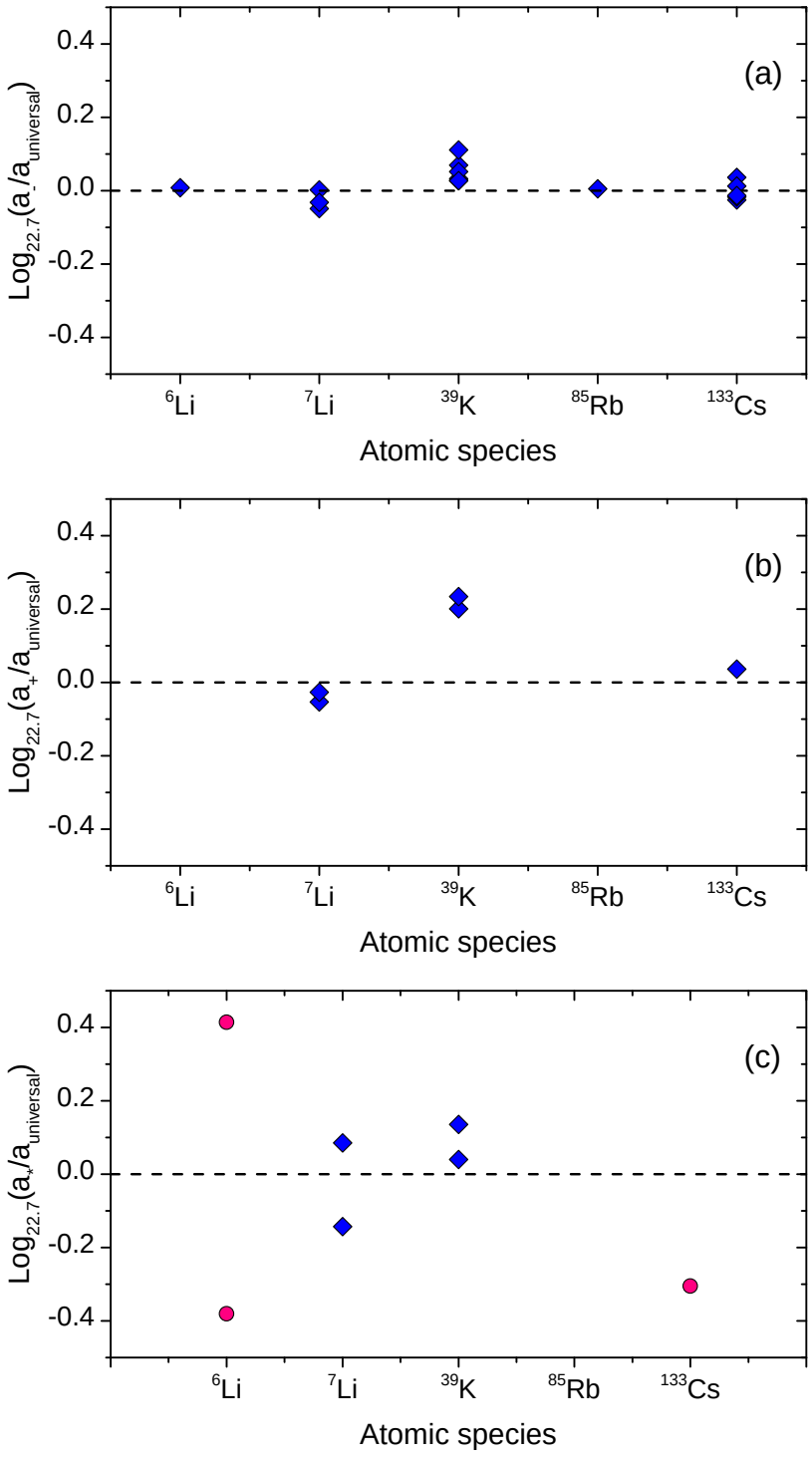

Figure 7.6: Measurements of the three-body parameter in homonuclear systems by three-body recombination (blue diamonds) and atom-molecule loss (pink circles). Each subplot corresponds to a different type of Efimov resonance: subplot (a) shows measurements of a_- [111, 98, 104, 25, 97, 99, 22, 26, 79, 110]; subplot (b) shows measurements of a_+ [104, 25, 97, 22]; and subplot (c) shows measurements of a_* [105, 97, 98, 106, 112]. The horizontal dashed lines show a prediction based on a three-body parameter that is universally determined by the van der Waals length.

$^4He^*$ have also been consistent with the same universal three-body parameter [115]. More recently, a different universal model based on the van der Waals potential [103] was able to explain the locations of both a_- and a_* for ^{133}Cs, including the deviation of their relationship from the simple Efimov rules in Equation 7.6.

For homonuclear cold atom systems, a combination of universal models based on Efimov physics and a large number of experimental measurements have driven the development of a detailed quantitative understudying of three-body interactions. In contrast, only a handful of measurements exist for mixed-species systems. The first was performed by the LENS group in a Bose–Bose mixture of ^{41}K and ^{87}Rb atoms with resonant interspecies interactions [92]. They identified loss resonances corresponding to $a_- = -246\ a_0$ and a tentatively labelled avalanche peak at $a_* = 667\ a_0$ in the ^{41}K–^{87}Rb–^{87}Rb system. One theory has predicted a universal three-body parameter for heteronuclear mixtures, which would imply that LENS's ^{41}K–^{87}Rb–^{87}Rb system and our ^{40}K–^{87}Rb–^{87}Rb system have nearly identical Efimov resonance locations [116]. The resonance locations in Figures 7.4 and 7.5 are based on LENS's measurement of a_-. These figures show that multiple Efimov features would appear within our experimental window, if the two K–Rb mixtures had identical three-body parameters. Our measurements presented in Chapter 8 investigate this possibility. After our measurements were published, two independent groups measured Efimov loss resonances in mixtures of ^{6}Li and ^{133}Cs atoms [82, 83]. They demonstrated a high density of Efimov states consistent with the predicted value of $\lambda = 4.9$, which made it possible to observe three consecutive Efimov states for the first time in any experiment. This illustrates the rich behavior of few-body interactions in quantum gas mixtures.

Chapter 8

K-Rb-Rb collisions

In this Chapter, I describe our measurements of inelastic collision rates as a function of the interspecies scattering length, and then discuss our results in the context of the universal Efimov effect. Similar measurements for atoms with the same mass have uncovered a wealth of insights into few-body interactions. Extending this understanding to include mixtures of different atomic species is important to build a more general picture. To that end, we search for evidence of ^{40}K–^{87}Rb–^{87}Rb three-body states and compare our findings with theoretical predictions [116] as well as with past measurements of the isotopically different ^{41}K–^{87}Rb–^{87}Rb mixture by the LENS group [92]. Section 8.1 presents our measurement of an Efimov resonance in the collisions between ^{40}K^{87}Rb Feshbach molecules and ^{87}Rb atoms. In Section 8.2, we present measurements of the three-body recombination rate coefficient α over the entire range of interspecies scattering lengths available to our experiments, and find that the data exclude the presence of Efimov resonances in that range. Finally, in Section 8.3 we analyze these findings in terms of a predicted universality of the three-body parameter that sets the Efimov resonance locations.

The bulk of the material in this Chapter is published in Reference [117]. In particular, Sections 8.2 and 8.1 are published nearly verbatim in that work. Section 8.3 also contains material from the paper, but it is expanded to include comparisons against newer results from other groups.

8.1 Atom-molecule loss

I'll begin by considering inelastic atom-molecule collisions, which eject the participating atom and Feshbach molecule from the trap. The inelastic collision rate is enhanced when a is tuned to a value, denoted a_*, where an Efimov trimer state is degenerate with the atom-molecule threshold [93, 23]. Such Efimov resonances have been observed as broad loss features for ^{133}Cs [105] and ^{6}Li dimers [106, 107] (see Figure 7.5 and the accompanying discussion in Section 7.2 for more on these resonances). Part of our motivation to study atom-molecule collisions in the ^{40}K–^{87}Rb mixture came from previous measurements of the same mixture that were made by our group in 2008 [71]. They found that collisions between ^{87}Rb atoms and ^{40}K^{87}Rb molecules intensified as they reduced the scattering length, which ran opposite to the expected trend [35]. Helfrich *et al.* later suggested that these experiments had encountered one side of an Efimov resonance [81]. Our new measurements, which are the topic of this Section, extend these data to lower values of a where we do in fact observe an atom-molecule resonance, which is the first one to be measured in a heteronuclear mixture.

We map out the molecule loss rates for three different collision partners: ^{87}Rb atoms in the $|1,1\rangle$ state, ^{40}K atoms in the $|9/2,-9/2\rangle$ state, and ^{40}K atoms in the $|9/2,-7/2\rangle$ state. Efimov resonances are only possible for the first case, and, in the last case, the collision partner does not participate in the Fano-Feshbach resonance. For these measurements, the atom gas mixture was typically prepared at $a = -300\ a_0$ and $T = 300$ nK. We measured ^{87}Rb–^{40}K^{87}Rb collisions in the single-beam optical dipole trap, whereas ^{40}K–^{40}K^{87}Rb collisions were measured with an additional confining laser beam that increases the ^{40}K axial trap frequency. For data in this Chapter, the ^{40}K atoms are at $T/T_{\mathrm{F}} > 0.2$ and the ^{87}Rb are at $T/T_{\mathrm{c}} > 1.1$.

Figure 8.1 shows a timing diagram and an example of raw data from a ^{87}Rb–^{40}K^{87}Rb loss measurement. First, the magnetic field is slowly swept across the Fano-Feshbach resonance at a rate of 3 G/ms to form ^{40}K^{87}Rb Feshbach molecules by magnetoassociation, following the procedures discussed in Chapter 5. To prepare a pure sample of molecules and one particular atom species, we then hold the magnetic field at 545 G while we use a combination of resonant light and RF

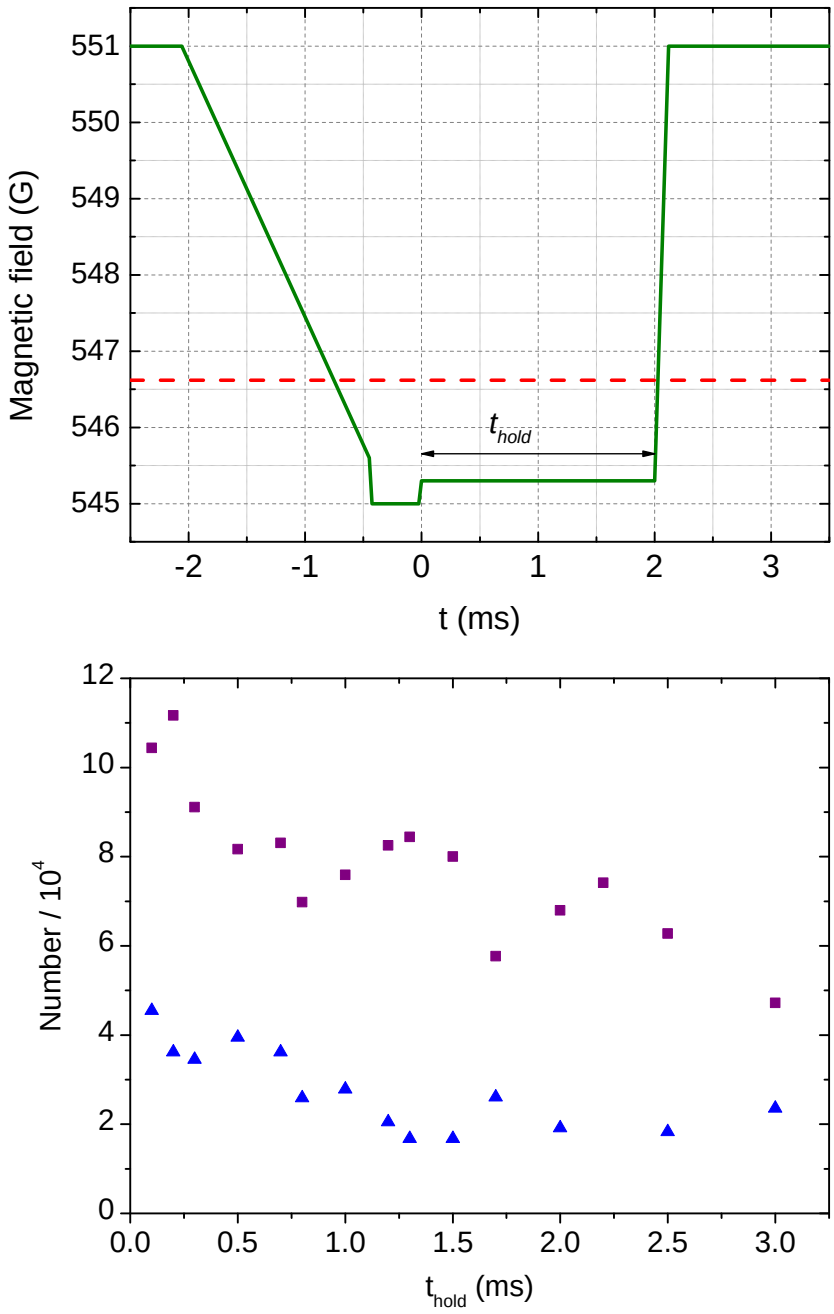

Figure 8.1: Top: Magnetic-field sequence for molecule production and loss measurements (green solid line). The red dashed line marks the interspecies Fano-Feshbach resonance. Bottom: Loss in a gas of ^{87}Rb atoms and ^{40}K^{87}Rb molecules. Blue triangles show the number of ^{40}K atoms which were bound as ^{40}K^{87}Rb molecules during t_{hold}. Purple squares show ^{87}Rb atoms, including those that were free and those that were bound into ^{40}K^{87}Rb molecules.

pulses to selectively remove unpaired atoms from the trap. When measuring collisions with ^{40}K atoms in the $|9/2, -7/2\rangle$ state, we use RF transfer the unpaired ^{40}K atoms into the $|9/2, -7/2\rangle$ hyperfine state at this point. After preparing the atom-molecule sample, we ramp the field up to the the value desired for the loss measurement, wait a variable hold time $t_{\rm hold}$, turn off the optical trap, and then jump the magnetic field back across the Fano-Feshbach resonance to dissociate the molecules. We extract the number of molecules, the number of free atoms, and the in-trap cloud sizes from images of the resulting atom clouds after a few milliseconds of expansion from the trap. In-trap radial sizes are calculated from the measured axial size and the trap aspect ratio.

From the Rb+KRb data, we extract the loss-rate coefficient β by fitting the measured loss of atoms and molecules to numerical solutions of Eqs. (8.1), which are reproduced here:

$$\dot{N}_{\rm KRb}(t) = \dot{N}_{\rm A}(t) = -\beta \int d^3\mathbf{r}\ n_{\rm KRb}(\mathbf{r}, t)\ n_{\rm A}(\mathbf{r}, t), \tag{8.1}$$

where $n_{\rm KRb}(\mathbf{r}, t)$ is the number density of the Feshbach molecules and $n_{\rm A}(\mathbf{r}, t)$ is the number density of the atoms. We account for heating by including the measured cloud sizes at each point in time. The estimated systematic uncertainty in β, which is dominated by the uncertainty in the in-trap densities, is $\pm 20\%$. For our measurements of collisions between ^{40}K atoms and ^{40}K^{87}Rb molecules, the depletion and heating of the much larger atom cloud are negligible during the loss measurement and Eq. (8.1) has the analytic solution $N_{\rm KRb}(t) = N_{\rm KRb}(0)e^{-t/\tau}$ where $1/\tau = \langle n_{\rm K}\rangle\beta$, and $\langle n_{\rm K}\rangle$ is the density-weighted atom density. The loss rate coefficient β for K–KRb collisions is extracted by fitting the molecule number to an exponential decay as a function of time, with τ and the initial molecule number as free parameters. This method give results that are consistent with more detailed calculations like the ones we use for Rb+KRb collisions.

Figure 8.2 plots the measured β vs. a. The rate of molecule collisions with ^{40}K in either hyperfine state decreases smoothly with increasing a, as was seen previously [71]. In contrast, for collisions between ^{40}K^{87}Rb molecules and ^{87}Rb atoms, we observe a prominent resonance whose location lies beyond the range of previous data [71] and is consistent with the suggestion of $a_* = 200(50)\ a_0$ made by Ref. [81]. The solid line in Fig. 8.2 shows a fit to the universal formula for

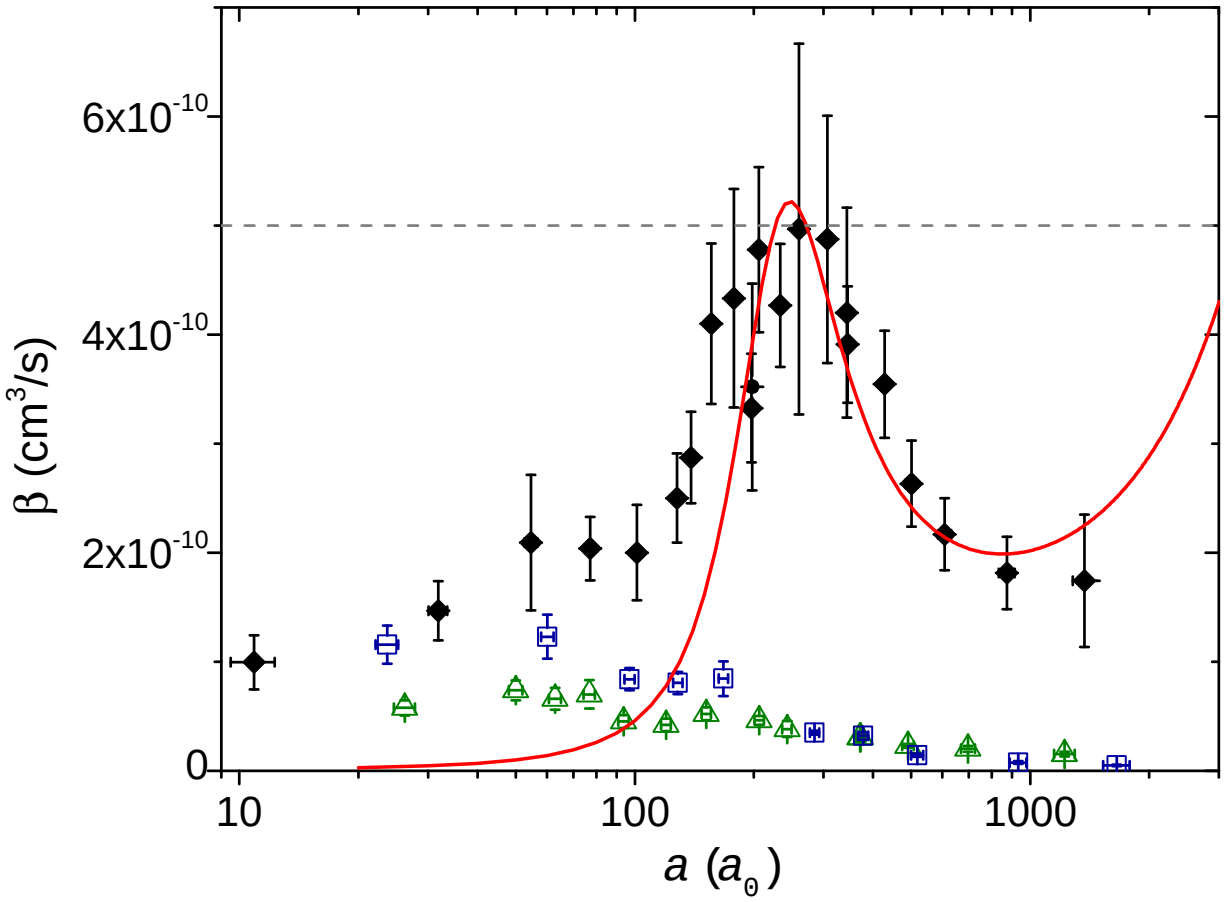

Figure 8.2: Measured β vs. a for collisions of ^{40}K^{87}Rb molecules with ^{40}K atoms in the $|9/2, -7/2\rangle$ state (triangles), with ^{40}K atoms in the $|9/2, -9/2\rangle$ state (squares), and with ^{87}Rb atoms in the $|1, 1\rangle$ state (solid diamonds). Vertical error bars indicate one standard deviation of statistical error, and horizontal error bars correspond to an upper bound of ± 0.02 G variation in B across the cloud. A broad resonance is evident in the ^{87}Rb+^{40}K^{87}Rb loss and the solid curve shows a fit to the universal $T = 0$ shape for an Efimov resonance Eq. (7.5). The horizontal dashed line indicates the estimated unitarity-limited β for the collisions between ^{87}Rb atoms and ^{40}K^{87}Rb molecules. This data was published in Reference [117].

an Efimov resonance, Equation 7.5, which gives a resonance location $a_* = 230(10)\ a_0$, a resonance width set by $\eta* = 0.26(3)$, and a resonance amplitude $C_\beta = 3.2(2)$. Here, we exclude data at $a < 2r_{\mathrm{vdW}} = 144\ a_0$ from the fit because the non-universal short ranged interaction potential between the atoms has a strong influence in this range [18]. Whereas the values of a_* and η_* are functions of the particular interaction potentials of ^{40}K and ^{87}Rb atoms, the value of C_β has been predicted to equal 10.1 based on universal theory [81]. The discrepancy between theory and our measured value of C_β could be due to saturation at finite temperature: the horizontal dashed line indicates the unitarity-limited value for β, which is $\beta_{\mathrm{sat}} = \hbar\pi/(\mu_{\text{Rb-KRb}}k) \approx 5 \times 10^{-10}$ cm^3/s at 300 nanoKelvin [94]. This value is close to much of our data near the resonance center. It would be interesting to calculate the saturation effect more accurately by averaging over the thermal distribution of collision energies [87], or to repeat these measurements on a gas at an even lower temperature. However, recent measurements of similar resonances in ^{133}Cs also find a non-universal value for the amplitude C_β, which suggests that a more detailed theoretical approach is generally required for atom-molecule Efimov resonances [118].

8.2 Three-body recombination

Now we turn our attention to three-body recombination, which is widely used to reveal Efimov physics in cold atoms. Three atoms can collide inelastically and form a diatomic molecule, which typically releases enough energy to eject all three atoms from the trap. This process is resonantly enhanced when an Efimov trimer state approaches zero binding energy at a negative a denoted a_-. On the other side of the Fano-Feshbach resonance, interference effects lead to minima in the three-body rate coefficient α at a positive a denoted a_+. These features modulate an overall a^4 dependence of α that results in a large increase of atom loss rates near a Fano-Feshbach resonance [119, 23]. Figure 7.4 and the accompanying discussion in Section 7.2 give more details on these resonances.

In the only previous observation of heteronuclear Efimov resonances, enhanced loss for ^{41}K–^{87}Rb–^{87}Rb was observed at $a_- = -246(14)a_0$ [92]. An additional narrow loss feature at 667(1) a_0

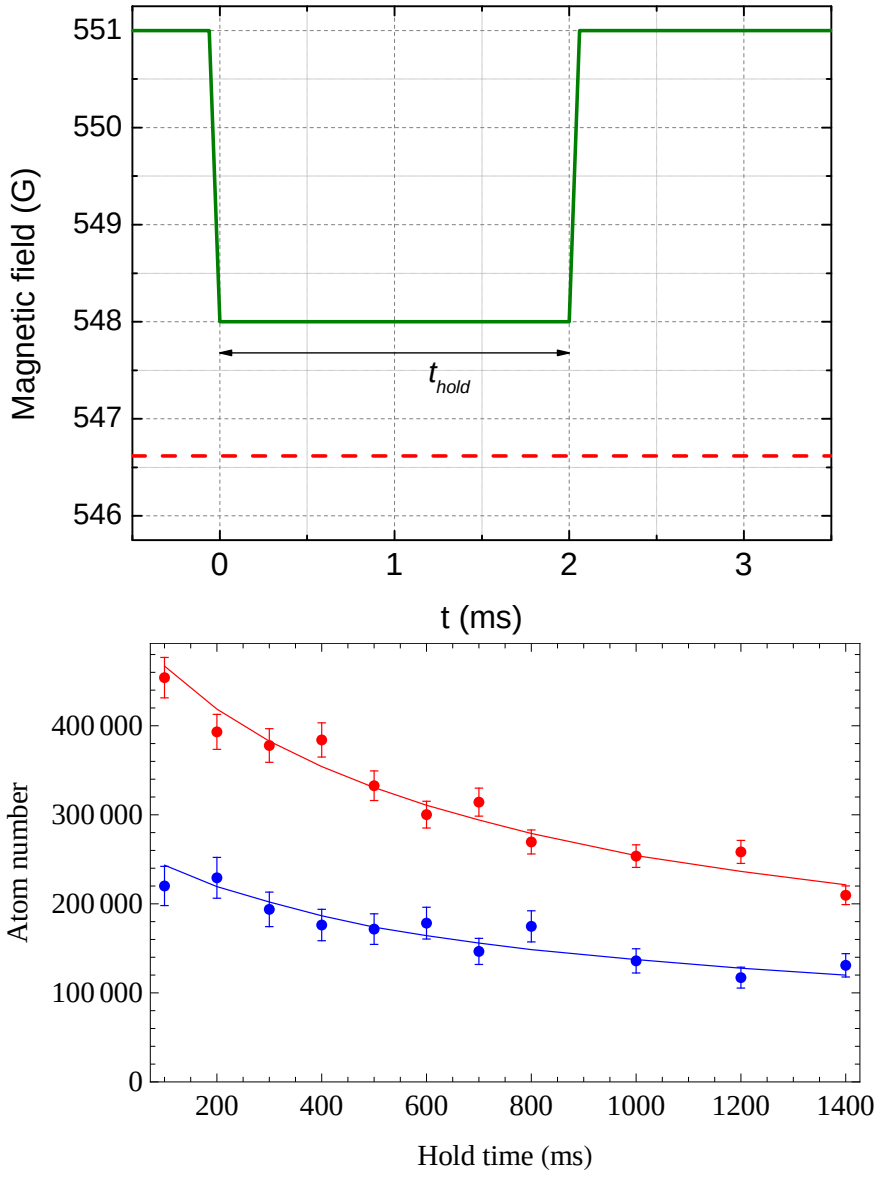

Figure 8.3: Top: An example timing diagram for a measurement of the three-body recombination rate coefficient α at $B = 548$ G. Bottom: The measured number of Rb atoms (red points) and K atoms (blue points) vs t_{hold}. Solid lines show the result of the fit used to obtain α following Reference [120].

indicated a possible atom-molecule resonance. We were interested in testing whether matching features existed in our ^{40}K–^{87}Rb–^{87}Rb system. After the three-body parameter that sets Efimov resonance locations was found to be universal in homonuclear systems, Wang *et al.* predicted a similar pattern for heteronuclear systems [116]. Since the two K–Rb mixtures have the same interspecies van der Waals length and non-resonant Rb-Rb scattering length, as well as nearly identical mass ratios, a universal three-body parameter would result in Efimov resonances at the same interspecies scattering lengths. Previous measurements of α for a ^{40}K–^{87}Rb mixture saw no features beyond a^4 scaling; however, the data were relatively sparse [71] and it had been hypothesized that an Efimov resonance could have fit between the points [81]. This Section presents additional, more detailed, measurements of α for ^{40}K–^{87}Rb that cover values of a where the ^{41}K–^{87}Rb features were seen.

For these measurements, the atom gas mixture is prepared by evaporating at a field where $|a| \approx 300\ a_0$ on the same side of the Fano-Feshbach resonance as the field for the loss measurement, B. Figure 8.3 shows a timing diagram and an example of raw atom loss data. Once the gas is prepared, the field is then swept to B in a short time compared to the loss, and held for a variable time t_{hold}. Finally, the optical trap is turned off and the field is swept back to the evaporation value where the atoms are imaged. From our measured cloud sizes and atom numbers, we obtain α which is defined by

$$\dot{N}_{\mathrm{Rb}}(t) = 2\dot{N}_{\mathrm{K}}(t) = -2\alpha \int d^3\mathbf{r}\ n_{\mathrm{K}}(\mathbf{r},t)\ n_{\mathrm{Rb}}^2(\mathbf{r},t). \tag{8.2}$$

We employ an analysis similar to that described in Ref. [120], which uses the measured atom densities at each time to account for heating of the gas. Whereas Ref. [120] used quantum degenerate gases, we adapt the analysis to the Maxwell-Boltzmann density distributions that describe our atom clouds. As a check of this analysis, we compare the results against a brute-force numerical solution of the differential equations, which calculates heating rates from anti-evaporation of Rb atoms rather than taking measured cloud sizes as a given input. We find the results to be consistent for both methods, although the former method involves less computational overhead. Based on our

ability to accurately extract the in-trap density of the atoms from expanded images, we estimate the systematic uncertainty in α to be $\pm 20\%$.

Figure 8.4 shows the measured α vs. B. We measure an increase of α by over four orders of magnitude near the s-wave resonance at $B_0 = 546.618$ G. A second peak, on the order of 0.1 G wide, is evident near 547.4 G. As illustrated in the inset to Fig. 8.4, this feature is not consistent with the expected shape of an Efimov resonance, and we identify it as a two-body d-wave Fano-Feshbach resonance [46, 121]. Because it is technically challenging to control a near a narrow resonance, we exclude the data for B between 547.25 G and 547.50 G from further analysis and calculate a using Equation 2.1 for the s-wave resonance alone. Namely, we set $a = -187a_0(1+3.04G/(B-546.618G))$ following Reference [122].

Figure 8.5 shows the measured α vs. a, using the same data presented in Figure 8.4. These data are consistent with the more sparse measurements of Ref. [71]. For comparison, we also plot the universal form for α as a function of a [81] with Efimov resonances corresponding to the measurement of a_- by the LENS group [92]. These functions are given in Equations 7.2 and 7.3, and the location for the interference minimum at a_+ is extrapolated from the value of a_- using Equation 7.7. We use $\eta* = 0.02$ for the plotted curves, which gives the best agreement to the measured magnitude of α. The calculated shapes for Efimov features at this value of η_* (orange solid lines) are extremely large compared to any gaps or uncertainty in our data over the measured range. We conclude that there are no Efimov features in α at negative a between -200 a_0 and -3000 a_0 or at positive a between 200 a_0 and 3000 a_0.

We also used these data sets to measure the ratio of ^{87}Rb loss to ^{40}K loss. Within the uncertainties, this ratio does not show a dependence on a and the average value is 2.1(1), which is consistent with ^{87}Rb+^{87}Rb+^{40}K three-body recombination being the dominant loss process. A resonance feature with a different multistage process has also been proposed, in which three-body recombination generates an energetic ^{40}K^{87}Rb Feshbach molecule that undergoes subsequent resonant elastic collisions with ^{87}Rb atoms, eventually ejecting multiple ^{87}Rb atoms from the trap. This so-called 'avalanche mechanism' loss has been hypothesized to exist near atom-molecule Efimov res-

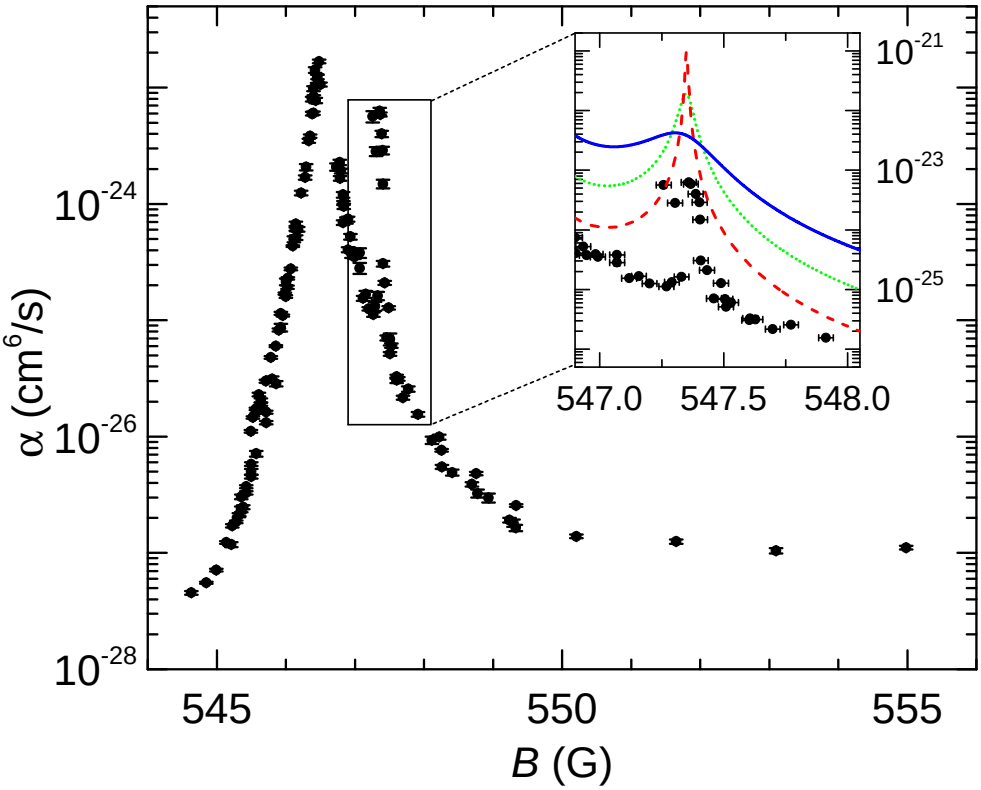

Figure 8.4: α vs B. There are two clear peaks near 546.6 G and 547.4 G: The first is the s-wave Fano-Feshbach resonance that we use to control a, and the second, much narrower feature we attribute to a d-wave interspecies Fano-Feshbach resonance. Vertical error bars show the statistical uncertainty in α, and horizontal error bars show an upper bound of ± 0.03 G for the variation in B during the measurement. Inset: α vs. B near the feature at 547.4 G. The solid, dotted, and dashed lines show the universal shape of an Efimov resonance, Eqs. (7.2) and (7.3), for $\eta* = 0.1$, $\eta* = 0.02$, and $\eta* = 0.004$. This data was published in Reference [117].

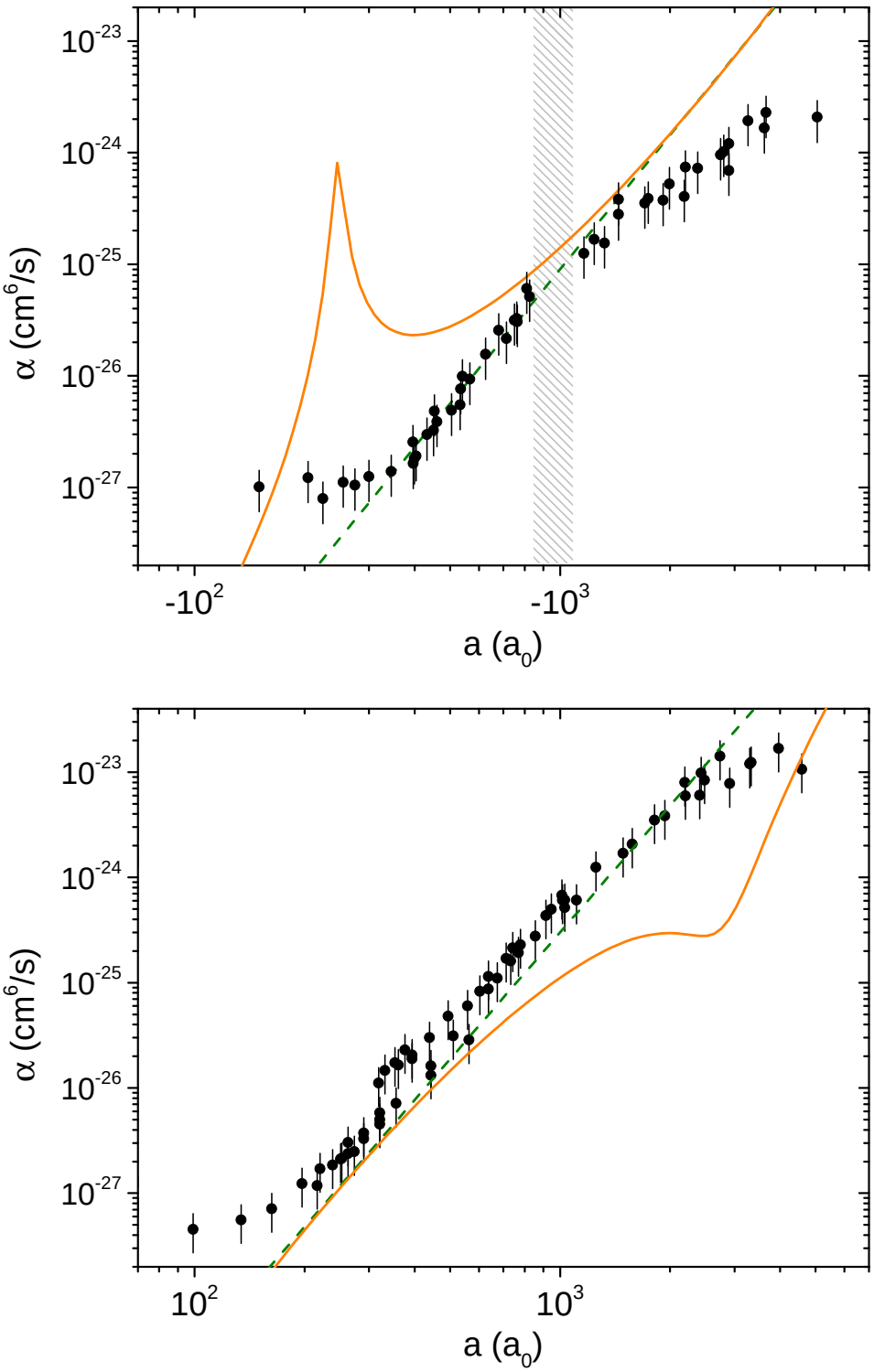

Figure 8.5: α vs. a for $a < 0$ (upper panel) and $a > 0$ (lower panel). The dashed green lines show an a^4 dependence with no Efimov resonances. The solid orange lines show Equations 7.2 and 7.2 for the three-body parameter that was measured in ^{41}K–^{87}Rb–^{87}Rb by the LENS group [92]. A narrow two-body Fano-Feshbach resonance blocks experimental access to the range $-1090 \leq a/a_0 \leq -840$, which is indicated by the shaded region on the upper plot. This data was published in Reference [117].

Table 8.1: Comparison of K–Rb–Rb Efimov resonances to universal theory. The 'Three-body parameter' column lists measurements or predictions of Efimov resonance locations. The a_-/a_0, a_+/a_0, and a_*/a_0 columns use Equation 7.7 to calculate the universal locations of ^{40}K–^{87}Rb–^{87}Rb Efimov resonances corresponding to the same Efimov bound state described in the first column. In order to show potential resonances associated with other Efimov bound states, some rows are scaled by factors of $\lambda = e^{\pi/s_0}$.

Three-body parameter	Source	a_-/a_0	a_+/a_0	a_*/a_0
$a_* = 230\ a_0$	^{40}K+^{87}Rb Experiment [117]	-55000	5100	230
$a_* = 230\ a_0/\lambda$	^{40}K+^{87}Rb Experiment [117]	-450	41	1.9
$a_+ = 2800\ a_0$	Universal 3BP Theory [116]	-30000	2800	130
$a_+ = 2800\ a_0/\lambda$	Universal 3BP Theory [116]	-250	23	1.1
$a_- = -246\ a_0$	^{41}K+^{87}Rb Experiment [92]	-246	22	1.0
$a_- = -\lambda \times 246 a_0$	^{41}K+^{87}Rb Experiment [92]	-30000	2700	130
$a_* = 667\ a_0$	^{41}K+^{87}Rb Experiment [92]	-160000	14000	667
$a_* = 667\ a_0/\lambda$	^{41}K+^{87}Rb Experiment [92]	-1300	120	5.4

onances like ours in Figure 8.2, where elastic atom-molecule collisions are also enhanced [97]. Such a peak was tentatively identified by the LENS data in the ^{41}K–^{87}Rb–^{87}Rb system [92]. However, our data show no sign of such a narrow loss resonance or of any increase in the ratio of lost ^{87}Rb atoms to lost ^{40}K atoms near $a_* = 230\ a_0$. We have since made more detailed followup measurements to search for even narrower resonances, but we still find no evidence for avalanche collisions in either the atom loss rate or the ratio of lost ^{87}Rb atoms to lost ^{40}K atoms [123].

8.3 Comparison to other experiments

Armed with the measurements in Figures 8.2 and 8.5, what can we now conclude? In this Section we examine the data in the context of universal Efimov theory as well as predictions based on the universality of the three-body parameter. Table 8.1 lists measurements and predictions of K-Rb-Rb Efimov resonance locations. The relationships between different resonance locations from universal Efimov theory, which are listed in Equation 7.7, are used to calculate corresponding values of a_-/a_0, a_+/a_0, and a_*/a_0 where resonances would hypothetically be observable in our data. Due to the large scaling factor, $\lambda = 122.7$, many of these predicted resonances are outside of our measurement range and therefore not testable in our current experiments.

First, we check the self-consistency of our own measurements. Given our observed resonance at $a_* = 230(30)\ a_0$ (Figure 8.2), universal relations predict $a_+ = 5100\ a_0$ and $a_- = -55,000\ a_0$ which are outside of our measurement range. The absence of an Efimov resonance in Figure 8.5 is therefore consistent with universal theory. However, if there were to exist a more deeply bound Efimov state, then scaling by $\lambda = 122.7$ would give $a_+ = 41\ a_0$ and $a_- = -450\ a_0$. The latter feature in α is clearly excluded by our measurements. This suggests that the observed resonance at $a_* = 230\ a_0$ belongs to the most deeply bound Efimov state in our system. However, it is worth noting that the ratio of $|a_-|$ and a_* measurements have not always agreed with universal Efimov theory [105, 111, 106, 26].

Next, we compare our results for ^{40}K–^{87}Rb to the previous measurements for ^{41}K–^{87}Rb. The two mixtures share the same isotope of Rb, they both have resonant interspecies interactions with $r_{\mathrm{vdW}} = 72\ a_0$ [18, 124], and their mass ratios differ by only a few percent. If the three-body parameter is universally determined by the two-body potential, one would expect ^{41}K–^{87}Rb and ^{40}K–^{87}Rb mixtures to have the same Efimov resonance locations [116]. However, our measurements exclude a_- near -246 a_0, where the ^{41}K–^{87}Rb–^{87}Rb Efimov resonance was observed. The ^{41}K–^{87}Rb work also identified a feature in α at 667(1) a_0 as a possible atom-molecule resonance [92]. For the ^{40}K–^{87}Rb mixture, we find $a_* = 230(30)\ a_0$ with direct measurements of atom-molecule loss and we do not observe a corresponding feature in α.

Wang *et al.* predict a universal three-body parameter for heteronuclear mixtures, and specifically predict the locations of K–Rb–Rb Efimov resonances to be $a_+ = 2800\ a_0$ and $a_- < -30000\ a_0$ [116]. The corresponding atom-molecule loss feature would be at $a_* = 130\ a_0$. Our measurements of α exclude $a_+ = 2800\ a_0$ and we find $a_* = 230(30)\ a_0$ from atom-molecule loss; both results suggest that the value of a_+ is slightly higher than the prediction. Intriguingly, the LENS group's measurement of $a_- = -246\ a_0$ in the ^{41}K–^{87}Rb mixture is consistent with the presence of a more deeply bound Efimov state whose location is related to Wang *et al.*'s predictions by the universal scaling factor λ. Furthermore, recent measurements of Efimov resonances in ^{6}Li-^{133}Cs mixtures by two different groups have also been similar to the predictions by Wang *et al.* [82, 83]. In these mea-

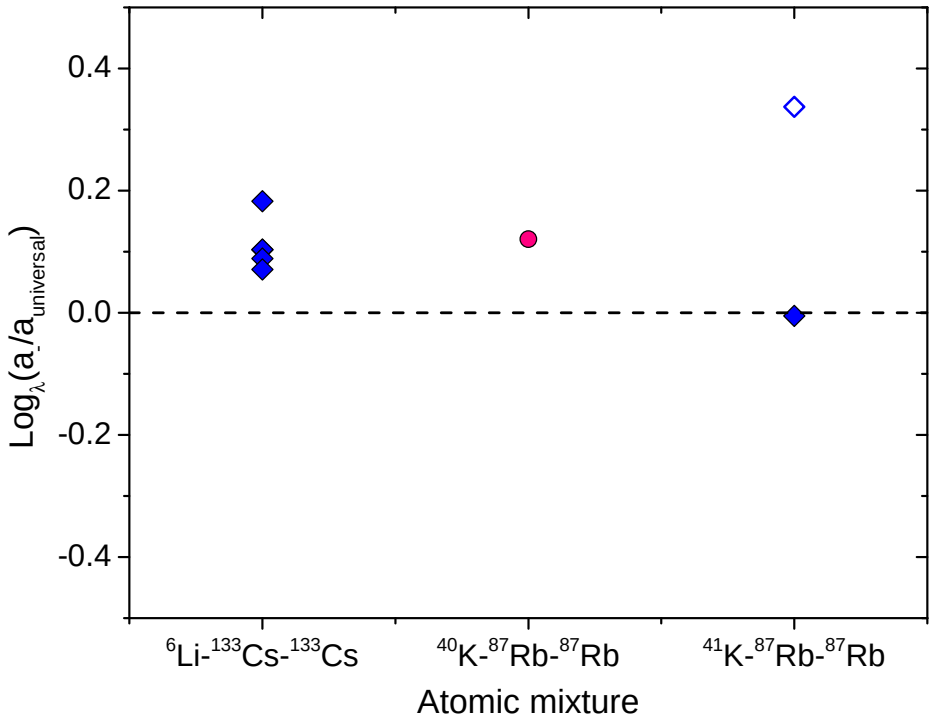

Figure 8.6: Measured three-body parameters in heteronuclear mixtures (points) compared against a theoretical universal three-body parameter for heteronuclear systems (dashed line) [116]. Individual measurements have been rescaled by multiples of $\lambda = e^{\pi/s_0}$ to facilitate a comparison of multiple Efimov states. Solid blue diamonds show measurements of a_- via three-body recombination [92, 82, 83], the solid pink circle shows a value of a_- that would correspond to our measurement of a_* from Figure 8.2, and the empty blue diamond shows a tentative assignment of a_- that would correspond to an 'avalanche' atom loss feature [92].

surements, the Efimov series also included a state that was more deeply bound than the theoretical prediction. Figure 8.6 summarizes these comparisons.

Overall, we do not find clear evidence for a universal three-body parameter. However, given the large Efimov scaling factor (122.7), the observed differences are relatively small. In addition, the clearest features seen for both K–Rb mixtures occur at scattering lengths that are only a few times larger than r_{vdW}, where non-universal finite-range effects can play a role [125, 126, 127]. This role may be greater for ^{40}K–^{87}Rb, where the Fano-Feshbach resonance has an intermediate strength parameterized by $s_{\mathrm{res}} = 2.0$, compared to the strong ^{41}K–^{87}Rb resonance with $s_{\mathrm{res}} = 26$ [18]. On the other hand, a universal three-body parameter has been observed in homonuclear ^{7}Li atoms [25] at Fano-Feshbach resonances with $s_{\mathrm{res}} = 0.9$ and in ^{39}K atoms with s_{res} as low as 0.1 [110]. An interesting question is whether the strength of the Fano-Feshbach resonance has more influence on the locations of Efimov features in heteronuclear systems.

Chapter 9

Concluding remarks

9.1 Summary

In this Thesis, I explored few-body interactions in an ultra cold mixture of ^{87}Rb and ^{40}K atoms. I began by demonstrating a magnetic trapping system for the atoms that can also provide a stable, uniform magnetic field to improve our control over the atoms' interactions near a magnetic Fano-Feshbach resonance. Our experiments rely on this resonance to access universal phenomena where the interspecies interactions are strong.

Chapter 5 studied the conversion of atoms to fermionic Feshbach molecules using magnetic sweeps. By combining a degenerate Fermi gas of ^{40}K atoms with a thermal Bose gas of minority ^{87}Rb atoms, we are able to pair as much as 45 percent of the ^{87}Rb atoms into ^{40}K^{87}Rb molecules. However, we still measure significantly fewer molecules than would be expected from a model that has successfully described bosonic molecule formation in Bose or Fermi gases. Based on this discrepancy, it seems likely that the Fermi statistics of the ^{40}K–^{87}Rb molecules exerts a strong influence on the pairing process. In Chapter 6 we found that the kinetic energy of these molecules corresponds to a temperature that is about 1.5 times larger than that of the atoms. Together, the surprisingly low number and high temperature of the molecules prevent the formation of a degenerate Fermi gas of Feshbach molecules in our experiments.

In Chapters 7 and 8, we measured the rates of three-body collisions in the ^{40}K–^{87}Rb gas mixture as a function of the interspecies scattering length. These measurements reveal a resonance in the collisions between ^{87}Rb atoms and ^{40}K^{87}Rb molecules that is connected to the universal

Efimov series of three-body bound states. We also measure a notable absence of features in the atom loss rate, in defiance of some theoretical predictions. In combination with a growing number of measurements in diverse heteronuclear systems, these results will hopefully lead to a more quantitative understanding of three-body collisions between cold atoms. In the meantime, three-body interactions are now more thoroughly characterized in the popular ^{40}K–^{87}Rb mixture.

9.2 Looking forward

The range of useful scattering lengths for our experiments is presently limited by the density and temperature of the atom samples. In part, the minimum temperature and density are limited by the fact that our method of supporting the atoms against the pull of gravity also has the effect of compressing the gas. It would be possible to achieve lower atom temperatures and densities on an apparatus in low-Earth orbit, which would open the door to quantum physics experiments at extremely high scattering lengths. The Cold Atom Laboratory project at the Jet Propulsion Laboratory is scheduled to launch an experimental apparatus that creates ultra cold samples of ^{40}K and ^{87}Rb atoms on the International Space Station in 2016. This will be an exciting development for our field.

For those of us who are trapped down here on Earth, there are still plenty of experiments within reach of terrestrial ^{40}K–^{87}Rb experiments. In terms of few-body physics, there is another Fano-Feshbach resonance that overlaps the one that we used for the experiments in this thesis, and couples to the same K Zeeman state but to a different Rb Zeeman state [124]. A spin mixture of ^{87}Rb atoms with a polarized gas of ^{40}K atoms could have two different resonantly enhanced interspecies scattering lengths, which is a situation where interesting few-body phenomena have been predicted [109]. On the other hand, we could push our experiments to colder temperatures and study many-body effects in fully quantum-degenerate gases. One particularly exciting new development in our lab has been the implementation of a so-called 'painted' optical potential, which rapidly modulates the position of an optical trap beam to create a time-averaged potential. This can create a larger, more harmonic, potential than the optical traps that were used in this

thesis. This flexible potential, whose shape can be changed dynamically during an experiment, sets the stage for a variety of exciting measurements of many-body physics.

Bibliography

[1] N. Bohr. I. On the constitution of atoms and molecules. Philosophical Magazine, 26, 1913.

[2] William D. Phillips. Nobel lecture: Laser cooling and trapping of neutral atoms. Rev. Mod. Phys., 70:721–741, Jul 1998.

[3] H. J. Metcalf and P. van der Straten. Laser Cooling and Trapping. Springer, 1999.

[4] M. H. Anderson, J. R. Ensher, M. R. Matthews, C. E. Wieman, and E. A. Cornell. Observation of Bose-Einstein condensation in a dilute atomic vapor. Science, 269(5221):198–201, 1995.

[5] M. R. Andrews, C. G. Townsend, H.-J. Miesner, D. S. Durfee, D. M. Kurn, and W. Ketterle. Observation of interference between two Bose condensates. Science, 275(5300):637–641, 1997.

[6] M. R. Matthews, B. P. Anderson, P. C. Haljan, D. S. Hall, C. E. Wieman, and E. A. Cornell. Vortices in a Bose-Einstein condensate. Phys. Rev. Lett., 83:2498–2501, Sep 1999.

[7] B. DeMarco and D. S. Jin. Onset of Fermi degeneracy in a trapped atomic gas. Science, 285(5434):1703–1706, 1999.

[8] D.O. Edwards and M.S. Pettersen. Lectures on the properties of liquid and solid 3He-4He mixtures at low temperatures. Journal of Low Temperature Physics, 87(3-4):473–523, 1992.

[9] Leon N. Cooper. Bound electron pairs in a degenerate Fermi gas. Phys. Rev., 104:1189–1190, Nov 1956.

[10] Elisa Fratini and Pierbiagio Pieri. Pairing and condensation in a resonant Bose–Fermi mixture. Phys. Rev. A, 81:051605, May 2010.

[11] RichardP. Feynman. Simulating physics with computers. International Journal of Theoretical Physics, 21(6-7):467–488, 1982.

[12] Immanuel Bloch, Jean Dalibard, and Wilhelm Zwerger. Many-body physics with ultracold gases. Rev. Mod. Phys., 80:885–964, Jul 2008.

[13] C. A. Regal and D. S. Jin. Experimental realization of the BCS-BEC crossover with a Fermi gas of atoms. Adv. Atom. Mol. Opt. Phys., 54:1–79, 2006.

[14] Markus Greiner, Olaf Mandel, Tilman Esslinger, Theodor W. Hansch, and Immanuel Bloch. Quantum phase transition from a superfluid to a Mott insulator in a gas of ultracold atoms. Nature, 415:39 – 44, Jan 2002.

[15] Waseem S. Bakr, Jonathon I. Gillen, Amy Peng, Simon Folling, and Markus Greiner. A quantum gas microscope for detecting single atoms in a Hubbard-regime optical lattice. Nature, 462, November 2009.

[16] Y.-J. Lin, K. Jiménez-Garcia, and I. Spielman. Spin-orbit-coupled Bose-Einstein condensates. Nature, 471, 2011.

[17] M. Georgescu, I. S. Ashhab, and Franco Nori. Quantum simulation. Rev. Mod. Phys., 86:153–185, Mar 2014.

[18] Cheng Chin, Paul Julienne, and Eite Tiesinga. Feshbach resonances in ultracold gases. Rev. Mod. Phys., 82(2):1225–1286, April 2010.

[19] T. Köhler, K. Góral, and P. S. Julienne. Production of cold molecules via magnetically tunable Feshbach resonances. Rev. Mod. Phys., 78:1311–1361, January 2006.

[20] K-K Ni, S. Ospelkaus, M. H. G. de Miranda, A. Pe'er, B. Neyenhuis, J. J. Zirbel, S. Kotochigova, P. S. Julienne, D. S. Jin, and J. Ye. A high phase-space-density gas of polar molecules. Science, 322:231, 2008.

[21] V. N. Efimov. Energy levels arising from resonant two-body forces in a three-body system. Phys. Lett. B, 33:563–564, Oct 1970.

[22] T. Kraemer, M. Mark, P. Waldburger, J. G. Danzl, C. Chin, B. Engeser, A. D. Lange, K. Pilch, A. Jaakkola, H.-C. Nägerl, and R. Grimm. Evidence for Efimov quantum states in an ultracold gas of caesium atoms. Nature, 440:315–318, Mar 2006.

[23] Eric Braaten and H.-W. Hammer. Universality in few-body systems with large scattering length. Phys. Rep., 428:259–390, Apr 2006.

[24] F. Ferlaino, A. Zenesini, M. Berninger, B. Huang, H. Nägerl, and R. Grimm. Efimov resonances in ultracold quantum gases. Few-Body Systems, 51:113–133, 2011. 10.1007/s00601-011-0260-7.

[25] Noam Gross, Zav Shotan, Servaas Kokkelmans, and Lev Khaykovich. Nuclear-spin-independent short-range three-body physics in ultracold atoms. Phys. Rev. Lett., 105:103203, Sep 2010.

[26] M. Berninger, A. Zenesini, B. Huang, W. Harm, H.-C. Nägerl, F. Ferlaino, R. Grimm, P. S. Julienne, and J. M. Hutson. Universality of the three-body parameter for Efimov states in ultracold Cesium. Phys. Rev. Lett., 107:120401, Sep 2011.

[27] Jia Wang, J. P. D'Incao, B. D. Esry, and Chris H. Greene. Origin of the three-body parameter universality in Efimov physics. Phys. Rev. Lett., 108:263001, Jun 2012.

[28] AJ Moerdijk, BJ Verhaar, and A. Axelsson. Resonances in ultracold collisions of 6Li, 7Li, and 23Na. Phys. Rev. A, 51(6):4852–4861, 1995.

[29] A. S. Jensen, K. Riisager, D. V. Fedorov, and E. Garrido. Structure and reactions of quantum halos. Rev. Mod. Phys., 76:215–261, Feb 2004.

[30] C. A. Regal, M. Greiner, S. Giorgini, M. Holland, and D. S. Jin. Momentum distribution of a Fermi gas of atoms in the BCS-BEC crossover. Phys. Rev. Lett., 95:250404, Dec 2005.

[31] Martin Berninger, Alessandro Zenesini, Bo Huang, Walter Harm, Hanns-Christoph Nägerl, Francesca Ferlaino, Rudolf Grimm, Paul S. Julienne, and Jeremy M. Hutson. Feshbach resonances, weakly bound molecular states, and coupled-channel potentials for Cesium at high magnetic fields. Phys. Rev. A, 87:032517, Mar 2013.

[32] C. Klempt, T. Henninger, O. Topic, M. Scherer, L. Kattner, E. Tiemann, W. Ertmer, and J. J. Arlt. Radio-frequency association of heteronuclear Feshbach molecules. Phys. Rev. A, 78:061602, Dec 2008.

[33] J. J. Zirbel, K.-K. Ni, S. Ospelkaus, T. L. Nicholson, M. L. Olsen, P. S. Julienne, C. E. Wieman, J. Ye, and D. S. Jin. Heteronuclear molecules in an optical dipole trap. Phys. Rev. A, 78(1):013416, July 2008.

[34] Paul S. Julienne. Ultracold molecules from ultracold atoms: a case study with the KRb molecule. Faraday Discuss., 142:361–388, 2009.

[35] J. P. D'Incao and B. D. Esry. Mass dependence of ultracold three-body collision rates. Phys. Rev. A, 73:030702, Mar 2006.

[36] Tyler Cumby. Exploring few-body scattering resonances in a Bose–Fermi mixture: from Feshbach dimers to Efimov trimers. PhD thesis, University of Colorado at Boulder, 2012.

[37] David E. Pritchard. Cooling neutral atoms in a magnetic trap for precision spectroscopy. Phys. Rev. Lett., 51:1336–1339, Oct 1983.

[38] Jon Goldwin. Quantum Degeneracy and Interactions in the 87Rb–40K Bose–Fermi Mixture. PhD thesis, University of Colorado, Boulder, CO, 2005.

[39] C. Monroe, W. Swann, H. Robinson, and C. Wieman. Very cold trapped atoms in a vapor cell. Phys. Rev. Lett., 65:1571–1574, Sep 1990.

[40] J. Goldwin, S. B. Papp, B. DeMarco, and D. S. Jin. Two-species magneto-optical trap with 40k and 87rb. Phys. Rev. A, 65:021402, Jan 2002.

[41] C. J. Myatt, E. A. Burt, R. W. Ghrist, E. A. Cornell, and C. E. Wieman. Production of two overlapping bose-einstein condensates by sympathetic cooling. Phys. Rev. Lett., 78:586–589, Jan 1997.

[42] Andrew G. Truscott, Kevin E. Strecker, William I. McAlexander, Guthrie B. Partridge, and Randall G. Hulet. Observation of Fermi pressure in a gas of trapped atoms. Science, 291(5513):2570–2572, 2001.

[43] Rudolf Grimm, Matthias Weidemüller, and Yurii Ovchinnikov. Optical dipole traps for neutral atoms. Advances in Atomic, Molecular and Optical Physics, 42:95–170, 2000.

[44] Michele Olsen. Experiments with Feshbach molecules in a Bose–Fermi mixture. PhD thesis, University of Colorado, Boulder, CO, December 2008.

[45] S. Ospelkaus, C. Ospelkaus, L. Humbert, K. Sengstock, and K. Bongs. Tuning of heteronuclear interactions in a quantum-degenerate Fermi–Bose mixture. Phys. Rev. Lett., 97:120403, July 2006.

[46] M. Zaccanti, C. D'Errico, F. Ferlaino, G. Roati, M. Inguscio, and G. Modugno. Control of the interaction in a Fermi–Bose mixture. Phys. Rev. A, 74:041605, Oct 2006.

[47] Th. Best, S. Will, U. Schneider, L. Hackermüller, D. van Oosten, I. Bloch, and D.-S. Lühmann. Role of interactions in ^{87}Rb-^{40}K Bose–Fermi mixtures in a 3d optical lattice. Phys. Rev. Lett., 102:030408, Jan 2009.

[48] C. Ospelkaus, S. Ospelkaus, L. Humbert, P. Ernst, K. Sengstock, and K. Bongs. Ultracold Heteronuclear Molecules in a 3D Optical Lattice. Phys. Rev. Lett., 97(12):120402, September 2006.

[49] Daniel Steck. Rubidium 87 D line data. http://steck.us/alkalidata, Dec 2010.

[50] Tobias Tiecke. Properties of potassium. http://steck.us/alkalidata, Feb 2010.

[51] B. DeMarco, H. Rohner, and D. S. Jin. An enriched 40K source for Fermionic atom studies. Rev. Sci. Instrum, 70, 1999.

[52] Claude Cohen-Tannoudji. Atom-Photon Interactions: Basic Processes and Applications. Wiley, 1992.

[53] W. Ketterle, D. S. Durfee, and D. M. Stamper-Kurn. Making, probing, and understanding Bose-Einstein condensates. In M. Inguscio, S. Stringari, and C. Wieman, editors, Proceedings of the International School of Physics 'E. Fermi': Cource CXL - Bose-Einstein Condensation in atomic gases. 1998.

[54] Henry Lao. Quantum Behavior of an Atomic Fermi Gas. PhD thesis, University of Colorado at Boulder, 2001.

[55] Tyler D. Cumby, Ruth A. Shewmon, Ming-Guang Hu, John D. Perreault, and Deborah S. Jin. Feshbach-molecule formation in a Bose–Fermi mixture. Phys. Rev. A, 87:012703, Jan 2013.

[56] Jan Chwedeńczuk, Krzysztof Góral, Thorsten Köhler, and Paul S. Julienne. Molecular Production in Two Component Atomic Fermi Gases. Phys. Rev. Lett., 93(26):260403, December 2004.

[57] C. Zener. Non-adiabatic Crossing of Energy Levels. Proc. R. Soc. A, 137(833):696–702, 1932.

[58] E. Hodby, S. T. Thompson, C. A. Regal, M. Greiner, A. C. Wilson, D. S. Jin, E. A. Cornell, and C. E. Wieman. Production efficiency of ultracold Feshbach molecules in bosonic and fermionic systems. Phys. Rev. Lett., 94(12):120402, 2005.

[59] S. B. Papp and C. E. Wieman. Observation of heteronuclear Feshbach molecules from a 85Rb87Rb gas. Phys. Rev. Lett., 97(18):180404, Oct 2006.

[60] F. M. Spiegelhalder, A. Trenkwalder, D. Naik, G. Kerner, E. Wille, G. Hendl, F. Schreck, and R. Grimm. All-optical production of a degenerate mixture of 6Li and 40K and creation of heteronuclear molecules. Phys. Rev. A, 81(4):043637, April 2010.

[61] Zeng-Qiang Yu, Shizhong Zhang, and Hui Zhai. Stability condition of a strongly interacting boson-fermion mixture across an interspecies Feshbach resonance. Phys. Rev. A, 83:041603, Apr 2011.

[62] T. Sogo, P. Schuck, and M. Urban. Bose-Fermi pairs in a mixture and the Luttinger theorem within a Nozières-Schmitt-Rink-like approach. Phys. Rev. A, 88:023613, Aug 2013.

[63] Andrea Guidini, Gianluca Bertaina, Elisa Fratini, and Pierbiagio Pieri. Bose-Fermi mixtures in the molecular limit. Phys. Rev. A, 89:023634, Feb 2014.

[64] Cheng-Hsun Wu, Jee Woo Park, Peyman Ahmadi, Sebastian Will, and Martin W. Zwierlein. Ultracold Fermionic Feshbach molecules of 23Na40K. Phys. Rev. Lett., 109:085301, 2012.

[65] Myoung-Sun Heo, Tout T. Wang, Caleb A. Christensen, Timur M. Rvachov, Dylan A. Cotta, Jae-Hoon Choi, Ye-Ryoung Lee, and Wolfgang Ketterle. Formation of ultracold fermionic NaLi Feshbach molecules. Phys. Rev. A, 86:021602, Aug 2012.

[66] J. E. Williams, N. Nygaard, and C. W. Clark. Theory of Feshbach molecule formation in a dilute gas during a magnetic field ramp. New J. Phys., 8:150, 2006.

[67] Shohei Watabe and Tetsuro Nikuni. Conversion efficiencies of heteronuclear Feshbach molecules. Phys. Rev. A, 77(1):1–20, January 2008.

[68] Tomotake Yamakoshi, Shinichi Watanabe, Chen Zhang, and Chris H. Greene. Stochastic and equilibrium pictures of the ultracold fano-feshbach-resonance molecular conversion rate. Phys. Rev. A, 87:053604, May 2013.

[69] Jesper Bertelsen and Klaus Mø lmer. Association of heteronuclear molecules in a harmonic oscillator well. Phys. Rev. A, 76(4):1–9, October 2007.

[70] Chen Zhang, Javier von Stecher, and Chris H. Greene. Few-body ultracold reactions in a Bose–Fermi mixture. Phys. Rev. A, 85:043615, Apr 2012.

[71] J. J. Zirbel, K.-K. Ni, S. Ospelkaus, J. P. D'Incao, C. E. Wieman, J. Ye, and D. S. Jin. Collisional stability of fermionic Feshbach molecules. Phys. Rev. Lett., 100(14):143201, April 2008.

[72] H. Bruns. Über die integrale des vielkörper-problems. Acta Mathematica, 11(1-4):25–96, 1887.

[73] Milovan Šuvakov and V. Dmitrašinović. Three classes of Newtonian three-body planar periodic orbits. Phys. Rev. Lett., 110:114301, Mar 2013.

[74] V. N. Efimov. Weakly bound states of three resonantly interacting particles. Yad. Fiz., 12:1080–1091, 1970.

[75] Lucas Platter. Low-energy universality in atomic and nuclear physics. Few-Body Systems, 46(3):139–171, 2009.

[76] N T Zinner and A S Jensen. Comparing and contrasting nuclei and cold atomic gases. Journal of Physics G: Nuclear and Particle Physics, 40(5):053101, 2013.

[77] P. Makotyn, C. E. Klauss, D. L. Goldberger, E. A. Cornell, and D. S. Jin. Universal dynamics of a degenerate unitary Bose gas. Nat Phys, pages 116 – 119, 2014.

[78] D. Hudson Smith, Eric Braaten, Daekyoung Kang, and Lucas Platter. Two-body and three-body contacts for identical Bosons near unitarity. arXiv:1309.6922 [cond-mat.quant-gas], 2014.

[79] Bo Huang, Leonid A. Sidorenkov, Rudolf Grimm, and Jeremy M. Hutson. Observation of the second triatomic resonance in Efimov's scenario. Phys. Rev. Lett., 112:190401, May 2014.

[80] A. S. Jensen and D. V. Fedorov. Efimov states in asymmetric systems. Europhys. Lett., 62(3):336–342, 2003.

[81] K. Helfrich, H.-W. Hammer, and D. S. Petrov. Three-body problem in heteronuclear mixtures with resonant interspecies interaction. Phys. Rev. A, 81:042715, Apr 2010.

[82] Shih-Kuang Tung, Karina Jimenez-Garcia, Jacob Johansen, Colin V. Parker, and Cheng Chin. Observation of geometric scaling of Efimov states in a Fermi-Bose Li-Cs mixture. arXiv:1402.5943v1 [cond-mat.quant-gas], February 2014.

[83] R. Pires, J. Ulmanis, S. Häfner, M. Repp, A. Arias, E. D. Kuhnle, and M. Weidemüller. Observation of Efimov resonances in a mixture with extreme mass imbalance. arXiv:1403.7246 [cond-mat.quant-gas], March 2014.

[84] D. V. Fedorov, A. S. Jensen, and K. Riisager. Efimov states in halo nuclei. Phys. Rev. Lett., 73:2817–2820, Nov 1994.

[85] B. Acharya, C. Ji, and D.R. Phillips. Implications of a matter-radius measurement for the structure of Carbon-22. Physics Letters B, 723(1 - 3):196 – 200, 2013.

[86] G. Hagen, P. Hagen, H.-W. Hammer, and L. Platter. Efimov physics around the neutron-rich Ca60 isotope. Phys. Rev. Lett., 111:132501, Sep 2013.

[87] J. P. D'Incao, H. Suno, and B. D. Esry. Limits on universality in ultracold three-Boson recombination. Phys. Rev. Lett., 93:123201, Sep 2004.

[88] Olga Machtey, Zav Shotan, Noam Gross, and Lev Khaykovich. Association of Efimov trimers from a three-atom continuum. Phys. Rev. Lett., 108:210406, May 2012.

[89] Thomas Lompe, Timo B. Ottenstein, Friedhelm Serwane, Andre N. Wenz, Gerhard Zürn, and Selim Jochim. Radio-frequency association of Efimov trimers. Science, 330(6006):940–944, 2010.

[90] Shuta Nakajima, Munekazu Horikoshi, Takashi Mukaiyama, Pascal Naidon, and Masahito Ueda. Measurement of an Efimov trimer binding energy in a three-component mixture of 6Li. Phys. Rev. Lett., 106:143201, Apr 2011.

[91] J. P. D'Incao and B. D. Esry. Scattering length scaling laws for ultracold three-body collisions. Phys. Rev. Lett., 94:213201, Jun 2005.

[92] G. Barontini, C. Weber, F. Rabatti, J. Catani, G. Thalhammer, M. Inguscio, and F. Minardi. Observation of heteronuclear atomic Efimov resonances. Phys. Rev. Lett., 103:043201, Jul 2009.

[93] E. Nielsen, H. Suno, and B. D. Esry. Efimov resonances in atom-diatom scattering. Phys. Rev. A, 66:012705, Jul 2002.

[94] J. P. D'Incao, B. D. Esry, and Chris H. Greene. Ultracold atom-molecule collisions with fermionic atoms. Phys. Rev. A, 77:052709, May 2008.

[95] T. B. Ottenstein, T. Lompe, M. Kohnen, A. N. Wenz, and S. Jochim. Collisional stability of a three-component degenerate Fermi gas. Phys. Rev. Lett., 101:203202, Nov 2008.

[96] J. H. Huckans, J. R. Williams, E. L. Hazlett, R. W. Stites, and K. M. O'Hara. Three-body recombination in a three-state Fermi gas with widely tunable interactions. Phys. Rev. Lett., 102:165302, Apr 2009.

[97] M. Zaccanti, B. Deissler, C. D'Errico, M. Fattori, M. Jona-Lasinio, S. Müller, G. Roati, M. Inguscio, and G. Modugno. Observation of an Efimov spectrum in an atomic system. Nature Physics, 5:586–591, Jul 2009.

[98] Scott E. Pollack, Daniel Dries, and Randal G. Hulet. Universality in three- and four-body bound states of ultracold atoms. Science, 326:1683–1685, Dec 2009.

[99] R. J. Wild, P. Makotyn, J. M. Pino, E. A. Cornell, and D. S. Jin. Measurements of Tan's contact in an atomic Bose-Einstein condensate. Phys. Rev. Lett., 108:145305, Apr 2012.

[100] Pascal Naidon, Shimpei Endo, and Masahito Ueda. Physical origin of the universal three-body parameter in atomic Efimov physics. arXiv:1208.3912v1, [cond-mat.quant-gas], 2012.

[101] Richard Schmidt, Steffen Patrick Rath, and Wilhelm Zwerger. Efimov physics beyond universality. Eur. Phys. B, 85, 2012.

[102] P. K. Sørensen, D. V. Fedorov, A. S. Jensen, and N. T. Zinner. Efimov physics and the three-body parameter within a two-channel framework. Phys. Rev. A, 86:052516, Nov 2012.

[103] Y. Wang and P. Julienne. Universal van der Waals physics for three ultracold atoms. arXiv:1404.0483 [physics.atom-ph], April 2014.

[104] Noam Gross, Zav Shotan, Servaas Kokkelmans, and Lev Khaykovich. Observation of universality in ultracold 7Li three-body recombination. Phys. Rev. Lett., 103:163202, Oct 2009.

[105] S. Knoop, F. Ferlaino, M. Mark, M. Berninger, H. Schöbel, H.-C. Nägerl, and R. Grimm. Observation of an Efimov-like trimer resonance in ultracold atom-dimer scattering. Nat. Phys., 5:227, February 2009.

[106] T. Lompe, T. B. Ottenstein, F. Serwane, K. Viering, A. N. Wenz, G. Zürn, and S. Jochim. Atom-dimer scattering in a three-component Fermi gas. Phys. Rev. Lett., 105:103201, Sep 2010.

[107] Shuta Nakajima, Munekazu Horikoshi, Takashi Mukaiyama, Pascal Naidon, and Masahito Ueda. Nonuniversal Efimov atom-dimer resonances in a three-component mixture of 6Li. Phys. Rev. Lett., 105:023201, Jul 2010.

[108] V. Efimov. Energy levels of three resonantly interacting particles. Nuclear Physics A, 210(1):157 – 188, 1973.

[109] J. P. D'Incao and B. D. Esry. Ultracold three-body collisions near overlapping feshbach resonances. Phys. Rev. Lett., 103:083202, Aug 2009.

[110] Sanjukta Roy, Manuele Landini, Andreas Trenkwalder, Giulia Semeghini, Giacomo Spagnolli, Andrea Simoni, Marco Fattori, Massimo Inguscio, and Giovanni Modugno. Test of the universality of the three-body Efimov parameter at narrow Feshbach resonances. Phys. Rev. Lett., 111:053202, Aug 2013.

[111] A. N. Wenz, T. Lompe, T. B. Ottenstein, F. Serwane, G. Zürn, and S. Jochim. Universal trimer in a three-component Fermi gas. Phys. Rev. A, 80:040702, Oct 2009.

[112] Olga Machtey, David A. Kessler, and Lev Khaykovich. Universal dimer in a collisionally opaque medium: Experimental observables and Efimov resonances. Phys. Rev. Lett., 108:130403, Mar 2012.

[113] Christian Langmack, D. Hudson Smith, and Eric Braaten. Avalanche mechanism for atom loss near an atom-dimer Efimov resonance. Phys. Rev. A, 86:022718, Aug 2012.

[114] Cheng Chin. Universal scaling of Efimov resonance positions in cold atom systems. arXiv:1111.1484v2, [cond-mat.quant-gas], 2011.

[115] S. Knoop, J. S. Borbely, W. Vassen, and S. J. J. M. F. Kokkelmans. Universal three-body parameter in ultracold 4He*. Phys. Rev. A, 86:062705, Dec 2012.

[116] Yujun Wang, Jia Wang, J. P. D'Incao, and Chris H. Greene. Universal three-body parameter in heteronuclear atomic systems. Phys. Rev. Lett., 109:243201, Dec 2012.

[117] Ruth S. Bloom, Ming-Guang Hu, Tyler D. Cumby, and Deborah S. Jin. Tests of universal three-body physics in an ultracold Bose–Fermi mixture. Phys. Rev. Lett., 111:1, Sep 2013.

[118] Alessandro Zenesini, Bo Huang, Martin Berninger, Hanns-Christoph Nägerl, Francesca Ferlaino, and Rudolf Grimm. Resonant atom-dimer collisions in cesium: Testing universality at positive scattering lengths. arXiv:1406.3443v1, [cond-mat.quant-gas], 2014.

[119] B. D. Esry, Chris H. Greene, and James P. Burke. Recombination of three atoms in the ultracold limit. Phys. Rev. Lett., 83:1751–1754, Aug 1999.

[120] C. Ospelkaus, S. Ospelkaus, K. Sengstock, and K. Bongs. Interaction-driven dynamics of 40K-87Rb Fermion-Boson gas mixtures in the large-particle-number limit. Phys. Rev. Lett., 96:020401, Jan 2006.

[121] Brandon P. Ruzic, Chris H. Greene, and John L. Bohn. Quantum defect theory for high-partial-wave cold collisions. Phys. Rev. A, 87:032706, Mar 2013.

[122] C. Klempt, T. Henninger, O. Topic, J. Will, W. Ertmer, E. Tiemann, and J. Arlt. 40K-87Rb Feshbach resonances: Modeling the interatomic potential. Phys. Rev. A, 76(2):020701(R), August 2007.

[123] Ming-Guang Hu, Ruth Bloom, Jon Goldwin, and Deborah Jin. Search for avalanche mechanism loss at an atom-molecule efimov resonance. arXiv:1405.4915v2 [cond-mat.quant-gas], 2014.

[124] Andrea Simoni, Matteo Zaccanti, Chiara D'Errico, Marco Fattori, Giacomo Roati, Massimo Inguscio, and Giovanni Modugno. Near-threshold model for ultracold KRb dimers from interisotope Feshbach spectroscopy. Phys. Rev. A, 77:052705, May 2008.

[125] Vitaly Efimov. Force-range correction in the three-body problem: Application to three-nucleon systems. Phys. Rev. C, 44:2303–2310, Dec 1991.

[126] M. Thøgersen, D. V. Fedorov, and A. S. Jensen. Universal properties of Efimov physics beyond the scattering length approximation. Phys. Rev. A, 78:020501, Aug 2008.

[127] L. Platter, C. Ji, and D. R. Phillips. Range corrections to three-body observables near a Feshbach resonance. Phys. Rev. A, 79:022702, Feb 2009.